2014

Analysis of Microstructural Evolution and Fracture Mechanisms in Ti-5Al-5V-5Mo-3Cr-0.4Fe in Response to Electron Beam Welding and Post Weld Heat Treatments

Joseph Colter Sabol
Lehigh University

Analysis of Microstructural Evolution and Fracture Mechanisms in Ti-5Al-5V-5Mo-3Cr-0.4Fe in Response to Electron Beam Welding and Post Weld Heat Treatments

By

Joseph C. Sabol

Presented to the Graduate and Research Committee
of Lehigh University
in Candidacy for the Degree of
Doctor of Philosophy

in

Materials Science and Engineering

Lehigh University

May 2014

Approved and recommended for acceptance as a dissertation in partial fulfilment of the requirements for the degree of Doctor of Philosophy.

Date

Dissertation Director

Accepted Date

Committee Members:

Dr. Wojciech Z. Misiolek

Dr. John N. DuPont

Dr. Natasha Vermaak

Dr. Masashi Watanabe

Acknowledgements

First, I would like to thank Dr. Wojciech Misiolek for inviting me to join his graduate research group and serving as a competent advisor and fellow skier. Your trust in your graduate students has made my graduate studies my own. It's what you make of what is given to you, not what others make of it for you. I am glad that I had the opportunity to work with you.

I would also like to thank Timotius Pasang of Auckland University of Technology, Auckland, NZ. Without him, the current work would not have been possible and my trip to Auckland to work at AUT would have never occurred.

Many thanks are due to my fellow graduate students in the department and IMF group members who were always there to provide insight to problems. Thanks are deserved by Lauren Bacigalupo, Dan Bechetti, Brett Leister, Chris Marvel, Mark McLean, Andrew Stockdale, Anthony Ventura, and Austin Wade. Without them, I would not have gotten as far as I did. They are great co-workers and even better friends.

I would especially like to thank Arlan Benscoter and Sam Lawrence for their guidance in lab. Both have pushed me to strive for excellence in my work as well as have provided motivation to challenge myself. Their expertise in metallography is second to none and I am grateful for being able to learn from them the skills that I will use for my entire career. Their guidance and friendship are invaluable.

To all of the Materials Science & Engineering staff – Janie Carlin, John Gregoris Katrina Kraft, Brie Lisk, Anne Marie Lobley, Mike Rex– thank you for your patience with me and for seeing potential in me, of which I was not aware.

Special thanks are due to the Loewy Foundation. Through the generosity of the Loewy family, my project and I were supported, for which I am extremely thankful.

Most of all, I would like to thank my family. Their love and encouragement has made me who I am today and has enabled me to stick it out through tough times. To my mom and dad and two sisters, I love you.

List of Tables ..... **ix**

List of Figures ..... **x**

Abstract **1**

1. Introduction *3*

1.1. Titanium and its Alloys *3*

1.1.1. Titanium Alloy Classification *4*

1.1.1.1. α Alloys *6*

1.1.1.2. α+β Alloys *7*

1.1.1.3. β Alloys *9*

1.2. Phases in Titanium *11*

1.2.1. Equilibrium Phases *12*

1.2.1.1. α *12*

1.2.1.2. β *14*

1.2.1.3. B2 ..... *16*

1.2.1.4. α_2 ..... *16*

1.2.1.5. γ *16*

1.2.1.6. O *17*

1.2.1.7. $B8_2$ *17*

1.2.2. Non-Equilibrium Phases *17*

1.2.2.1. α' *18*

1.2.2.2. α'' *18*

1.2.2.3. ω *19*

1.2.2.4. β' *20*

1.3. Phase Transformations in Titanium *21*

1.3.1. β to α *21*

1.3.2. β to ω *23*

1.3.3. ω to α *28*

1.4. Welding Titanium and Titanium Alloys *29*

1.4.1. Problems Associated with Welding Titanium Alloys *30*

1.4.2. Electron Beam Welding *31*

1.5. Ti-5Al-5V-5Mo-3Cr-0.4Fe (Ti-5553) Alloy *32*

1.5.1. History and Applications of Ti-5553 ..... *32*

1.5.2. Microstructures and Mechanical Properties *33*

1.5.3. Welding of Ti-5553 ..... *34*

1.6. Motivation *35*

2. Experimental Procedure 37
2.1. Material 37
2.2. Electron Beam Welding 37
2.3. Post Weld Heat Treatments 37
2.4. Metallographic Specimen Preparation 38
2.5. Electron Probe Microanalysis 39
2.6. Mechanical Properties Testing 39
2.6.1. Microhardness Profiles 39
2.6.2. Uniaxial Tensile Testing 40
2.6.3. Localized Strain Measurement 40
2.6.3.1. ARAMIS and Digital Image Correlation 40
2.6.3.2. ARAMIS – Setup and Testing 42
2.7. Fracture Analysis 45
2.7.1. Scanning Electron Microscopy 45
2.7.2. Metallographic Analysis 46
2.8. Transmission Electron Microscopy 46
2.8.1. Specimen Preparation 46
2.8.2. Transmission Electron Microscopy 47
2.8.3. Atomic Resolution Microscopy 49
3. Results and Discussion 49
3.1. Mechanical Testing 49
3.1.1. Section 3.1 Summary 54
3.2. Microstructure 55
3.2.1. As-Welded Condition 55
3.2.2. Post Weld Heat Treatment Conditions 58
3.2.3. Section 3.2 Summary 75
3.3. Solidification 76
3.3.1. Scheil Analysis 76
3.3.2. Effects of PWHTs on Homogenization 84
3.3.3. Section 3.3 Summary 92
3.4. Identification of Precipitates within the Fusion Zone 92
3.4.1. α 94
3.4.2. ω 99
3.4.3. Section 3.4 Summary 104
3.5. HAADF-STEM Investigation of ω in the FZ of As-Welded Ti-5553 105
3.5.1. Section 3.5 Summary 114

3.6. Fracture of EBW Ti-5553 ..... *114*
3.6.1. Influence of ω on Fracture *123*
3.6.2. Section 3.6 Summary *125*
4. Conclusions *125*
5. Future Work *127*
6. References *129*
7. Vita *137*

List of Tables

Table 1.1. Common β-stabilizing elements and their critical minimum contents required to retain fully β structures upon quenching as well as their effects per wt.% of addtion on suppressing the β-transus temperature in binary Ti systems (recreated from Bania, 1994). 10

Table 1.2. Common solute lean and solute rich β alloys and their corresponding nominal compositions. 11

Table 2.1. Nominal composition of Ti-5553 (values are in wt.%). 37

Table 2.2. Post weld heat treatment temperatures and times used for subsequent precipitation strengthening after electron beam welding. 38

Table 2.3. Setup geometry distances and angles for use with the ARAMIS HS system equipped with a 50mm lens and using the smallest calibration panel (15mmx12mm). Refer to Figure 2.3. 44

Table 3.1. Average yield and ultimate tensile strengths along with the localized tensile strain in the vicinity of the WZ from ARAMIS for EBW Ti-5553. 52

Table 3.2. Average hardness of the BM, HAZ, and FZ in EBW Ti-5553 (all values are Vickers hardness – HV). 53

List of Figures

Figure 1.1. Schematic pseudo-binary phase diagram of the Ti-rich sections showing the effects of (left to right) α stabilizing elements, β stabilizing elements (isomorphous and eutectoid), and neutral elements on the β-transus temperature and phase regimes [Lütjering and Williams, 2007]. 5

Figure 1.2. Schematic representation of a pseudo-binary section through a β-isomorphous phase diagram indicating regions pertaining to α alloys, α+β alloys, and β alloys (metastable and stable β alloys) [Luutjering and Williams]. 5

Figure 1.3. Schematic of the α unit cell in pure Ti with one of each of the corresponding closed packed planes 0002, prismatic planes $10\bar{1}0$, and pyramidal planes $10\bar{1}1$ [Lütjering and Williams, 2007]. 14

Figure 1.4. Schematic of the β unit cell in pure Ti with one of the corresponding close packed planes 110 [Lütjering and Williams, 2007]. 15

Figure 1.5. Selected area diffraction pattern of the 131β zone normal (Z.N.) (left) in Ti-15 wt.% Mo and accompanying schematic of the 131β zone normal with indexed reflections [De Fontaine et al., 1971]. 23

Figure 1.6. Schematic of the atoms which move during the collapse of the 111β planes in forming the ω-phase [Bagariatskii et al., 1959]. 24

Figure 1.7. A longitudinal sinusoidal displacement wave showing its effect on the 111β planes during the propagation of the wave to transform β to ω [De Fontaine, 1973]. 25

Figure 1.8. Representation of the 111β planes in a BCC crystal at different stages of transformation to ω [Lütjering and Williams, 2007]. 26

Figure 1.9. HRTEM image of Ti-20mass%Mo aged at 623K for 8 hours showing two ω variants [Sukedai et al., 1991]. 27

Figure 1.10. (a) HRTEM image of ω in Ti-9at.%Mo and (b) HAADF-STEM image of ω in the same sample [Devaraj et al. 2012]. 27

Figure 1.11. (left) A 110β zone axis pattern with ω superlattice reflections at 1/2 and 1/3 the 211β reflections [Harper, 2004] and (right) a 113β zone axis pattern with an accompanying dark field image showing α which has nucleated on a ω particle [Nag et al., Acta Mater., 2009]. 34

Figure 2.1. An example of a high contrast stochrastic pattern that can easily be recognized by ARAMIS [GOM mbH, Software]. 42

Figure 2.2, An example of a sub-size tensile specimen with high contrast speckle pattern applied by spray painting. 43

Figure 2.3. A representative diagram of the geometry between the measuring volume and cameras for typical testing using an ARAMIS system [GOM mbH, Hardware, 2007]. 44

Figure 2.4. Example panels for calibrating ARAMIS and determining a measuring volume [GOM mbH, Software, 2007]. 44

Figure 2.5. Set up of the tensile frame with ARAMIS after testing a specimen. 45

Figure 3.1. (left) Representative tensile results of true stress versus time and true strain for a EBW Ti-5553 tensile specimen in the AW condition and (right) corresponding localized strain distributions from ARAMIS for the same tensile specimen at times of 0 seconds (A), 10 seconds (B), 20 seconds (C), 30 seconds (D), 40 seconds (E), and immediately prior to failure (F) – approximately 53 seconds (the tensile direction is oriented horizontally). 50

Figure 3.2. (left) Representative tensile results of true stress versus time and true strain for a EBW Ti-5553 tensile specimen heat treated at 700°C/4 hours and (right) corresponding localized strain distributions from ARAMIS for the same tensile specimen at times of 0 seconds, 30 seconds, and immediately prior to failure – approximately 67 seconds (the tensile direction is oriented horizontally). 50

Figure 3.3. (left) Representative tensile results of true stress versus time and true strain for a EBW Ti-5553 tensile specimen heat treated at 804°C/1 hour and (right) corresponding localized strain distributions from ARAMIS for the same tensile specimen at times of 0 seconds, 15 seconds, and immediately prior to failure – approximately 24 seconds (the tensile direction is oriented horizontally). 51

Figure 3.4. (left) Representative tensile results of true stress versus time and true strain for a EBW Ti-5553 tensile specimen heat treated at 804°C/1 hour then aged at 600°C/4 hours and (right) corresponding localized strain distributions from ARAMIS for the same tensile specimen at times of 0 seconds, 15 seconds, and immediately prior to failure – approximately 26 seconds (the tensile direction is oriented horizontally). 51

Figure 3.5. Hardness profile across the weld from BM to BM in EBW Ti-5553 in the AW condition. 54

Figure 3.6. Hardness profiles across the welds from BM to BM in EBW Ti-5553 subjected to PWHTs (left) at 700°C/4 hours, (center) at 804°C/1 hour, and (right) at 804°C/1 hour followed by aging at 600°C/4 hours. 54

Figure 3.7. Representative image of the weld cross-section from an EBW Ti-5553 specimen in the as-welded condition (etched in Kroll's using an etch-polish-etch technique). The two black spots at the FZ/HAZ boundary are pores, which developed during solidification [Sabol et al., 2012]. 55

Figure 3.8. Representative images from and EBW Ti-5553 specimen in the as-welded condition of (a) the weld centerline in the fusion zone detailing the cellular dendritic structure and (b) the boundary between the heat affected zone (left side in b) and the fusion zone (right side in b) [Sabol et al., 2012]. 56

Figure 3.9. Representative images from an EBW Ti-5553 specimen in the as-welded condition of (a) the equiaxed grains within the HAZ and (b) the transition from the HAZ to the BM [Sabol et al., 2012]. 57

Figure 3.10. Representative images of weld cross-sections from EBW Ti-5553 after PWHTs at (a) 700°C/4 hours, (b) 804°C/1 hour, and (c) 804°C/1 hour followed by aging at 600°C/4 hours (etched in Kroll's using an etch-polish-etch technique). 59

Figure 3.11. Representative images of the BM, SCHAZ, CHAZ, and FZ from each of the PWHTs at (a-d) 700°C/4 hours, (e-f) 804°C/1 hour, and (i-l) 804°C/1 hour followed by aging at 600°C/4 hours. 61

Figure 3.12. Backscatter secondary electron images of the BM in each of the PWHT conditions at lower magnification (left) and higher magnification (right). 63

Figure 3.13. Backscatter secondary electron image of the BM in the AW condition at lower magnification (left) and higher magnification (right). 64

Figure3.14. Backscatter secondary electron images of the SCHAZ in each of the PWHT conditions at lower magnification (left) and higher magnification (right)..... 65

Figure3.15. Backscatter secondary electron images of the CHAZ in each of the PWHT conditions at lower magnification (left) and higher magnification (right)..... 66

Figure3.16. Backscatter secondary electron images of the FZ in each of the PWHT conditions at lower magnification (left) and higher magnification (right). 67

Figure 3.17. Schematic of the equilibrium pseudo binary phase diagram showing the compositions associated with the α- and β-phases at the heat treatment temperatures (700°C, 804°C, 600°C) as well as the nominal [Mo]eq composition of Ti-5553 69

Figure 3.18. Representative composition profile acquired across a grain boundary for a specimen post weld heat treated at 700°C/4h. 72

Figure 3.19. Representative composition profile acquired across a grain boundary for a specimen post weld heat treated at 804°C/1 hours. 72

Figure 3.20. Representative composition profile acquired across a grain boundary for a specimen post weld heat treated at 804°C/1 hours followed by aging at 600°C/4 hours. 73

Figure 3.21. Schematics of Gibbs free energy versus temperature for the three PWHT temperatures, 804°C, 700°C, and 600°C (left, center, right). 75

Figure 3.22. Backscatter secondary electron image of cellular dendrites in the FZ of an EBW Ti-5553 specimen in the AW condition (top) and the corresponding concentration profiles of alloying elements across the cellular dendrites generated by EPMA (bottom). The white line in the backscatter image designates the location from which the concentration profiles were acquired..... 77

Figure 3.23. EPMA concentration profiles across the FZ from one HAZ to the other showing the depletion of Al in the FZ after EBW of Ti-5553. The FZ composition of Al is approximately 4.66 wt.%Al compared to the nominal composition of 5.03 wt.%Al before EBW. 78

Figure 3.24. Dimensionless α parameter as a function of cooling rate for the main alloying elements in Ti-5553. 80

Figure 3.25. A comparison of specific heat as a function of temperature for VT22, Beta 21, and Ti-6Al-4V. 82

Figure 3.26. A plot of composition versus fraction solid based on the Scheil calculations for solute partitioning during solidification in the FZ of EBW Ti-5553. 84

Figure 3.27. Backscatter secondary electron image of cellular dendrites in the FZ of an EBW Ti-5553 specimen heat treated at 700°C/4h (top) and the corresponding concentration profiles of alloying elements across the cellular dendrites generated by EPMA (bottom). The white line in the backscatter image designates the location from which the concentration profiles were acquired. 85

Figure 3.28. Backscatter secondary electron image of cellular dendrites in the FZ of an EBW Ti-5553 specimen heat treated at 804°C/1h (top) and the corresponding concentration profiles of alloying elements across the cellular dendrites generated by EPMA (bottom). The white line in the backscatter image designates the location from which the concentration profiles were acquired. 86

Figure 3.29. Backscatter secondary electron image of cellular dendrites in the FZ of an EBW Ti-5553 specimen heat treated at 804°C/1h followed by aging at 600°C/4h (top) and the corresponding concentration profiles of alloying elements across the cellular dendrites generated by EPMA (bottom). The white line in the backscatter image designates the location from which the concentration profiles were acquired. 87

Figure 3.30. Arrhenius diagram of Ti self-diffusion and diffusion of selected alloying elements in the β and α phases. The dashed line represents the β-transus of pure Ti (882°C) [Lütjering and Williams, 2007]. 89

Figure 3.31. A plot of the index of residual segregation, δ, versus time for PWHT temperatures and times of 700°C for 4 hours and 804°C for 1 hour. Data for 600°C for 4 hours is not shown because δ was approximately 1, meaning no homogenization occurred. 89

Figure 3.32. Extrapolated plot of δ for Mo out to 3 hours for a PWHT temperature of 804°C. An acceptable degree of homogenization ($\delta<0.1$) is achieved in approximately 2.9 hours. 90

Figure 3.33. Theoretical homogenization temperatures versus homogenization times for PHWTs performed above the β-transus (856°C) for EBW Ti-5553. 91

Figure 3.34. (a) SAD pattern of the 100_β zone axis, (b) indexed schematic of (a), and (c) the accompanying 0001_α DF image from the FZ of a specimen heat treated at 700°C/4 hours. The indices in red boxes correspond to the α-phase. 96

Figure 3.35. (a) SAD pattern of the 100_β zone axis, (b) an enlarged schematic of (a), and (c) the accompanying 0001_α DF image from the FZ of a specimen heat treated at 804°C/1 hour. The indices in red boxes correspond to the α-phase. 97

Figure 3.36. (a) SAD pattern of the 100β zone axis and (b) an enlarged schematic of (a) from the FZ of a specimen heat treated at 804°C/1h followed by aging at 600°C/4h. The indices in red boxes and circles correspond to the $\alpha 1$ and $\alpha 2$ variants, respectively. 98

Figure 3.37. DF images from the FZ of specimens heat treated at 804°C/1h followed by aging at 600°C/4h acquired using the (a) $10\bar{1}1\alpha 2$ reflection, (b) $1011\alpha 2$ reflection, (c) $10\bar{1}1\alpha 2$ reflection, and (d) $1011\alpha 2$ reflection. 98

Figure 3.38. (a) SAD pattern of the $11\bar{3}\beta$ zone axis, (b) an enlarged schematic of (a) and (c) the accompanying $\bar{1}\bar{1}00_w$ DF image from the FZ of a specimen in the AW condition. The indices in red boxes correspond to the ω-phase. 100

Figure 3.39. (a) SAD pattern of the $11\bar{3}\beta$ zone axis, (b) an enlarged schematic of (a) and (c) the accompanying $\bar{1}\bar{1}00_w$ DF image from the FZ of a specimen heat treated at 804°C/1 hour. The reflections in red boxes correspond to the ω-phase. 102

Figure 3.40. (a) SAD pattern of the $11\bar{3}\beta$ zone axis and (b) an enlarged schematic of (a) from the FZ of a specimen heat treated at 700°C/4 hours. The indices in red boxes correspond to the ω-phase. 104

Figure 3.41. (a) SAD pattern of the $11\bar{3}\beta$ zone axis and (b) an enlarged schematic of (a) from the FZ of a specimen heat treated at 804°C/1 hour followed by aging at 600°C/4 hours. The indices in red boxes correspond to the ω-phase. 104

Figure 3.42. HAADF-STEM images of ω in the FZ of EBW Ti-5553 in the AW condition acquired in the $[110]_\beta$ beam direction. (a) original and (b) Fourier filtered. 106

Figure 3.43. (a) $[110]_\beta$ zone axis pattern acquired from the FZ of the EBW Ti-5553 specimen in the AW condition along with the (b) fast Fourier transform of Figure 1a and (c) an RGB composite created from three separate masks of the fast Fourier transform in (b) for the β matrix (blue), the ω1 variant (red), and the ω2 variant (blue). 107

Figure 3.44. HAADF-STEM image a ω particle with the surrounding β matrix indicating the rows (1, 2, 3) and direction in which the intensities can clearly be seen to vary due to atomic contrast. (a) original and (b) Fourier filtered. 109

Figure 3.45. Intensity profile in the 110β direction showing the tri-layer atomic ordering of the ω-phase in the FZ of EBW Ti-5553 in the AW condition. Rows 1, 2, and 3 are labeled above the peaks. The location from which the profile was acquired is indicated by the white box in Figure 3.43. 110

Figure 3.46. Schematic of the atomic arrangement in β (BCC), fully transformed, disordered ω (isothermal ω), and partially transformed, ordered ω as evidenced in the FZ of Ti-5553, left, center, right, respectively, with the 110β direction normal to the plane of the page. The red box represents an equivalent cell in each schematic. The tri-layering can be seen in the partially transformed and ordered ω. 111

Figure 3.47. Overlaid intensity profiles for rows 1, 2, and 3 as indicated in the insets acquired along the 111β direction in figure 3.48 from β to ω. 112

Figure 3.48. HAADF-STEM image of a ω precipitate and the surrounding β matrix wherein the atomic displacement within the ω-phase, a gradient of transition from β to ω, the coherency of the ω-phase with β, and distortion of the β lattice around the ω precipitate can be seen. (a) original and (b) Fourier filtered. 113

Figure 3.49. Representative secondary electron image of the fracture surface of an EBW Ti-5553 in the AW condition. The FZ (top half of image) shows indications of transgranular cleavage facets and the HAZ (bottom half) shows microvoid coalescence. The inset image of the FZ also shows clear signs of fine microvoid coalescence on the cleavage facets. 116

Figure 3.50. Representative secondary electron image of the fracture surface from an EBW Ti-5553 tensile specimen, which was heat-treated at 700°C/4h. The FZ (top half of image) exhibits evidence of transgranular cleavage facets and intergranular fracture and the HAZ (bottom half) shows microvoid coalescence. The inset image clearly shows the presence of microvoid coalescence on the fracture facets in the FZ (top half of image). 117

Figure 3.51. Representative secondary electron image of fracture surfaces from an EBW Ti-5553 tensile specimen, which was heat treated at 804 °C/1h. The FZ and HAZ (top half and bottom half of image, respectively) exhibit evidence of transgranular cleavage. The inset image clearly shows the presence of microvoid coalescence on the fracture facets. 117

Figure 3.52. Representative secondary electron image of fracture surfaces from an EBW Ti-5553 tensile specimen, which was heat-treated at 804 °C/1h followed by aging at 600 °C/4h. The FZ and HAZ (top half and bottom half of image, respectively)exhibit evidence of intergranular fracture. The inset image clearly shows the presence of microvoid coalescence on the fracture facets in the FZ (top half of image)..... 118

Figure 3.53. Cross-section of the fracture surface in Figure 3.49 showing fracture through the FZ (top) and HAZ (bottom) of the EBW Ti-5553 specimen in the AW condition. 121

Figure 3.54. Cross-section of the fracture surface in Figure 3.50 showing fracture through the FZ (top) and HAZ (bottom) of the EBW Ti-5553 specimen heat treated at 700°C/4h. 121

Figure 3.55. Cross-section of the fracture surface in Figure 3.51 showing fracture through the FZ (top) and HAZ (bottom) of the EBW Ti-5553 specimen heat treated at 804°C/1h. 122

Figure 3.56. Cross-section of the fracture surface in Figure 3.49 showing fracture through the FZ (top) and HAZ (bottom) of the EBW Ti-5553 specimen heat treated at 804°C/1h followed by aging at 600°C/4h. 122

Abstract

Within the last half-century, advances in Ti and Ti alloys have increased their popularity in the aerospace industry as well as in commercial products. Some Ti alloys have even replaced steels and Ni-base alloys due to their high strength and superior corrosion resistance. Of the various Ti alloys, near-β and metastable β alloys have become more common since their first large-scale use in the SR-71 Blackbird. In particular, TIMET's Ti-5Al-5V-5Mo-3Cr (Timetal Ti555, Ti-5553) gained high attainable strengths, excellent forging characteristics, and increased sensitivity to heat treatments compared to other β-Ti alloys. Ti-5553 has become widely known for its desirable attributes and has since become the baseline for the next generation of metastable β and near-β Ti alloys.

However, as well known as Ti-5553 is in the aerospace and Ti industry, its responses to welding have, for the most part, gone uncharacterized. The work presented in this dissertation investigates the influence of electron beam welding and post weld heat treatments on the microstructural, mechanical, and fracture responses of Ti-5553. In this study, Ti-5553 was electron beam welded and heat-treated in accordance to three predetermined heat treatments: 700°C for 4 hours followed by air cooling to room temperature, 804°C for 1 hour followed by air cooling to room temperature, and 804°C for 1 hour followed by air cooling to room temperature then aging at 600°C for 4 hours followed by air cooling to room temperature. Subsequently, the mechanical properties, microstructure, solute partitioning, precipitate identities, and fracture characteristics were evaluated.

With the use of traditional techniques and new technology it was shown that electron beam welded Ti-5553 in the as-welded condition and three post weld heat treatment conditions exhibited varying properties, distinctive to each of the corresponding microstructures. It was also found that the ω-phase played a large role in the evolution of the resultant microstructures and

mechanical properties in each of the four post-welding conditions. In general, ω-phase imparted brittle characteristics and acted as nucleation sites for fine scale, uniform α-phase precipitation. This investigation also reports the first atomic resolution high angle annular dark field scanning transmission electron microscopy images of ω-phase in a commercial metastable β-Ti alloy containing multiple alloying elements. The atomic resolution images of ω revealed unexpected atomic ordering. Typically ordering of "ω-like" phases is limited to titanium aluminides, making this the first report of observed ordering in Ti-5553. This ordering likely accounts for the increased brittle behavior of the weld zone compared to bulk Ti-5553.

1. Introduction

1.1. Titanium and its Alloys

Titanium (Ti) was first discovered in Cornwall, England by William Gregor in 1791 to exist as an oxide in ilmenite ($FeO\text{-}TiO_2$), magnetic iron sand. It wasn't until 1795 that this element was named by Martin Heinrich Klaproth, when he identified it while analyzing rutile (TiO_2) the same unknown element as reported by Gregor. Klaproth named the element titanium after the Titans of Greek mythology. Pure Ti does not occur naturally and must be extracted from its ores. An impure sample of Ti was first isolated in 1825, but it wasn't until 1937 that pure Ti in any significant quantity was produced. Kroll successfully reacted $TiCl_4$ with molten Mg under an Ar atmosphere to produce pure Ti, with what is now known as the Kroll process. The general reaction is shown in equation 1.1. Since the invention of the Kroll process, the production of Ti has gone relatively unchanged and uses for Ti and its alloys have expanded into many industries, particularly aerospace and weight-critical applications.

$$4TiCl_{4\,(gas)} + 2Mg_{(liquid)} \xrightarrow{yields} 4Ti_{(solid)} + 2Mg\ Cl_{2\,(liquid)} \quad \text{Eq. 1.1}$$

Elemental Ti belongs to Group 4 of the periodic table, has an atomic number of 22, and has an atomic mass of 47.87 g/mol. Its electronic configuration is $1s^2\ 2s^2\ 2p^6\ 3s^2\ 3p^6\ 3d^2\ 4s^2$, giving it an incomplete 3d shell that allows it to form solid solutions with many substitutional elements having a size factor within ±20% [Polmear, 1995]. Occurring primarily in ore as rutile and ilmenite, Ti is the ninth most abundant element (0.66%) in the Earth's crust behind O, Si, Al, Fe, Ca, Na, K, and Mg. Among Ti's most notable physical characteristics are its corrosion resistance, high strength to weight ratio, and relatively high melting point at 1668°C (1941K). Compared to iron and some low grade steels, pure Ti has a higher melting point (Fe: 1538°C, Ti: 1668°C) and can achieve higher ultimate tensile strengths (UTS). At 882.5°C (the β-transus temperature of pure Ti), Ti undergoes an allotropic transformation from a low temperature, hexagonal close packed (HCP) α-phase to the high temperature, body centered cubic (BCC) β-

phase that remains stable up to the melting point. However, the addition of certain alloying elements may favor the stabilization of either α- and/or β-phase and result in an alloy, which is heat treatable. The following sections describe the three different alloy types, commonly observed in Ti as well as phase transformations and an overview of Ti-5553 is given.

1.1.1. Titanium Alloy Classification

Titanium alloys are classified into three simple types based on the effects that alloying elements have on the β-transus temperature, in the Ti-rich portions of pseudo-binary phase diagrams (Figure 1.1). The three types are α stabilizer, β stabilizer, and neutral. Elements, such as Al and O, that dissolve in the α-phase, raise the β-transus temperature by expanding the α-phase field. This stabilizes the α-phase and favors the α-stabilizer type. Al, the most widely used alloying element in Ti, is a strong α-stabilizer because it raises the β-transus temperature and has large solubilities in both the α- and β-phases. The β-stabilizer type, on the other hand, consists of β-stabilizing elements that depress the β-transus temperature and are classified in two groups: those that form the β-isomorphous type and those that promote formation of a β-eutectoid. Examples of such elements are Mo, V, Nb, W, and Ta (pertaining to the former) and Fe, Mn Cr, Ni, Cu, Si, Co, and H (pertaining to the latter) of which Mo and W have the strongest effects. The eutectoid reaction, however, is very sluggish in many alloys and is almost undetectable [Polmear, 1995]. The neutral type includes alloying elements, such as Zr, Hf, and Sn and has neutral effects on the β-transus temperature. Zr and Hf are also isomorphous with Ti and exhibit the same allotropic phase transformation from β to α. These neutral alloying elements initially lower the β-transus temperature slightly, but increase it at higher concentrations [Lütjering and Williams, 2007].

It is conventional, however, to group the alloys according to a combination of traits. Characteristics, such as the phases formed upon cooling (stable or metastable), effects of alloying elements (α- or β-stabilizing), and β-transus temperature, are more typical ways, with which to

classify Ti alloys. Their position on a pseudo-binary section through a β-isomorphous phase diagram, shown schematically in Figure 1.2, further delineates the groups. Therefore, Ti alloys are commonly grouped in one of the following three categories: α alloys, α+β alloys, or β alloys. These groups are discussed in the subsequent sections.

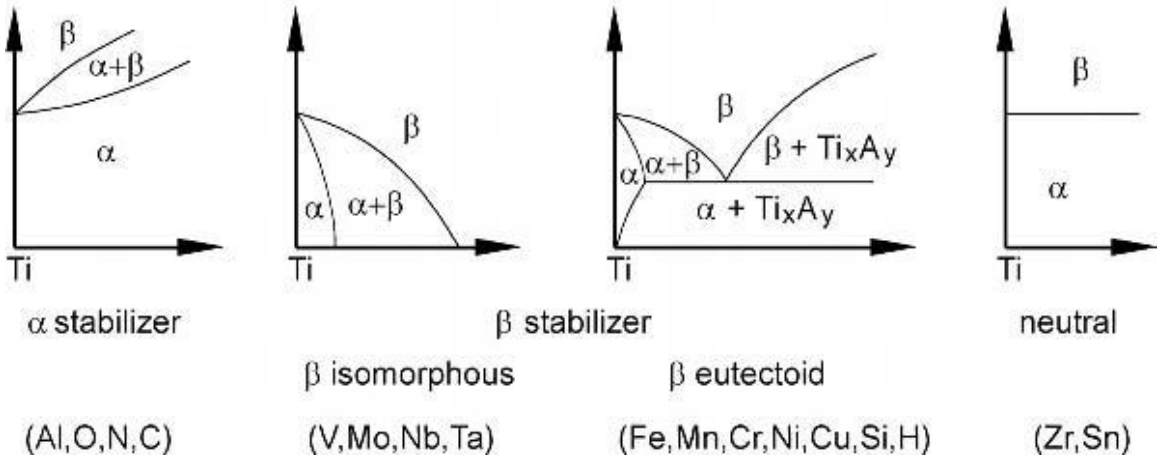

Figure 1.1. Schematic pseudo-binary phase diagram of the Ti-rich sections showing the effects of (left to right) α stabilizing elements, β stabilizing elements (isomorphous and eutectoid), and neutral elements on the β-transus temperature and phase regimes [Lütjering and Williams, 2007].

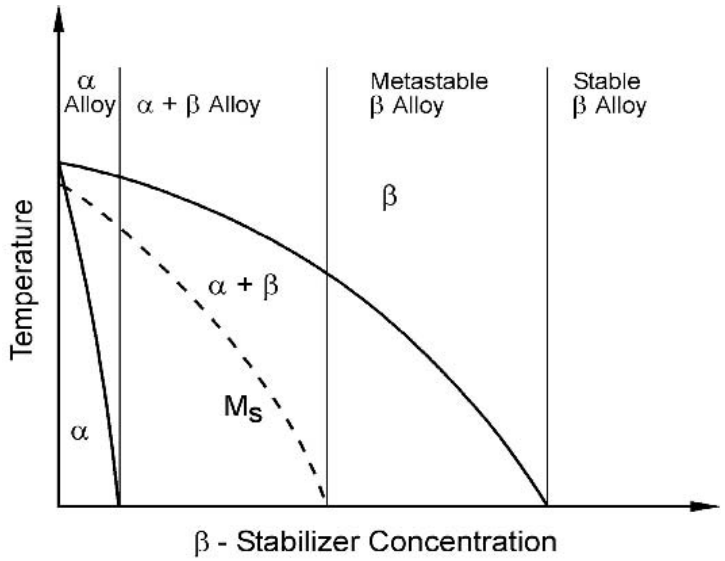

Figure 1.2. Schematic representation of a pseudo-binary section through a β-isomorphous phase diagram indicating regions pertaining to α alloys, α+β alloys, and β alloys (metastable and stable β alloys) [Luutjering and Williams].

1.1.1.1. α Alloys

The α alloys consist of commercially pure (CP) Ti and low alloy Ti. The alloying elements commonly present in α alloys are Al and O, which dissolve in the α-phase, and the neutral elements, Zr and Sn. All of these elements cause solid solution hardening and increase tensile strength by 35 MPa to 70 MPa for each one percent of added element [Polmear, 1995]. O and N provide interstitial hardening as impurities, but controlled additions of O can be used to provide specific ranges of strength in CP Ti. Alloying elements such as Pd, Nb, and Ru impart significant improvements on corrosion resistance of CP Ti. In general, small additions of other elements can be present, which alter the microstructure and mechanical properties and lead to the α alloys being further divided into fully-α, near-α, and age-hardenable.

Fully-α alloys consist of CP Ti, essentially Ti-O, and alloys containing small amounts of Al and the neutral elements. These alloys are characterized by equiaxed α grains formed from working and subsequent annealing in the α-phase regime, martensitic α (α′) due to quenching from above the β-transus temperature, or Widmanstätten α due to slow cooling from above the β-transus temperature. Fully-α alloys have good creep resistance, but inferior tensile strength and formability due to the presence of completely single-phase (HCP α) microstructures.

In order to increase the ductility of fully-α alloys and improve the tensile strengths, small additions of β stabilizers can be added. These alloys are known as near-α alloys and contain less than 2 wt.% of β stabilizing elements and in some alloys Si is also added. The addition of β stabilizing elements such as Mo and Fe, promotes the formation of very small volume fractions of β-phase in between α plates, which delineate the α-phase and cause a basket weave configuration of the Widmanstätten structure. Near-α alloys display the greatest creep resistance of any Ti alloy and possess greater degrees of formability and higher room temperature tensile strengths than fully-α alloys. Not only does the ductility and strength improve, but also the response to heat treatments.

Age-hardenable α alloys, and Ti alloys that are age-hardenable in the classic sense, are rare. Ti-2.5Cu (IMI 230) was developed as a heat treatable β-eutectoid sheet material. It was capable of being hardened by the traditional process of solution treatment, air-cooling/oil-quenching to room temperature, then aging at intermediate temperatures. This process promotes the formation of finely dispersed Ti_2Cu precipitates that are coherent with the β matrix. This alloy, however, has little significance as a commercial β-eutectoid system or as an age-hardenable α alloy.

In general, there is a practical limit to the amount of α-stabilizing elements, as well as other alloying elements, that can be added to Ti. Ti alloys tend to become brittle when the Al equivalent ($[Al]_{eq}$) exceeds 9% due to an ordering reaction. The Al equivalent is as follows [Rosenberg, 1970]:

$$[Al]_{eq} = \frac{1}{3}[Sn] + \frac{1}{6}[Zr] + 10([O] + [C] + 2[N]) \qquad \text{Eq. 1.2}$$

α-alloys, however, cannot have more than 5-6 wt.%Al added to them due to the formation of a finely dispersed, ordered phase known as α_2 (Ti_3Al). It is coherent with the lattice of the α-phase over a wide range of temperatures and causes brittle behavior in Ti alloys. Other elements such as Sn and Zr can be added to promote solid solution strengthening, but at the expense of increasing the alloy's density. Sn can also replace Al in α_2 of Ti-Al-Sn alloys, creating Ti_3Sn. The addition of Sn also induces greater lattice misfit between the precipitates and the matrix, which hinders α_2 nucleation and has a slightly less deleterious effect on ductility [Polmear, 1995].

1.1.1.2. $\alpha+\beta$ Alloys

α+β alloys, like the name implies, are Ti alloys with compositions that favor the formation of both the α and β phases. Compared to the α-alloys, they offer higher tensile strengths, better formability, and good fatigue strength, but sacrifice creep strength above 300°C-400°C due to the BCC crystal structure and ease of precipitation hardening [Polmear, 1995; Nag, 2008]. This class of alloys contains elements to stabilize and strengthen the α-phase as well as 4-

6 wt.% β-stabilizing elements that allow significant amounts of β-phase to be retained upon quenching from the β or α+β phase fields. Their compositions range from the α/α+β phase boundary to the martensite start line (M_s) at room temperature on the pseudo-binary section of the β-isomorphous phase diagram in Figure 1.2. In all instances of α+β alloys, no amount of fast cooling can produce a 100% β microstructure, rather α and martensitic variants of α with some amounts of retained β may form. α+β alloy Ti-6Al-4V (Ti-64) has been shown to contain up to 15 vol.% β-phase upon quenching [Polmear, 1995].

Unlike α-alloys, α+β alloys respond to tempering or aging heat treatments, which can increase their room temperature tensile strengths significantly. The two most common heat treatments are the β processing and α+β processing treatments. Each of which are named for the temperature ranges at which the heat treatments may be carried out. A typical β processing treatment consists of three stages: (i) cooling from above the β-transus (solutionizing temperature), (ii) heating into the α+β phase regime and holding at the annealing temperature and subsequently cooling, and (iii) stabilizing to essentially form an equilibrium structure [Lütjering and Williams, 2007]. Depending on the cooling rate from the β-phase regime (slow or fast) different microstructures form. Under slow cooling conditions colonies of uni-variant α laths over wide regions are formed, referred to as a colony microstructure. Under fast cooling conditions a basketweave-type structure is formed, wherein multi-variant α laths nucleate and grow. β-phase is present between the α laths in each case. In a α+β processing treatment, three stages are also typical: (i) cooling from the β solutionizing temperature, (ii) mechanical working in the α+β phase regime, and (iii) stabilizing, like that of the β processing treatment. A bimodal structure with equiaxed grains of α and transformed β (Widmanstätten α) may be achieved. During the stabilization stages in both processing treatments alloy partitioning occurs, which increases the high temperature stability of the α and β phases. Decomposition of β occurs during the aging or elevated temperature stages of each type of processing. β transforms into martensitic

variants of α, similar to the transformation observed in α-alloys. Because α+β alloys are responsive to heat treatments, which can give them a wide range of properties, they are the most common Ti alloys in use [Donachie, 2000].

1.1.1.3. β Alloys

β alloys are defined as Ti alloys containing enough total β-stabilizing elements to retain a fully β structure upon quenching from above the β-transus temperature. This implies that a sufficient β-stabilizer content exists to avoid passing through the M_s line (denoted by a dotted line in Figure 1.2). It is commonly accepted that the alloys, whose compositions lie between the M_s line at room temperature and the intersection of the α+β/β phase boundary line at room temperature, are referred to as metastable β alloys. They are considered metastable because of their tendency to precipitate a second phase upon aging. More highly alloyed compositions that lie beyond the α+β/β phase boundary are called stable β alloys and aren't hardenable by heat treatment. As a result, they are not typically used as structural components [Polmear, 1995].

As stated previously, the frequently used β-stabilizing elements are: Mo, V, Nb, W, and Ta (β-isomorphous) and Fe, Mn Cr, Ni, Cu, Si, Co, and H (β-eutectoid). The critical minimum concentration of each element to fully stabilize β (β_c) as well as the effects of these elements on suppressing the β-transus temperature are presented in Table 1.1. Of these β-stabilizers, Mo is well known and a relatively strong β-stabilizer, which has arbitrarily been designated as a baseline [Bania, 1994]. Therefore, a Mo equivalent ($[Mo]_{eq}$) is used to define β alloys, which provides a convenient manner to consider the overall β-stability of an alloy with various alloying additions [Bania, 1994]. The $[Mo]_{eq}$ can be defined as follows:

$$[Mo]_{eq} = 1.0(wt.\%Mo) + 0.67(wt.\%V) + 0.44(wt.\%W) + 0.28(wt.\%Nb) + 0.22(wt.\%Ta) + 2.9(wt.\%Fe) + 1.6(wt.\%Cr) - 1.0(wt.\%Al) \quad \text{Eq. 1.3}$$

The constants before each alloying element reflect the ratio of the β_c for Mo (10 wt.%) divided by the β_c for the specific element (β_c values may be found in Table 1.1). Al is subtracted to reflect its opposing tendency to stabilize α. Generally, a $[Mo]_{eq}$ of 10 wt.% or greater is required to stabilize β upon quenching. However, it should be noted that some alloys having a $[Mo]_{eq}$ less than 10 wt.% are still able to retain 100% β upon quenching, albeit metastable [Bermingham et. al., 2009; Bania, 1994]. This is also evident in the β_c values expressed in Table 1.1.

Table 1.1. Common β-stabilizing elements and their critical minimum contents required to retain fully β structures upon quenching as well as their effects per wt.% of addtion on suppressing the β-transus temperature in binary Ti systems (recreated from Bania, 1994).

β-Stabilizer	Type	β_c (wt.%)	β_t Suppression (°C)
Mo	Isomorphous	10.0	-8.3
V	Isomorphous	15.0	-5.5
W	Isomorphous	22.5	-13.8
Nb	Isomorphous	36.0	-10.6
Ta	Isomorphous	45.0	-15.6
Fe	Eutectoid	3.5	0
Cr	Eutectoid	6.5	-2.8
Cu	Eutectoid	13.0	-5.6
Ni	Eutectoid	9.0	4.4
Co	Eutectoid	7.0	3.3
Mn	Eutectoid	6.5	4.4
Si	Eutectoid	–	21.1

β alloys are also classified as solute lean and solute rich alloys. Solute lean β alloys have a greater tendency to precipitate a second phase, either α or ω (see section 1.2.1 and 1.2.2 for a more detailed discussion of these phases). The β matrix readily decomposes due to the lean β-stabilizer content. During heat treatment above the β-transus, solute lean alloys exhibit a β matrix, which is somewhat unstable [Nag, 2008]. In general, as the solution treatment temperature or heat treatment temperature is decreased, the β matrix becomes richer in β-stabilizing elements due to the formation of primary α and the rejection of β-stabilizing elements from α to the β matrix. This causes the matrix to become more stable and reduces the driving force for further decomposition of β during subsequent quenching and aging [Lütjering and Williams, 2007]. In lean β alloys there are two types of quenching transformations that have

been observed: athermal ω and α″, which arise due to the decomposition of β. While providing little strengthening effects, athermal ω and α″ serve as precursors for precipitation during aging. At low aging temperatures isothermal ω is precipitated, which also promotes the precipitation of α on further aging. Most alloys are over-aged or heat-treated in the α+β phase regime to reduce the amount of fine ω-phase particles that cause low ductility. By reducing the volume fraction of ω and somewhat coarsening α, a better combination of strength and ductility may be achieved. In all cases of solute lean alloys, however, the formation of grain boundary α cannot be avoided by processing [Nag, 2008; Lütjering and Williams, 2007; Polmear, 1995]. Common solute lean β alloys are given in Table 1.2.

Table 1.2. Common solute lean and solute rich β alloys and their corresponding nominal compositions.

	Alloy Name	Al (wt.%)	Sn (wt.%)	Zr (wt.%)	Mo (wt.%)	V (wt.%)	Cr (wt.%)	Fe (wt.%)	Nb (wt.%)	Si (wt.%)
Solute Lean	Ti6246	6	2	4	6	–	–	–	–	–
	Ti-17	5	2	2	4	–	6	–	–	–
	β-CEZ	5	2	4	4	–	2	1	–	–
	Ti-10-2-3	3	–	–	–	10	–	2	–	–
Solute Rich	Ti8823	3	–	–	8	8	–	2	–	–
	Beta 21S	3	–	–	15	–	–	–	2.7	0.2
	Ti-15-3	3	3	–	–	15	3	–	–	–
	Beta C	3	–	4	4	8	6	–	–	–

Solute rich β alloys are heavily stabilized β-Ti alloys, which are so stable that the β matrix does not decompose to the β/ω structure as in solute lean alloys [Lütjering and Williams, 2007]. Examples of some solute rich alloys are listed in Table 1.2. Because of the high solute content of β-stabilizing elements, the β-transus of solute rich alloys is suppressed to temperatures below 800°C and it becomes increasingly difficult for β-stabilizing elements to diffuse during the formation of α precipitates. Therefore, α nucleation kinetics is sluggish, making aging treatments impractical for industrial applications [Nag, 2008]. Just as in solute lean alloys, grain boundary α is also unavoidable in solute rich alloys; however, it is more favorable to form as solute concentration increases. This leads to low toughness in these alloys.

1.2. Phases in Titanium

Multiple phases exist in Ti and Ti alloys depending on temperature, pressure, cooling rate, deformation, and alloying elements. These phases are categorized as equilibrium or non-equilibrium phases. When conditions for steady state are reached for equilibrium phase formation, the minimization of Gibbs free energy governs phase stability. In contrast, when non-equilibrium conditions are imposed, such as high heating rates or cooling rates, metastable phases form that do not possess the lowest Gibbs free energy. In non-equilibrium cases, kinetics is the driving force behind phase transformations. However, when conditions become favorable, the metastable phases give way to more stable ones, wherein the Gibbs free energy is minimized.

1.2.1. Equilibrium Phases

Of the equilibrium phases in Ti and Ti alloys, α and β are the most common and dominant, but others exist in many alloys. The other phases pertaining to the equilibrium phases are intermetallics and ordered phases (B2, α_2, γ, O, $B8_2$) that have been observed in Ti alloys. The equilibrium Ti phases are discussed in the following sections.

1.2.1.1. α

α-Ti is the most stable form of pure Ti at room temperature and pressure [Donachie, 2000]. With atoms located at the (0,0,0) and (1/3, 2/3,1/2) positions in its unit cell, it has a HCP crystal structure with $P6_3mmc$ symmetry. The lattice parameters of α are 0.468nm and 0.295nm for the c and a axes, respectively, which gives a c/a ratio of 1.587, slightly less than the ideal c/a ratio (1.633) [Lütjering and Williams, 2007]. A schematic of the α unit cell is shown in Figure 1.3. The most densely packed plane in the HCP crystal is the basal plane, i.e. (0001) or (0002) as indicated in Figure 1.3, with a_1, a_2, and a_3 being the close packed directions ($\langle 11\bar{2}0\rangle$). The HCP crystal structure leads to an inherently anisotropic crystal wherein a single crystal of pure α-Ti at room temperature exhibits varying elastic moduli between 145 GPa (parallel to the c-axis) and 100 GPa (perpendicular to the c-axis). Variances in the shear modulus also exist in single crystal α from 46 GPa to 34 GPa when stress is applied in the $\langle 11\bar{2}0\rangle$ direction in the (0002) and

$\{10\bar{1}0\}$ planes, respectively. However, in polycrystalline α, the variations are not as dramatic. When precipitated during cooling from above the β-transus, α is commonly referred to as primary α, whereas finer α precipitated during heat treatments below the β-transus is referred to as secondary α. Precipitated α can take on multiple morphologies depending on prior deformation, alloy content, deformation temperature, and parent phase morphology. Typically α precipitates are found as clusters of invariant laths (colony) or multiple crystallographic variants growing together (basketweave), depending on cooling rate [Lütjering and Williams, 2007].

Like most HCP metals, deformation α-Ti is limited by the number of available slip systems. Deformation is most commonly accommodated by slip in the basal plane in the $\langle 11\bar{2}0\rangle$ direction and in the three $\{10\bar{1}0\}$ planes, as well as in the six $\{10\bar{1}1\}$ planes [Polmear, 1995]. This results in only four independent slip systems, where five are needed for homogeneous deformation based on the Von-Mises criteria. In order to activate the fifth slip system, energy must be introduced by raising the temperature of the system. At elevated temperatures a combination of basal and prismatic slip occurs in the $\{11\bar{2}2\}$ plane in the $\langle 11\bar{2}3\rangle$ direction. However, when slip cannot occur, twinning accommodates deformation in α-Ti. Common twinning modes are $\{10\bar{1}2\}$ and $\{11\bar{2}1\}$ in tension and $\{11\bar{2}2\}$ in compression [Lütjering and Williams, 2007].

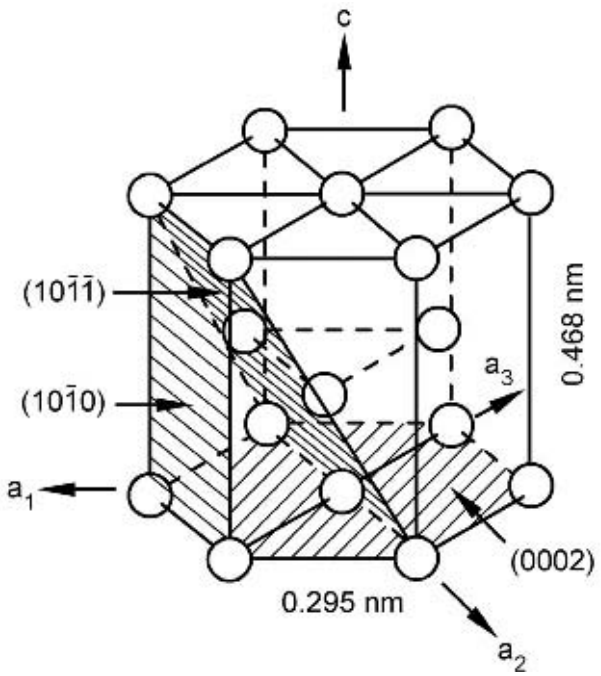

Figure 1.3. Schematic of the α unit cell in pure Ti with one of each of the corresponding closed packed planes (0002)*, prismatic planes* $(10\bar{1}0)$*, and pyramidal planes* $(10\bar{1}1)$ *[Lütjering and Williams, 2007].*

1.2.1.2. β

Above 882.5°C, pure Ti undergoes an allotropic transformation from HCP α to BCC β, which is stable up to the melting point. The BCC β unit cell (Figure 1.4), whose space group is $Im\bar{3}m$, contains a total of two atoms, which are positioned at (0,0,0) and (1/2,1/2,1/2). The lattice parameter for pure Ti as β is 0.332 nm [Lütjering and Williams, 2007]. β is more stable at elevated temperatures because it is a more open structure (BCC atomic packing factor = 0.68 versus HCP atomic packing factor = 0.74), which permits it to accommodate the higher vibrational entropy present at higher temperatures [Lütjering and Williams, 2007]. Unlike single crystal α, single crystal β is not anisotropic and exhibits equal elastic and shear moduli in each of the three principle crystallographic directions. The elastic modulus of single crystal β is 58 GPa while the shear modulus is 20 GPa [Lütjering and Williams, 2007]. However, these moduli were determined at elevated temperatures, due to β only being stable in pure Ti at temperatures above the β-transus. In polycrystalline β phase, the elastic constants, c_{11}, c_{12}, and c_{44}, are relatively independent of temperature [Ogi, et al., 2004].

As discussed in section 1.1.1.3 the addition of certain elements, known as β-stabilizers (Mo, V, Nb, W, Ta Fe, Mn Cr, Ni, Cu, Si, Co, H), decreases the β-transus temperature, which stabilizes the β-phase at lower temperatures. At certain concentrations in binary Ti alloys or above $[Mo]_{eq}$=10 wt.% (Equation 1.3) in multi-element Ti alloys, 100% retention of the β-phase may be achieved upon cooling from above the β-transus to room temperature (Table 1.1). Because these elements are substitutional, except for H, the lattice parameters of β in Ti alloyed with β-stabilizing elements may differ from that of pure β in unalloyed Ti.

Deformation of β is homogeneous compared to HCP α. In BCC metals, 48 slip systems are active, which satisfies the Von-Mises criteria for homogeneous deformation. Slip in BCC β occurs mostly on the {110} close packed planes, but also occurs on the {112} and {123} planes. These planes, while not being the most densely packed, come close to being as densely packed as the {110} plane. The slip direction in each case is the ⟨111⟩ direction. This results in a total of 48 slip systems able to accommodate deformation in β-Ti. Similar to HCP α, twinning also occurs in β. The twin systems available to β are {332}⟨113⟩ and {112}⟨111⟩ [Duerig, et al., 1984].

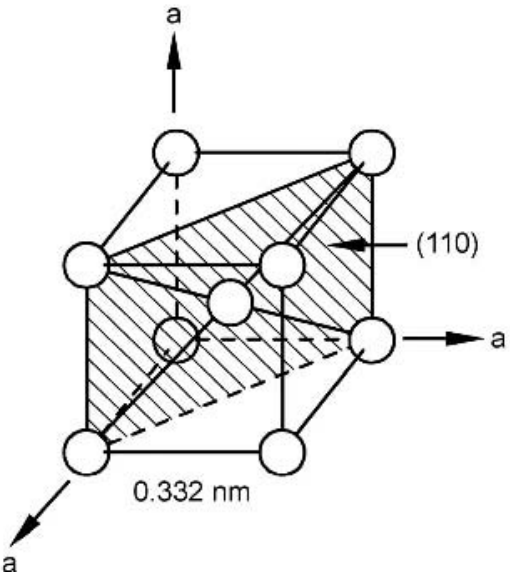

Figure 1.4. Schematic of the β unit cell in pure Ti with one of the corresponding close packed planes (110) *[Lütjering and Williams, 2007].*

1.2.1.3. B2

The B2 structure, also known as the CsCl structure, is made up of two interpenetrating BCC lattices of different elements. The corner of the first lattice is the body centered atom of the second lattice, whose corner atoms are the body centered atoms of the first lattice, thereby making it an ordered phase belonging to the $Pm\bar{3}m$ space group. In specific relation to Ti, the B2 structure may be found in some ternary Ti-aluminides and nickelides (TiNi shape memory alloy). However, unlike regular BCC β, B2 structures like that found in Ti-25Al-15Nb are extremely brittle due to the rapid decomposition and ordering of β during quenching to form B2 [Strychor, et al., 1982].

1.2.1.4. α_2

α_2, another ordered Ti phase, is hexagonal and has a DO_{19} crystal structure. This phase is coherent with the α matrix and serves to harden the α phase by precipitation hardening when the Al content reaches or exceeds approximately 5 wt.% and above. α_2 most commonly occurs as Ti_3Al, but in some instances Sn, Ga, or In may substitute in for Al. Hardening by precipitation of α_2 occurs primarily because dislocations must shear through the particles rather than slip or climb around them. As the particles coarsen they become ellipsoidal and their long axis grows parallel to the c-axis of the hexagonal lattice [Blackburn, 1968]. α_2 is found in α+β alloys, such as Ti-6Al-4V, IMI 685, Ti-6242, and IMI 834 [Lütjering and Williams, 2007].

1.2.1.5. γ

In the Ti-Al system the equilibrium intermetallic phase, γ (TiAl), exists at 50 at.% Al. γ has an $L1_0$ structure, which consists of alternating (001) planes of Ti and Al and creates long range order leading to tetragonal distortion of the disordered face centered cubic (FCC) lattice [Schectman, et al., 1974]. Schectman et al. [Schectman, et al., 1974] showed that the presence of

this order decreased the overall ductility of polycrystalline γ. However, γ alloys are relatively better suited to high temperate applications than other Ti-aluminides.

1.2.1.6. O

O, based on the Ti_2AlNb composition, is an intermetallic compound with an ordered orthorhombic structure. This orthorhombic phase forms at higher Nb concentrations (12.5-24% Nb) in Ti-25Al-Nb alloys. O is similar to α_2, but the size difference between the Nb and Al atoms causes the structure to have unequal axis lengths along rows that contain Ti and Nb and Ti and Al. Therefore, the O structure is distorted from hexagonal to orthorhombic [Lütjering and Williams, 2007]. The O phase forms in Nb rich regions, which are a result of solute rejection from α_2 during slow cooling. The Nb rich regions then order into the Ti_2AlNb orthorhombic phase [Muraleedharan et al., 1995]. Ti alloys containing 18-30 at.% Al and 18-34 at.% Nb exhibiting microstructures of O and a combination of β and B2 have been shown to have excellent mechanical properties at ambient and elevated temperatures [Banerjee, et al., 1988].

1.2.1.7. $B8_2$

In Ti-Al-Nb systems there is another phase, $B8_2$, found to be in equilibrium with γ, α_2, and O. Its composition is close to Ti_4Al_3Nb and has the same structure as the ω-type phases ($B8_2$) [Bandersky, et al., 1990]. $B8_2$ forms at high temperatures as pairs of [111] planes are displaced in the B2 phase, in which chemical ordering then takes place.

1.2.2. Non-Equilibrium Phases

Non-equilibrium phases are those that form under conditions that do not promote equilibrium phases, i.e. fast heating or cooling. During fast heating or cooling, long range diffusion is inhibited due to the decreased time allowed for the rearrangement of atoms to form stable phases. Because diffusion is limited, shuffle and martensitic transformation reactions take place. In these instances kinetics tends to dominate phase formation, while the system makes concessions in terms of thermodynamics to account for the non-equilibrium conditions. The non-

equilibrium phases in Ti and Ti alloys are α′, α″, ω, and β′, which will be discussed in the following sections.

1.2.2.1. α′

α′ forms due to very rapid quenching from the β phase through a martensitic transformation. Martensitic α′ is a supersaturated α phase that forms due to a diffusionless transformation [Lütjering and Williams, 2007], which has a hexagonal structure and belongs to the $P6_3mmc$ space group. Depending on the solute content of the alloy, α′ can occur in a variety of morphologies: colonies of laths, lenticular, or twinned plate structures. α′ typically forms in dilute alloys and has even been observed to form in Ti-Mo alloys. In Ti-Mo alloys, Flower et al. [Flower et al., 1983] found that α′ formed in systems containing up to 4 wt.% Mo. However, above 4 wt.% Mo, α″ formed until the concentration of Mo reached levels that suppressed all α′ and α″ transformations and 100% β was retained. Ho et al. [Ho et al. 1999] found similar results in Ti-Mo alloys and reported that at Mo concentrations of 10 wt.% and greater, β phase was retained. Thus, even with β-stabilizing elements being the only alloying additions, it is possible to achieve martensitic transformations when the β-stabilizer content is below the required minimum to retain the β-phase upon cooling.

1.2.2.2. α″

Similarly to α′, α″ is a result of the martensitic transformation of β during rapid quenching. α″ forms in alloys with higher solute contents compared to alloys in which α′ forms, but can also form due to applied external pressure or strain [Duerig et al. 1984]. α″ has an orthorhombic crystal structure, which is similar to the hexagonal structure exhibited by α′, but favorable at higher alloy contents wherein the constraints of the hexagonal structure cannot be met [Duerig et al., 1980]. The distinction between whether α′ or α″ will form is unclear, because the martensite start temperatures lie on top of one another in binary phase diagrams [Dobromyslov et al., 2001]. One way to determine which martensitic variant of α will form is to

calculate the electron-to-atom ratio for the alloy as described by Bagariatskii et al. [Bagariatskii et al., 1959]. Electron-to-atom ratios between 4.0 and 4.07 favor the formation of α′ and ratios greater than 4.07 were found to favor the formation of α″ [Cotton et al., 1994]. The electron to atom ratio is more of a guideline than a strict rule to predict the formation of α′ and α″.

1.2.2.3. ω

The first observed presences of ω was reported by Frost et al. [Frost, et al., 1954] in their work on isothermal transformations in Ti-Cr alloys. ω phase has since been determined to form during rapid cooling from the β phase regime and during isothermal heat treatments in Ti and Zr alloys that can retain 100% β at low temperatures, which also contain significant amounts of β-stabilizers [Hickman, 1969b; Lütjering and Williams, 2007]. More specifically, ω formation depends on three criteria: (i) upon quenching of alloys with compositions close to the lower limit of 100% retention of β, (ii) during aging of alloys with higher β-stabilizer contents within the temperature range of 100-500°C, and (iii) during room temperature deformation [Hickman, 1969b]. However, there are exceptions to these criteria. Jamieson found that under pressure, the transformation to ω from α in pure Ti and Zr was complete at room temperature and after removal of the pressure, ω remained stable [Jamieson, 1963]. Hickman reported that ω did not form in Ti-Nb systems when rapidly quenched, because α′ and α″ formed first. But on reheating of the quenched alloys, ω precipitated and could be retained by cooling back to room temperature [Hickman, 1969a]. In relation to deformation, Silcock et al. [Silcock et al., 1958] showed that deformation had no effect on the amount of ω phase formed in two binary Ti alloys containing 20 wt.% V and 13 wt.% Mo, respectively. It was proposed by Wood [Wood, 1963], in his work on the deformation of a Ti-15 wt.% Mo alloy, that what was observed by Silcock et al. is due to the formation of martensitic α in the early stages of deformation and formation of ω in fine grain specimens after 5% deformation.

Depending on the extent of transformation, ω has been identified to exist as two types that are coherent with the BCC β matrix: athermal and isothermal. During cooling athermal ω (incomplete transformation yielding trigonal symmetry) forms, while aging or isothermal holds cause isothermal ω (complete transformation yielding hexagonal symmetry) to form. The transformation of β to ω is discussed in section 1.3.2. The two forms of ω have the same lattice parameters, but different crystal symmetries, a=0.282 nm and c=0.460 nm, [Silcock et al., 1956; Bagariatskii et al., 1955]. Bagariatskii et al. suggested ω belonged to the $P\bar{3}m1$ space group with atom positions at (0,0,0) and (±2/3,1/3,μ), where μ=0.48±0.01, whereas Silcock et al. thought ω belonged to the $P6/mmm$ space group with atom positions at (0,0,0) and (±2/3,1/3,1/2) [Silcock et al., 1956; Bagariatskii et al., 1955]. Both research efforts agree that ω is hexagonal in its completely transformed state.

ω can be present in two morphologies, cuboidal or ellipsoidal. The cuboidal morphology occurs when the mismatch between the particle and β matrix is high, whereas ellipsoidal particles occur when that mismatch is low. Cuboidal particles have cube faces that grow parallel to the $\{100\}$ planes of the β phase. Ellipsoidal particles have long axes that grow parallel to the $\langle 111\rangle$ directions of the β phase. When ω is present in high volume fractions in either morphology, it causes embrittlement of the alloy. This is due to dislocations having no mobility in ω [Polmear, 1995]. ω particles are coherent with the β matrix and are sheared by moving dislocations, which results in the formation of intense, localized slip bands leading to early crack nucleation and low ductility [Gysler et al., 1974].

1.2.2.4. β′

Just as the other non-equilibrium phases form and give way to other phase transformations as β-stabilizer content increases (i.e. β to α, β to α′, β to α″, and β to ω), β′ becomes stable in solute rich β-Ti alloys. In the case of β′ precipitation, the β phase undergoes a phase separation reaction that results in β1 and β2 phases. β1 and β2 have BCC crystal

structures, but different lattice parameters. The difference in lattice parameters arises due to β2 being solute rich and β1 being solute lean. Conventionally, β1 and β2 are referred to as β and β′, respectively [Duerig et al., 1984]. The phase separation reaction from which β′ forms, can occur by traditional nucleation and growth or spinodal decomposition [Lütjering and Williams, 2007].

1.3. Phase Transformations in Titanium

Of all the possible phase transformations in Ti and Ti alloys, those most relevant to the current work will be discussed in detail. These phase transformations include the diffusional transformation of β to α, the shuffle transformation of β to ω, and the decomposition of ω to α.

1.3.1. β to α

The diffusional transformation of β to α occurs in all Ti alloys and it is the α-phase that affects the majority of an alloy's mechanical properties. Upon transformation of β to α, there are multiple orientations with respect to the β-phase that promote α nucleation and growth and are preferred due to the minimization of interfacial energy between the two phases. These orientation relationships (OR) are as follows:

Burgers OR: $(0001)_\alpha // \{011\}_\beta ; \langle 11\bar{2}0\rangle_\alpha // \langle 1\bar{1}1\rangle_\beta ; \{1\bar{1}00\}_\alpha // \{121\}_\beta$

Pitsch-Schrader OR: $(0001)_\alpha // \{011\}_\beta ; \langle 11\bar{2}0\rangle_\alpha // \langle 100\rangle_\beta ; \{1\bar{1}00\}_\alpha // \{0\bar{1}1\}_\beta$

Potter OR: $(0001)_\alpha\ 2° \mathit{from} \{011\}_\beta ; \langle 11\bar{2}0\rangle_\alpha // \langle 1\bar{1}1\rangle_\beta ; \{1\bar{1}01\}_\alpha // \{110\}_\beta$

Rong-Dunlap OR: $(0001)_\alpha // \{021\}_\beta ; \langle 11\bar{2}0\rangle_\alpha // \langle 100\rangle_\beta ; \{1\bar{1}00\}_\alpha // \{0\bar{1}2\}_\beta$

Of these four ORs, the Burgers OR is most commonly observed between α and β [Nag, 2008]. Each OR of α can be considered a different variant of α when present as a result of the same nucleation event.

There are three possible types of α that can form in β-Ti alloys. They are classified by the location at which they form: along β/β grain boundaries (allotriomorph), from the grain boundary into the β grain (intergranular), and throughout the β grain interior (intragranular).

Allotriomorph α precipitates by the kink-on-ledge mechanism as reported by Furuhara et al. [Furuhara, et al., 1991]. Intergranular α may form with the same orientation as the allotriomorph α or as a different variant, where both have been found to form by separate mechanisms. The former is said to form due to instabilities at the α/β interface caused by the perturbation wavelength as reported by Mullins et al. [Mullins et al., 1963; Mullins et al., 1964]. In this case the boundary between the allotriomorph α and intergranular α develops due to a "pinch-off" mechanism. The latter intergranular α is proposed to nucleate sympathetically on the allotriomorph α, wherein an α crystal nucleates at the α/β boundary of another α crystal (allotriomorph α) that is different from the composition of the matrix [Aaronson et al., 1995]. Here the intergranular α would be of a different orientation than the allotriomorph α and they would be separated by a α/α boundary [Nag, 2008]. Duerig et al. have also found the sympathetic form of intergranular α to be present in Ti-10-2-3 after aging [Duerig et al., Metal. Trans. A, 1980]. Intragranular α is typically brought about by a separation of the β-phase. The products of the β-phase separation are temperature dependent, but always result in the formation of α. Menon and Aaronson [Menon et al. 1986] showed that at temperatures higher than the monotectoid isotherm in binary Ti-alloys α and β′ (solute lean) are in equilibrium, while at lower temperatures α and β are in equilibrium. They also reported that below certain aging temperatures in Ti-Cr alloys, a discrete change in aspect ratio of α precipitates occurred along with an increase in their growth kinetics and volume fraction. Furuhara et al. [Furuhara et al., 1998] expressed similar findings in Ti-Mo alloys with respect to the same monotectoid reaction. Not only can α form from β-phase separation, but also from ω-phase. Duerig et al. [Duerig et al., Metal. Trans. A, 1980] and Ohmori et al., [Ohmori et al., 1998] observed fine α plates that nucleated on ω in Ti alloy Ti-10-2-3.

1.3.2. β to ω

The transformation of β to ω is not a diffusional transformation like β to α, but rather a shuffle or displacive transformation. ω does not form randomly, but in specific orientations with respect to β. This OR was first described by Silcock [Silcock, 1958] as follows.

$$(0001)_\omega // (\bar{1}11)_\beta \text{ and } (11\bar{2}0)_\omega // (1\bar{1}0)_\beta$$

$$\langle 11\bar{2}0\rangle_\omega // \langle 1\bar{1}0\rangle_\beta$$

Because of the relation of the $(0001)_\omega$ plane to the $(1\bar{1}1)_\beta$ plane, it can be inferred that ω may form as four variants. This is due to the fact that there are four sets of $\langle 111\rangle_\beta$ directions, which may give rise to four variants of ω. De Fontaine et al. [De Fontaine et al., 1971] investigated the transformation of β to ω in Ti alloys and showed that four variants of ω exist with the aforementioned relation and can be distinguished in the $[113]_\beta$ zone axis selected area diffraction (SAD) pattern. Figure 1.5 shows the SAD pattern of the $[113]_\beta$ zone axis for a Ti-15 wt.% Mo alloy as found by De Fontaine et al. Superlattice reflections occur at the $1/3\{211\}_\beta$ and $2/3\{211\}_\beta$ positions, which are indicative of the ω2 and ω3 variants. The reflections caused by ω1 and ω4 variants lie on the $\{211\}_\beta$ spots and $\{110\}_\beta$ spots, respectively, making them more intense than normal. Identical results have been reported in multiple Ti alloys by other authors for the $[113]_\beta$ zone axis pattern [Harper, 2004; Qzai et al. 2005; Nag et al. 2009;].

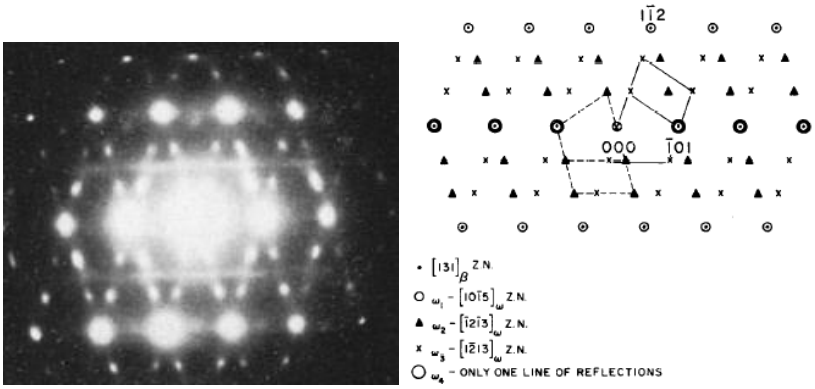

Figure 1.5. Selected area diffraction pattern of the $[131]_\beta$ *zone normal (Z.N.) (left) in Ti-15 wt.% Mo and accompanying schematic of the* $[131]_\beta$ *zone normal with indexed reflections [De Fontaine et al., 1971].*

Two models exist, which involve the shuffling of atoms and planes with respect to the $\{111\}_\beta$ planes and corresponding plane normals ($\langle 111\rangle_\beta$). The first model, known as the "Linear Fault Mechanism" as described by Sass [Sass, 1972], begins with the BCC β structure and a stacking sequence of the close packed $\{111\}_\beta$ planes of ABCABC. If equal and opposite shears are applied to the $\{110\}_\beta$ planes in the $\langle 111\rangle_\beta$ direction, two adjacent $\{111\}_\beta$ planes collapse to form ω. After the collapse is complete, a six-fold symmetry exists about the $\langle 111\rangle_\beta$ direction, along which the collapse occurred. However, it is possible for the planes to partially collapse, resulting in an incomplete ω transformation (athermal ω) with trigonal symmetry about the $\langle 111\rangle_\beta$ direction. Figure 1.6 shows a schematic taken from Bagariatskii et al. [Bagariatskii et al., 1959] depicting the direction in which atoms must move in the β-phase to form the ω-phase.

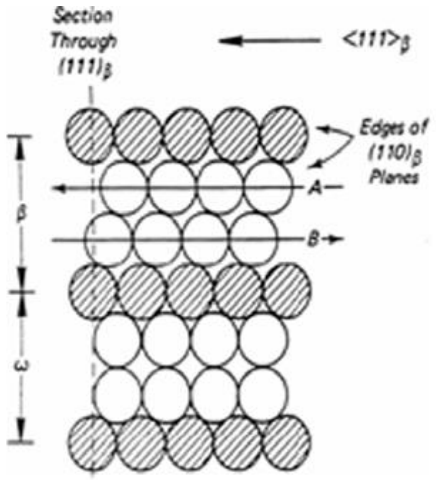

Figure 1.6. Schematic of the atoms which move during the collapse of the $\{111\}_\beta$ *planes in forming the ω-phase [Bagariatskii et al., 1959].*

While the Linear Fault Mechanism explains formation of ω, it does not explain the reversibility of ω with temperature. The "Phonon Mechanistic Model" proposed by De Fontaine et al. [De Fontaine et al., 1971], however, accounts for the temperature dependence as well as the composition dependence noted for various stages of ω transformation. Similar to the Linear Fault Mechanism model, the Phonon Mechanistic Model assumes a stacking sequence of ABCABC for

the $\{111\}_\beta$ planes along the $\langle 111\rangle_\beta$ directions. Instead of shear causing the atoms to move, a phonon propagating in the $\langle 111\rangle_\beta$ direction causes the atoms to shift. According to De Fontaine [De Fontaine, 1973] the phonon propagates as a transverse sinusoidal displacement wave with an amplitude of $1/3\,[211]_\beta$, which is equivalent to a longitudinal sinusoidal displacement wave with an amplitude of $2/3\,[111]_\beta$. The effects of a $2/3\,[111]_\beta$ longitudinal sinusoidal wave on the $\{111\}_\beta$ planes in a BCC lattice is shown in Figure 1.7. In three dimensions the stacking sequence changes from ABCABC to AB′AB′ as seen in Figure 1.8. Transformation using this model results in a continuum of incomplete ω transformations between β and the ideal ω, wherein structures with trigonal symmetry can exist in intermediate stages of transformations. This can subsequently be used to explain the reciprocal lattice streaking in SAD patterns, which accompanies the superlattice reflections associated with ω.

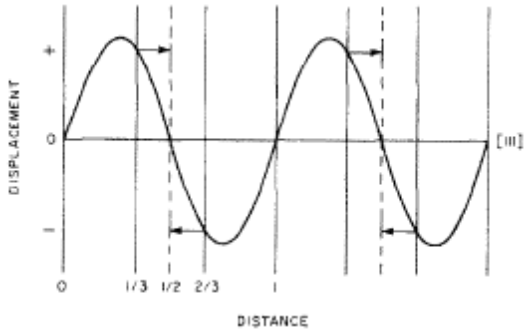

Figure 1.7. A longitudinal sinusoidal displacement wave showing its effect on the $\{111\}_\beta$ *planes during the propagation of the wave to transform β to ω [De Fontaine, 1973].*

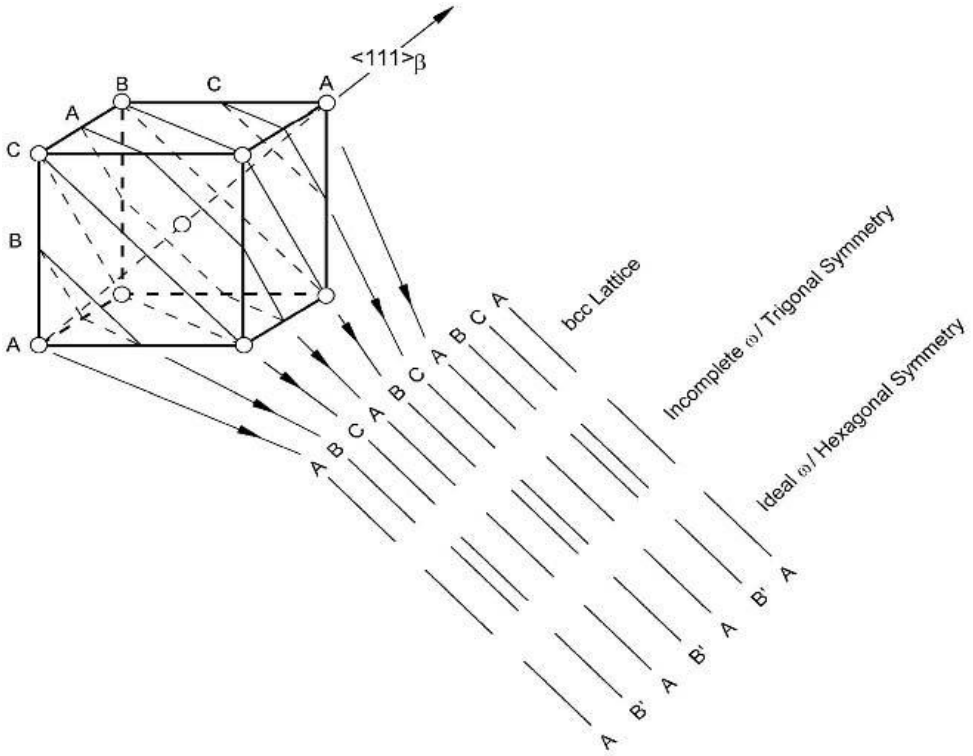

Figure 1.8. Representation of the $\{111\}_\beta$ *planes in a BCC crystal at different stages of transformation to ω [Lütjering and Williams, 2007].*

The results of the transformation can be seen when viewing the crystal from a reference along the $[110]_\beta$ zone axis. Sukedai et al. [Sukedai et al., 1991] and Devaraj et al. [Devaraj et al., 2012] have provided high resolution images of the final stages of transformation from β to athermal and isothermal ω. Figures 1.9 and 1.10 show HR TEM and HAADF-STEM images, respectively, from their works on Ti-Mo alloys. It is quite obvious in Devaraj et al.'s images, wherein the $\langle 111\rangle_\beta$ is parallel to the short side of the red rectangle, that the two atoms in the center of the red rectangle have been displaced towards the midline of the rectangle, along the $\langle 111\rangle_\beta$ direction.

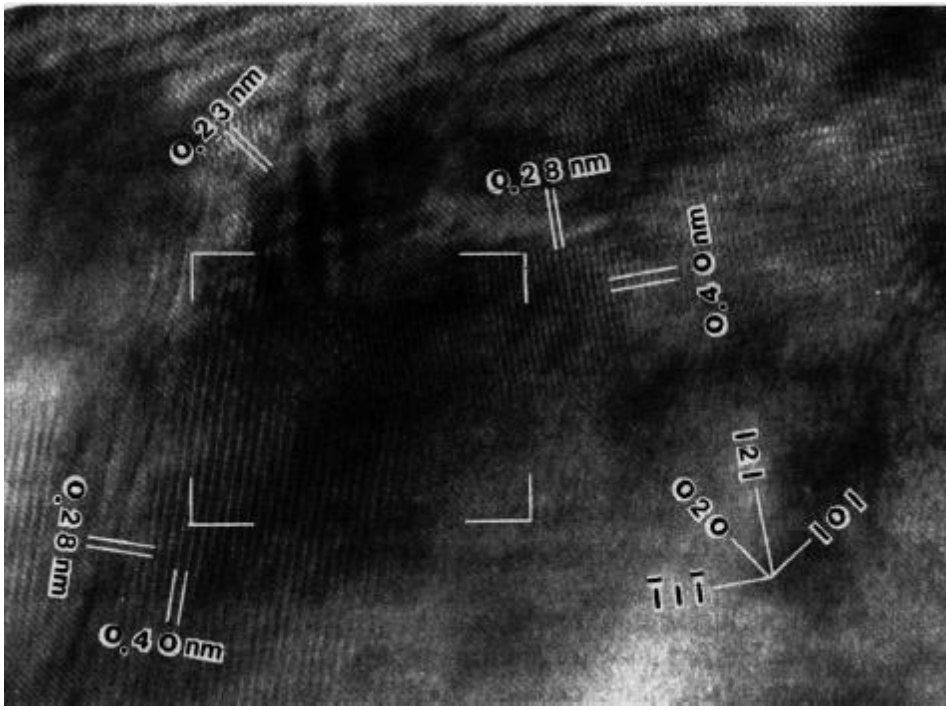

Figure 1.9. HRTEM image of Ti-20mass%Mo aged at 623K for 8 hours showing two ω variants [Sukedai et al., 1991].

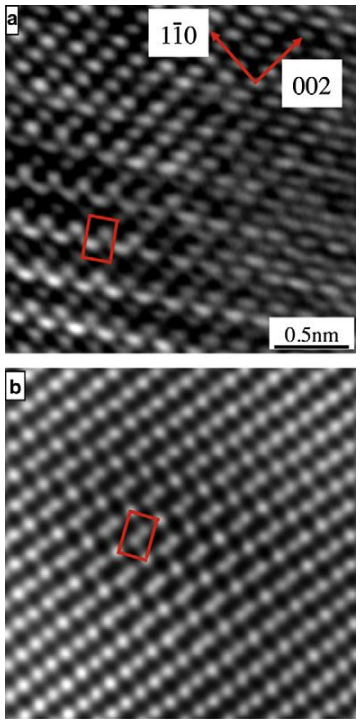

Figure 1.10. (a) HRTEM image of ω in Ti-9at.%Mo and (b) HAADF-STEM image of ω in the same sample [Devaraj et al. 2012].

In some alloys, the displacive shuffle reaction is accompanied by replacement ordering, from which "ordered ω" forms. Ordered ω has similar ORs with the parent phase as regular, disordered ω has with β [Nag, 2008]. It has been shown in Ti-Al-Nb alloys that an ordered B2 structure forms from the β-phase upon quenching, in which fine, coherent particles were found to exist [Strychor et al, 1988]. These particles were similar to disordered ω, but exhibited the ordering of the B2 matrix. Bendersky et al. [Bendersky et al., 1990] found that these particles were very similar to regular ω, but the lattice spacing in the $\langle 0001\rangle_\omega // \langle 111\rangle_\beta$ directions was doubled. While these types of "ordered" ω-phase exist, they only seem to be present in certain systems, where the B2 structure forms.

1.3.3. ω to α

The occurrence of fine, uniformly distributed α-phase in β-Ti alloys has been attributed to its nucleation in the presence of precursory ω-phase during low temperature aging. α has been shown to precipitate in the vicinity of ω sites, at the ω/β interface, and in the center of ω particles [Azimzadeh et al., 1998; Omhori et al., 1998; Williams et al., 1969; Prima et al, 2006]. Because α is known to form from the decomposition of ω, the formation of ω-phase may be thought of as an intermediate step in the transformation of β to α. During this intermediate step, precipitation of α has also been shown to be dependent upon the morphology of ω (cuboidal or ellipsoidal). As the lattice misfit varies from low to high, the location and mechanisms for α precipitation change. α precipitation in systems containing cuboidal ω (high lattice misfit) has been observed to take place at ledges or dislocations at the ω/ β interface [Ohmori, et al. 1998; Williams et al, 1969]. The strain energy associated with cuboidal ω may be reduced further by the formation of α at the ω/β interface, making cuboidal ω/β interfaces more stable as well as reducing their number. Prima et al. [Prima et al., 2006] showed that α nucleated from within the ω-phase. They proposed that because α nucleated within the center of ω, α coarsened at the expense of ω. In systems that contain ellipsoidal ω (low lattice misfit) the nucleation sites and mechanisms causing α

precipitation are not as evident. Azimzadeh et al. [Azimzadeh et al. 1998] showed that ellipsoidal ω served as precursors for α in specimens heat-treated up to 460°C. However, α did not precipitate at the ω/β interface or within a ω particle, but at "some distance" from the ω particles. They justified their observations by referencing Vassel's [Vassel, 1990] work, which reported that regions surrounding, but not adjacent to, ω were enriched in Al and promoted α formation.

Having evidence that the transformations from β to ω, β to α, and ω to α are related, Ohmori et al. [Ohmori et al., 1998] determined ORs for ω, α, and β. They were found to be:

$$(0001)_{\omega}//(\bar{1}2\bar{1}0)_{\alpha}//(\bar{1}11)_{\beta}$$

$$(\bar{1}\bar{1}20)_{\omega}//(0001)_{\alpha}//(0\bar{1}1)_{\beta}$$

$$(1\bar{1}00)_{\omega}//(10\bar{1}0)_{\alpha}//(211)_{\beta}$$

This group also acquired high resolution transmission electron microscopy images of α nucleation at ω/β interfaces in Ti-10-2-3.

Similar to what was reported by Azimzadeh et al. [Azimzadeh et al. 1998] and Vassel [Vassel, 1990], Nag et al. [Nag et al., Acta Mater., 2009] proposed that local enrichment of Al near ω was responsible for the nucleation of α. In their work on Ti-5553, they stated that since ω is coherent with β, the lattice misfit at the interface is low and may not be favorable sites for α nucleation. However, using 3D atom probe tomography, they were able to show that Al piled up at the ω/β interfaces near isothermally coarsening ω precipitates. This localized enrichment of Al coupled with depletion of Mo, V, and Cr, acted as nucleation sites for α.

1.4. Welding Titanium and Titanium Alloys

Most titanium components are joined by fusion welding techniques. Because titanium is a reactive metal, care must be taken while welding to avoid exposure to the atmosphere and limit contamination. Interstitial element (mainly oxygen, hydrogen, and nitrogen) ingression occurs in Ti and its alloys above 500°C and has been shown to cause severe embrittlement. Techniques

such as gas tungsten arc welding (GTAW), gas metal arc welding (GMAW), laser beam welding (LBW), and electron beam welding (EBW) are typical fusion welding processes suitable for joining Ti and Ti alloys. They employ methods with which to protect the titanium workpieces from the atmosphere. In the cases of GTAW, GMAW, and LBW, a shield of Ar gas must be formed around the top and bottom of the weld pool. This is done by constructing an enclosure around the workpiece and welding torch that confines the Ar around the weld pool. In the scenarios where an enclosure cannot be made around the workpieces, such as in-the-field repairs, a protective Ar gas shield on the top surface may suffice. EBW, on the other hand, is performed under high vacuum and is devoid of contamination from the atmosphere. Generally, if precautions are taken to properly clean the workpieces and provide a clean environment, each method can produce quality welds.

1.4.1. Problems Associated with Welding Titanium Alloys

In general, commercially pure titanium and α+β alloys, such as Ti-6Al-4V in the annealed condition are weldable without difficulties. Metastable β-titanium alloys, however, can be welded, but at the expense of their ductility. A few explanations have been proposed for the low ductility in welded metastable titanium alloys including phase transformation, formation of hard and brittle precipitates, and formation of hydrides in the weld zones. Alvarez et al. (2004) showed that hydrogen in excess of 3.5 at% in bulk metastable B–C Ti caused brittle fracture to occur in the aged condition. Danielson et al. (2003) found that oxygen embrittled commercially pure Ti by inducing a phase change from low temperature α cells and large β grains in a low oxygen specimen to an acicular microstructure with retained β phase between α cells, Widmanstätten plates, and α phase along grain boundaries. Similar results for hydrogen and oxygen embrittlement in titanium alloys have been discussed by Lynch et al. (1995) and Tal-Gutelmacher and Eliezer (2005). Both reported the formation of acicular microstructures of α and β phases as well as α plates at the grain boundaries in the presence of oxygen.

1.4.2. Electron Beam Welding

EBW is especially suited for welding titanium. While the other methods, GTAW, GMAW, and LBW, are typically less expensive, can be performed on site and out of position, EBW can consistently produce high quality welds because of the absence of oxygen, nitrogen, and hydrogen in the welding chamber. EBW also produces narrow weld zones that have been shown to penetrate up to 15cm in a single pass [Russell, 1981]. This greatly reduces the need for multipass welds, which are commonly required for joining thick sections. The weld zone, which includes the fusion zone (FZ) and heat affected zones (HAZ), is narrow compared to those made by other fusion welding methods due to the high energy density provided by the electron beam. Because the FZ and HAZs are narrow, residual stresses are reduced in the as-welded (AW) condition [Cottrell, 1985]. EBW has been used to weld Ti and Ti alloys in the aerospace industry since the 1970s. Most notably it is used to join pylon posts and wing components for the F15 as well as the wing boxes that hold the variable geometry wings in the Tornado and F14 [Mendez et al., 2001].

There are drawbacks to EBW, however. The most obvious is that welding with an electron beam (EB) requires a vacuum. This limits part size, production rates, and energy consumption. Part size is limited to the size of the vacuum chamber, production rates are limited by part size and the time it takes to reach the required vacuum level for a given chamber size, and energy consumption increases with chamber size and part size. Newer EBW systems can have chambers large enough for parts measuring 4 m x 2 m x 1.8 m and more efficient vacuum systems are being designed to decrease the time it takes to pump down a chamber as well as reduce energy demands [Sciaky, 2014]. Another problem associated with EBW is that the process is not portable like GTAW and GMAW processes. Therefore, on-site welding is not possible and field repairs using EBW are not likely. However, there is an interesting exception. The Energia rocket, manufactured by the Russians required massive fuel tanks. These fuel tanks

were assembled on-site and EB welded together. The Russians created local vacuum chambers using ferroelectric fluids to seal them. The local vacuum chambers could be moved, which made welding large sections on-site possible [Mendez et al., 2001].

1.5. Ti-5Al-5V-5Mo-3Cr-0.4Fe (Ti-5553) Alloy

1.5.1. History and Applications of Ti-5553

Ti-5Al-5V-5Mo-3Cr (Ti-5553) is a modified version of the Russian alloy, VT22 (Ti-5Al-5V-5Mo-1Cr-1Fe), which has been extensively evaluated by Orlova et al. [Orlova et al., 1986], Ivasishin et al. [Ivasishin et al., 2003], Moiseev et al. [Moiseev et al., 1990], Shevel'kov [Shevel'kov, 1992], and Gridnev et al. [Gridnev et al., 1986]. TIMET proposed the concept of Ti-5553 in 1997 as a high strength metastable beta alloy, suitable for large section forgings in aerospace applications [Fanning, 2005]. Similar to VT22, Ti-5553 has excellent through-hardening properties due to its sluggish alpha transformation compared to Ti-10-2-3, another metastable beta alloy with comparable mechanical properties and deformation characteristics [Lütjering and Williams, 2007]. Because Ti-10-2-3 is prone to Fe segregation, sensitive to high temperature forging and heat treatments, and is not air-hardenable, Ti-5553 was developed to address these issues [Fanning, 2011].

According to Fanning [Fanning, 2005], Ti-5553 has an average β-transus of 856°C and is typically solution treated at temperatures 28°C to 56°C below the β-transus, while aging is carried out in the temperature range from 560°C to 677°C. It should be noted that traditional solution treatments for most materials are performed in a single phase region of an equilibrium phase diagram and aging treatments are performed at subsequently lower temperatures, within a two-phase region of an equilibrium phase diagram. Ti-5553 exhibits exceptional forging characteristics and has good deep hardenability and is therefore used extensively in Boeing 777s and 787s and Airbus A380s for frame, fastener, and undercarriage applications [Kearns, 2005] as well as landing gear components [Fanning, 2005]. Ti-5553 has turned into the baseline Ti alloy

for high strength applications, from which other alloys, such as Ti18 [Ti-5.5Al-5V-5Mo-2.3Cr-0.8Fe-0.14O) are being developed [Fanning, 2011].

1.5.2. Microstructures and Mechanical Properties

Like many metastable β and near β alloys, microstructures and mechanical properties in Ti-5553 are sensitive to heat treatment temperatures and times. This is because precipitation events occur, during which two or more precipitates may coexist. However, depending on the time and temperature, the presence of one precipitate is typically favored over that of another. Ti-5553 attains its strength from the precipitation of α. Fanning reported yield strengths and ultimate tensile strengths that ranged from 1100 MPa to 1303 MPa and 1163 MPa to 1386 MPa, respectively, for cast and wrought Ti-5553 in different solution treated and aged conditions. Harper [Harper, 2004] showed similar results in Ti-5553, in which solution treated and quenched samples exhibited yield and tensile strengths of 725 MPa and 788 MPa, respectively, where solution treating then aging produced specimens with yield and tensile strengths upward of 1200 MPa.

Harper [Harper, 2004], Nag [Nag, 2008], Welk [Welk, 2010], and Folz et al. [Folz et al., 2011], Clement et al. [Clement et al., 2007] and Kar [Kar et al., 2013] have all performed work that shows the effects of solutionizing (above the beta-transus) and aging within the α/β phase regime on microstructure and mechanical properties of Ti-5553. Findings from the above work that have been widely accepted are: (i) 100% β is retained upon cooling from above the β-transus, (ii) solution treating at higher temperatures and/or for longer times increases the β grain size, (iii) α precipitate size is proportional to aging temperature and time, (iv) athermal ω forms during cooling from the solutionizing temperature, (v) athermal ω transforms to isothermal ω during aging and disappears above temperatures that promote α precipitation, (vi) grain boundary α formation is unavoidable during aging and is strongly promoted at higher aging temperatures, and

(vii) mechanical properties are improved with the formation of fine, uniformly dispersed α precipitates.

The presence of ω in Ti-5553 has been reported by Harper [Harper, 2004], Clement et al. [Clement et al., 2007], and Nag et al. [Nag et al., Acta Metal., 2009]. Figure 1.11 shows selected area diffraction patterns of the $[110]_\beta$ and $[113]_\beta$ zone axes, in which superlattice reflections from ω exist, as well as a DF image of ω precipitates. ω's presence in Ti-5553 is important, because it has significant effects on mechanical properties and the precipitation of α during aging treatments. Nag et al. [Nag et al, Acta Mater, 2009] and Nag et al [Nag et al., 2012] have shown that ω is a necessary precursor for the homogeneous precipitation of α in Ti-5553, upon which mechanical properties strongly depend.

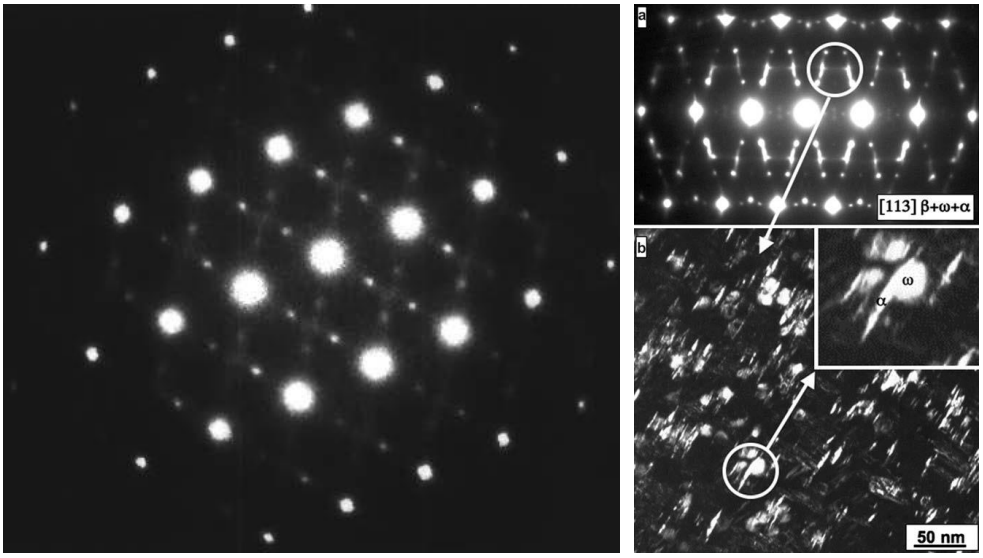

Figure 1.11. (left) A $[110]_\beta$ zone axis pattern with ω superlattice reflections at 1/2 and 1/3 the $\{211\}_\beta$ reflections [Harper, 2004] and (right) a $[113]_\beta$ zone axis pattern with an accompanying dark field image showing α which has nucleated on a ω particle [Nag et al., Acta Mater., 2009].

1.5.3. Welding of Ti-5553

Limited work has been performed on fusion welding Ti-5553. This is partially due to the fact that Ti-5553 was developed as a forging alloy, wherein welding may not ever be needed. In the little work that has been conducted on welding Ti-5553 it is generally accepted that Ti-5553 is weldable at the cost of hardness within the fusion zone (FZ) and ductile macroscopic tensile

behavior. Mueller et al. [Mueller et al., 2008] and Shariff et al. [Shariff et al., 2012] showed that the hardness within the FZ and heat affected zones (HAZs) of laser welded Ti-5553 decreased below that of the base metal (BM) in the AW condition. A large difference between their works, however, is that Shariff et al. used Ti-6Al-4V filler wire and Mueller et al. used no filler wire. This resulted in Shariff et al. finding martensitic structures within some regions of the FZ of the AW specimens whose joint gaps were large enough to impede complete mixing of the filler wire and base metal. In another study on welding Ti-5553, Mitchell et al. [Mitchell et al., 2011] used EB welding to autogeneously join Ti-5553 sheets. Similar to the results reported by Mueller et al. [Mueller et al., 2008] and Shariff et al. [Shariff et al., 2012], Mitchell et al. found that the hardness within the HAZs and FZ decreased below that of the BM. This was attributed to the 100% retained β microstructure in the FZ and HAZs, which is known to be softer than α hardened β. They also found that during tensile testing, fracture occurred in a brittle manner within the FZ at stresses much lower than the yield strength and ultimate tensile strength for un-welded Ti-5553. However, at higher magnifications it was noticed that dimples resided on the fracture surface, which suggested microscopic ductile behavior. In terms of microstructure, it was generally found that a cellular dendritic microstructure formed within the retained β in the FZ and equiaxed β grains developed within the HAZs. In all cases the FZ and HAZs were observed to be quite narrow; approximately 5.7 mm combined for the widest and 2 mm combined for the narrowest. These results, while limited, provide a basis as to the weldability of Ti-5553.

1.6. Motivation

There is a lack of research performed on the welding of Ti-5553, particularly electron beam welding. Not only is there little research on electron beam welded Ti-5553, but also even fewer works on post weld heat treatments for Ti-5553. Because Ti-5553 is considered a baseline Ti-alloy upon which future alloys will be based, understanding the effects of welding on its structure and properties is imperative for continued use of Ti-5553 and the further development of

metastable β-Ti alloys. The current work addresses this gap in the literature by presenting mechanical properties, localized strain distribution in the vicinity of the weld, microstructural responses, solidification of the fusion zone, and fracture mechanisms found as a result of electron beam welding and post weld heat treatments on Ti-5553.

In addition to the practical aspects of welding Ti-5553, ω-phase as a result of electron beam welding has been investigated. The ω-phase has been observed to exist in near-beta and metastable beta Ti alloys. Its presence has been linked to embrittlement and the precipitation of alpha during aging treatments. Many researchers have recorded the presence of ω in metastable beta Ti alloys using X-ray diffraction experiments, selected area diffraction patterns, dark field transmission electron microscopy, high resolution transmission electron microscopy, and more recently high angle annular dark field scanning transmission electron microscopy. These efforts, however, have been limited to model binary Ti systems, such as Ti-V, Ti-Mo, and Ti-Cr, and in rare cases to more practical systems like Ti-10-2-3. The current knowledge of the ω-phase is somewhat limited to model binary systems and does not address its presence in alloys containing more than one alloying element. This work, while mainly focused on the evolution of properties and microstructure in response to electron beam welding, also sheds light on the presence of ω-phase in the commercial Ti alloy, Ti-5553, subjected to processing (i.e. electron beam welding). Using high angle annular dark field scanning transmission electron microscopy to observe the ω-phase in electron beam welded Ti-5553 in the as-welded condition, this work discusses the presence of ω as well as its ordering and coherency compared to the beta matrix and its effects on embrittlement in electron beam welded Ti-5553. Such efforts have not yet been reported are valuable for completely understanding the ω-phase and Ti-5553.

2. Experimental Procedure

2.1. Material

The material under investigation is the metastable β-Ti alloy, Ti-5Al-5V-5Mo-3C5-0.4Fe (Ti-5553). The nominal composition of Ti-5553 is given in Table 2.1. Plates of Ti-5553 were received in the through-transus processing condition, which consists of β grains containing α platelets with globular α at the β grain boundaries. Evidence of rolling was also observed in the as-received plate as indicated by the elongation and directionality of β grains. The plate was sectioned into 1.6mm thick sheets using wire-electrical discharge machining prior to electron beam welding (EBW).

Table 2.1. Nominal composition of Ti-5553 (values are in wt.%).

Material	O	N	Al	V	Mo	Cr	Fe	Ti
Ti-5Al-5V-5Mo-3Cr (Ti-5553)	0.14	<0.01	5.03	5.1	5.06	2.64	0.38	Bal.

2.2. Electron Beam Welding

EBW was performed at Auckland University of Technology, Auckland, NZ. Autogeneous butt-welds were made with a voltage of 150kV, a current of 3mA, and travel speed of 8.5mm/s. These parameters were determined by Mitchell et al. [Mitchell et al., 2011] to produce consistent, keyhole welds in Ti-5553. All welds were made in the down-hand position and perpendicular to the rolling direction. Prior to welding, the sheets were prepared by thoroughly cleaning in degreasing solutions, then rinsing under water, and drying with ethyl alcohol under a heated air dryer. Specimens for metallurgical examination, and tensile testing were sectioned from the welded sheets.

2.3. Post Weld Heat Treatments

After EBW, specimens either remained in the as-welded condition or were heat treated using one of the following three heat treatment schedules shown in Table 2.2. Each specimen was degreased and rinsed with ethyl alcohol before heat treatment to remove any oils or dirt that could cause contamination. The heat treatments were conducted in sealed Lindberg/Blue M™

tube furnaces, in which a vacuum was initially created to produce a contaminant-free atmosphere. Furnaces were backfilled with Ar gas for the duration of each heat treatment. At the end of each heat treatment, the specimens were removed from the furnace and allowed to cool in air to room temperature. In total, four conditions of specimen were available for investigation; as-welded, heat treated at 700°C/4h, heat treated at 804°C/1h, and heat treated and aged at 804°C/1h+600°C/4h.

Table 2.2. Post weld heat treatment temperatures and times used for subsequent precipitation strengthening after electron beam welding.

Temperature (°C)	Time (hours)	Cooling Method
700*	4	Air
804*	1	Air
804/600**	1/4	Air

*Single step heat treatments consisting of sub-β transus precipitation treatments followed by air cooling to room temperature

**Two step heat treatment consisting of a sub-β transus precipitation treatment (804°C) followed by air cooling to room temperature then heating to an aging temperature (600°C) followed by air cooling to room temperature

2.4. Metallographic Specimen Preparation

Specimens for light optical, scanning electron, and electron microprobe analysis were metallographically prepared. Cross sections of the EBW specimens were made with the viewing direction parallel to the length of the weld, perpendicular to the thickness of the sheet. The specimens were mounted in Bakelite and ground and polished from 320 grit SiC paper to 0.05μm colloidal SiO_2. The specimens for light optical analysis were etched with Kroll's (1-3mL HF, 3-6mL HNO_3, 100mL water) to reveal microstructure. Contrary to submersion or swab etching techniques, these specimens were sprayed with Kroll's using a small squirt bottle. It was found that this method produced exceptional results and allowed for more control over the etching process. Specimens for scanning electron microscopy (SEM), electron probe microanalysis (EPMA), and focused ion beam (FIB) milling, were left in the as-polished condition to retain any chemical information and avoid the attack of phases caused by etching.

2.5. Electron Probe Microanalysis

A JEOL JXA-8900 SuperProbe Electron Probe Microanalyzer with Advanced MicroBeam software was used to obtain elemental concentration information from the EBW specimens. A repeatable method routine was created to perform wavelength dispersive spectroscopy in order to determine the concentration (in wt.%) of the each of the elements in Ti-5553, i.e. Ti, Al, V, Mo, Cr, and Fe. An accelerating voltage of 15kV with a probe current of 40nA was used in all cases. On-peak and off-peak dwell times were 20 seconds and 10 seconds, respectively.

Samples for EPMA were prepared as described in section 2.4; however these samples were not etched in order to retain all chemical information. Linear traverse concentration profiles were made from BM to BM across the HAZs and FZ of the AW specimens to identify changes in composition due to EBW. These profiles were made at a depth of approximately 0.5 mm from the top surface of the specimens and performed with a step size of 60 μm between acquisition points for a total distance of 3000 μm. Profiles were also obtained across parallel dendritic cells within single grains in the FZ of each specimen (AW and PWHT). The profiles across parallel cells and intercellular regions were acquired using a step-size of 1μm was used between acquisition points. These acquisition settings provided sufficient counts and resolution to observe small fluctuations in concentration as well as detect the small amounts of Fe in each specimen.

2.6. Mechanical Properties Testing

2.6.1. Microhardness Profiles

Linear microhardness profiles were made from BM to BM across the HAZs and FZ of the AW and each of the three PWHT specimens. A Leco M-400FT microhardness tester was used with a Vickers indenter, a load of 300g, and a dwell time of 15 seconds. The profiles were made at a depth of approximately 0.5mm from the top surface of the specimens. The linear hardness profiles were then plotted to show the hardness trends across the WZ of each specimen.

2.6.2. Uniaxial Tensile Testing

Using an Instron 5550R load frame with a 100kN load cell and Bluehill data acquisition software, uniaxial tensile tests were conducted on subsize dogbone (ASTM E8) tensile specimens. The tensile specimens were made from the 1.6mm thick Ti-5553 sheets, which were previously electron beam welded and in the AW or PWHT conditions. The welds were located in the center of the gage length and perpendicular to the tensile direction. The tensile tests were conducted with a crosshead speed of 3mm/s. Five to seven specimens were tested for each condition.

2.6.3. Localized Strain Measurement

2.6.3.1. ARAMIS and Digital Image Correlation

ARAMIS, a 3D digital image correlation (DIC) photogrammetry system, was employed parallel to tensile testing. ARAMIS is comprised of two high-speed digital cameras and a computer with collection and analysis software designed and manufactured by GOM mbH. The system is a non-contact, material independent system, which provides local sensitivity to static or dynamic loads. It has been shown by Grytten et al. [Grytten et al., 2009], Siebert et al. [Siebert et al., 2007], and Tiwari et al. [Tiwari et al., 2007] that the use of 3D DIC photogrammetry systems provides valid stress and strain measurements over a variety of materials and tests when compared to measurements made with traditional strain gages and load cells.

DIC uses a combination of photgrammetry, digital image processing, and stereo imaging to track features on a specimen's surface and correlate their positions to a predetermined coordinate system. A specimens' surface area can range in size from mm^2 to m^2 and have complex geometries as long as the specimen remains within the calibrated analysis volume. Measurements are made by comparison of an image series that is captured over timescales from microseconds to years. The system uses the first image taken by DIC as a reference or "zeroed" condition where the specimen is undeformed and then compares all subsequent images to it. By tracking features on the specimen's surface and comparing their positions to the reference

position, localized displacement can be determined. Not only can displacement be measured in plane (x-y plane), but also out of plane (z-direction towards the cameras) by triangulation between the two cameras. However, the specimen must be within the calibrated analysis volume to accurately measure in plane (x-y) and out of plane (z) displacements. After an image series is collected post-process analysis within the software provides information on shape, position, displacement, and true strain during and after testing.

In order for ARAMIS to track features on the surface of a specimen, a high contrast pattern must be applied. Depending on the size of the test specimen, different patterns maybe used to best track the displacement of the specimen. A typical pattern consists of periodic or randomized spots over a light background and is shown in Figure 2.1. Patterns made up of a white background and black spots provide excellent contrast and can easily be detected by the software. The pattern should be applied in such a way and with appropriate textiles so that it can deform with the specimen while still completely covering the surface without severe distortion or breakaway. Stenciling, spray paint, markers, as well as permanent markings are suitable ways by which to make a pattern. If the pattern is unable to deform with the specimen or is somehow dissociated from the surface of the specimen, ARAMIS will not be able to track the pattern or give measurements that are representative of the deformation experienced by the specimen.

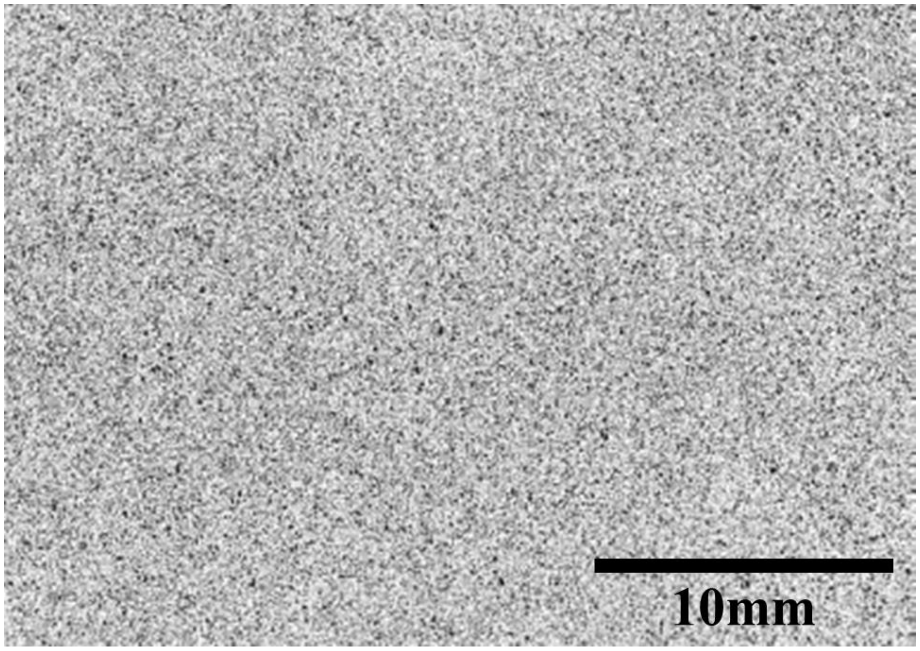

Figure 2.1. An example of a high contrast stochrastic pattern that can easily be recognized by ARAMIS [GOM mbH, Software].

2.6.3.2. ARAMIS – Setup and Testing

ARAMIS was used to capture the localized strain distribution in the vicinity of the WZ during uniaxial tensile testing of sub-size tensile specimens (ASTM E8). For these specimens, the weld was located in the center of the gage length, perpendicular to the long axis of the specimens. High contrast patterns were applied to the faces of each specimen using spray paint. A light coat of flat white spray paint was first applied to sufficiently coat the entire gage length, but still remain pliable in order to accurately capture the deformation experienced by the tensile specimens. Flat black spray paint was then used to apply a speckled pattern on top of the white background. One to two quick, glancing, horizontal passes approximately 45 cm away from the surface of the gage length were made to create a random speckled pattern. This method produced relatively low glare, high contrast patterns with spots approximately 0.2 mm – 1 mm in size. An example of a patterned tensile specimen is shown in Figure 2.2.

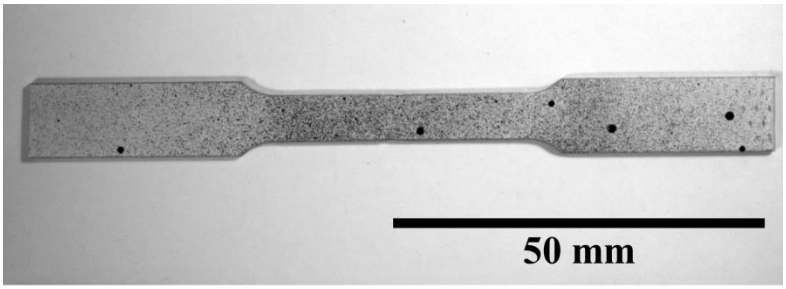

Figure 2.2, An example of a sub-size tensile specimen with high contrast speckle pattern applied by spray painting.

An ARAMIS HS system equipped with 50mm lenses was set up with respect to the tensile frame and specimen according to the analysis volume being utilized and instructions provided by GOM mbH. Figure 2.3 shows a schematic of the general configuration of the cameras with respect to the measuring volume. Because the gage length and width of the sub-size tensile specimens are small (25 mm x 6 mm), the smallest calibration panel (15mmx12mm) must be used to accurately capture the deformation within the region of interest in each specimen. Examples of typical calibration panels are shown in Figure 2.4. To ensure that the cameras remained clear of the tensile frame, a measuring distance of 180mm was used, which was the farthest distance from the center of the measuring volume that the cameras could be located before the smallest calibration panel was no longer relevant. A measuring distance of 180mm fixed the testing geometry to that recommended by GOM (Table 2.3).

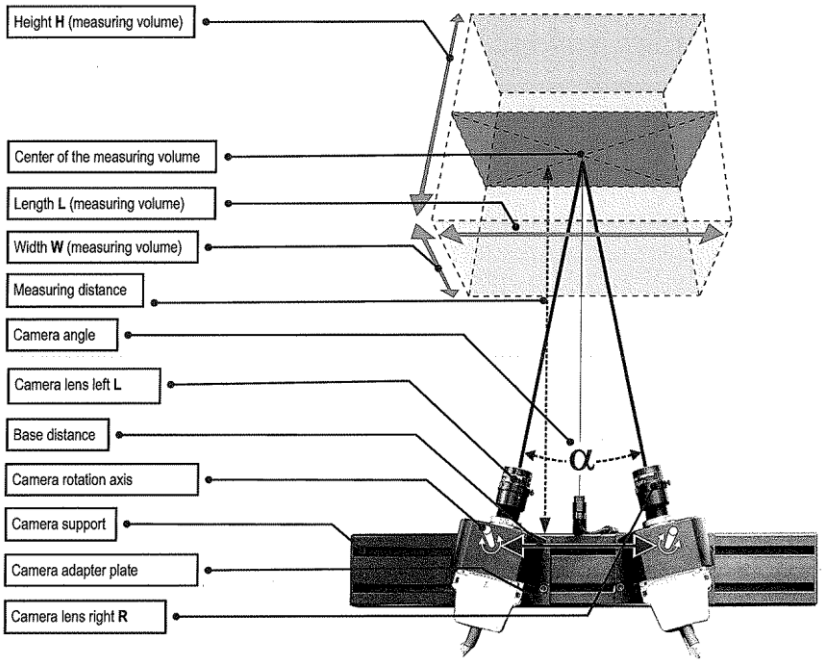

Figure 2.3. A representative diagram of the geometry between the measuring volume and cameras for typical testing using an ARAMIS system [GOM mbH, Hardware, 2007].

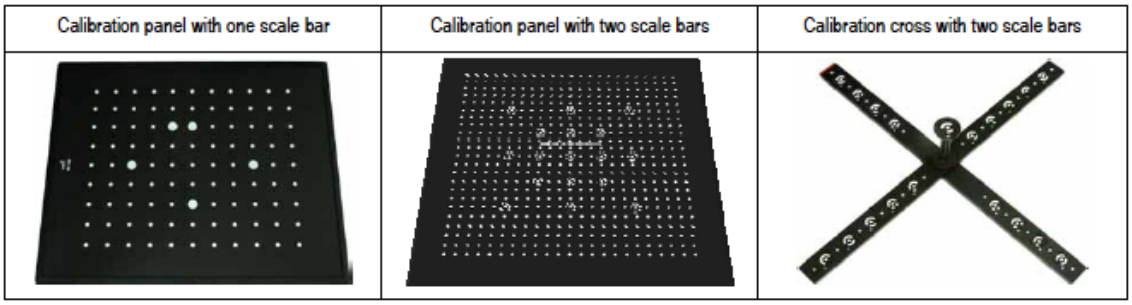

Figure 2.4. Example panels for calibrating ARAMIS and determining a measuring volume [GOM mbH, Software, 2007].

Table 2.3. Setup geometry distances and angles for use with the ARAMIS HS system equipped with a 50mm lens and using the smallest calibration panel (15mmx12mm). Refer to Figure 2.3.

	Measuring Distance (mm)	Base Distance (mm)	Camera angle, α (°)
Recommended	180	100	28
Actual	180	100	28

After the cameras were setup in the correct geometry, the system was calibrated according to the user manual and prompts during calibration within the software. Calibration is a sequential, thirteen step process that involves positioning the calibration panel in specific orientations with respect to the cameras and capturing an image series for calibration. Once the calibration steps are complete, the system calculates a measuring volume, whose length and width

must lie between 13mmx11mm and 20mmx16mm. If the calculated measuring volume is not within the specified range, recalibration will be required. The measuring volume for this investigation was 20 mm x 15 mm x 5 mm (L x W x H in Figure 2.3).

Figure 2.5 shows the setup of the tensile frame and ARAMIS after testing a specimen. This configuration was used for each specimen and routinely checked in order to maintain the correct specimen-to-camera geometry. If the setup was found to be out of the specifications for the desired measuring volume (due to slightly bumping the cameras or the position of the specimen in the grips), the setup was moved back to specifications and recalibrated.

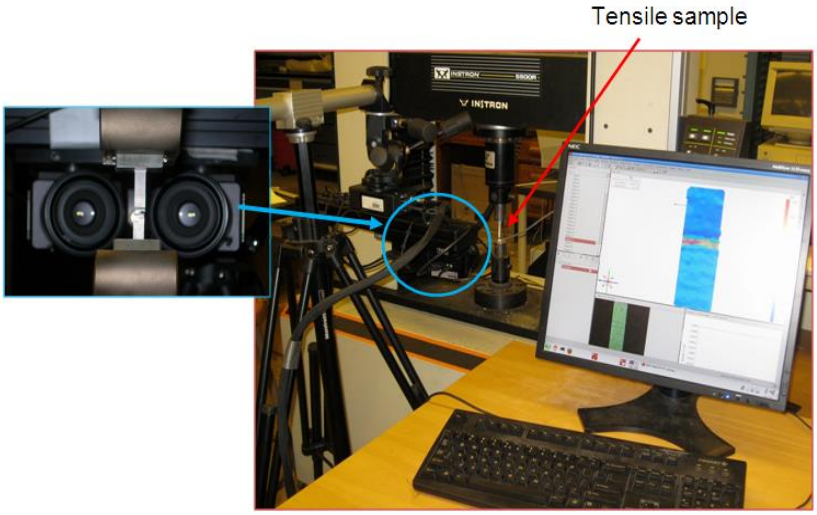

Figure 2.5. Set up of the tensile frame with ARAMIS after testing a specimen.

2.7. Fracture Analysis

2.7.1. Scanning Electron Microscopy

Fracured EBW Ti-5553 specimens in the AW and PWHT conditions were carefully sectioned using a Buehler Isomet 2 low speed saw so that very little contamination and disturbance of the fracture surface occurred. The specimens were sectioned perpendicular to the tensile direction, approximately 1 cm-1.5 cm behind the fracture location. These specimens were then mounted to 12.5 mm SEM stubs with carbon tape. A Hitachi 4300 SE/N was used to image each fracture surface at relatively low magnification as well as high magnification to observe features and provide evidence for how fracture occurred.

2.7.2. Metallographic Analysis

Using the complementary fracture surfaces to those in section 2.7.1, metallographic specimens were made by sectioning the broken tensile specimens approximately 1cm-1.5cm behind the fracture location. The cuts were made with a Buehler Isomet 2. The sectioned fracture surfaces were then mounted in Bakelite, oriented perpendicular to the thickness of the tensile specimens. The same procedure used in section 2.4 was used to prepare these specimens for light optical observation.

2.8. Transmission Electron Microscopy

2.8.1. Specimen Preparation

Due to the limited availability of material for this investigation of EBW Ti-5553 and the narrow WZs (~2.5 mm wide, including both HAZs and FZ) associated with EBW, specimens for transmission electron microscopy (TEM) cannot be made by bulk specimen preparation methods. Therefore, traditional methods, such as twinjet electropolishing, and dimpling followed by ion milling, will not suffice to accurately make individual specimens from the FZ, HAZ, or BM. Focused ion beam (FIB) techniques; however, allow for the precise removal of specimens from those small regions of interest in a bulk sample.

In order to begin making thin specimen for TEM observation and analysis, metallographic samples were prepared in the manner described in section 2.4, but were not etched so that all phases were retained. Vickers hardness indents were used to mark regions of interest within each sample so that locating the regions in the FIB instrument would be possible. The metallographic samples were then coated with Ir for 30 seconds. This coating of Ir served as protection against unwanted ion damage to the sample's surface.

A FEI Strata DB 235 FIB instrument was used to mill and extract thin specimens for observation and analysis in TEM. It was operated with an electron accelerating voltage of 5 kV and an ion accelerating voltage of 30 kV. The ion beam has a variable beam current from 5 pA to 10000 pA and is used to bombard a region of interest with Ga ions and effectively "mill" away

material. After a metallographic sample is inserted into the FIB instrument, a protective strip of Pt (approximately 2 μm x 2 μm x 25 μm) is deposited over the region of interest. Two trenches (10 μm x 15 μm x 25 μm) are milled on either side of the Pt layer to create the parallel surfaces of the rough TEM specimen. The surfaces are then cleaned by sequentially milling each face with lower ion beam currents so that ion beam damage and material redeoposition are removed. Once the cleaning is completed, the rough specimen is attached to a "plucker" needle using Pt deposition and cut free from the bulk with the ion beam. The bulk sample is then lowered away from the plucked specimen and the plucker needle is retracted along with the rough TEM specimen for protection during the sample exchange procedure. The bulk sample is removed from the FIB instrument and a Cu grid is then inserted into the FIB instrument's chamber. After the vacuum reaches an acceptable level, the beams are turned on and the plucker and rough TEM specimen are reinserted. The rough specimen is then attached to the center post of the Cu grid with Pt deposition in preparation for final thinning. Fine milling steps along with tilting the specimen and 180° scan rotations are used to successively reduce the thickness of the specimen until it becomes electron transparent. Once the specimen becomes electron transparent, it is ready for observation and analysis in the TEM.

2.8.2. Transmission Electron Microscopy

All TEM specimens were observed and analyzed using a JEOL JEM-2000FX at an accelerating voltage of 200kV. In order to correctly identify and confirm the presence of α and ω phases, the specimens were tilted to the $[001]_\beta$ zone axis and $[113]_\beta$ zone axis for α and ω, respectively. The $[001]_\beta$ zone axis has been shown to contain superlattice reflections for α due to the orientation relationship where $(10\bar{1}1)_\alpha // (100)_\beta$ [Rhodes et al., 1975; Lütjering and Williams, 2007]. The $[113]_\beta$ zone axis in β-Ti alloys has been shown to contain superlattice reflections corresponding to ω [De Fontaine et al., 1971; Harper, 2004; Nag, 2008, Nag et al., 2009]. The reflections for the α-phase in the $[001]_\beta$ zone axis pattern are located half way

between two of the $(002)_\beta$ reflections. The reflections for ω phase in the $[113]_\beta$ zone axis pattern are located at one third and two thirds of the distances from the central spot to the $(211)_\beta$ reflections (i.e. $1/3(211)_\beta$ and $2/3(211)_\beta$). Convergent beam (CBED) and selected area (SADP) diffraction patterns were acquired for each specimen oriented with the $[001]_\beta$ and $[113]_\beta$ zone axes parallel to the beam direction. Bright and dark field images were then acquired for the α and ω precipitates using their respective reflections in each zone axis pattern. Each diffraction pattern was indexed after the camera length was calibrated.

The camera length was calibrated to ensure that correct determination of the planar spacing (d) was accurate. A gold standard was used and ring diffraction patterns were acquired for each camera length.

The diffraction patterns were manually indexed by first measuring the angles and distances (R) between the closest and next closest spots from the central spot of the diffraction pattern. Using the calibrated camera length (L) and camera constant (λL) along with measurements, the d-spacings were calculated with the relation Rd= λL. The calculated d-spacings were compared to known values for BCC Ti. The planes corresponding with the d-spacings for BCC Ti were recorded and the angles between the plane normals were compared to the angles between the closest spot and the next closest spot. The following relation was used to determine the angles between the plane normals:

$$\cos(\phi) = \frac{\mathbf{g}_{h_1k_1l_1} \bullet \mathbf{g}_{h_2k_2l_2}}{\left|\mathbf{g}_{h_1k_1l_1}\right| \bullet \left|\mathbf{g}_{h_2k_2l_2}\right|} = \frac{h_1h_2 + k_1k_2 + l_1l_2}{\sqrt{h_1^2 + k_1^2 + l_1^2} \cdot \sqrt{h_2^2 + k_2^2 + l_2^2}} \qquad \text{Eq. 2.1}$$

The angles were checked for all possible combinations of order and positive and negative values of h, k, and l. The combinations of planes, whose plane normals met at angles that matched the measured angles between the corresponding spots, were designated as the indexed plane reflections. The zone axis of the diffraction pattern was confirmed by taking the cross product of

two of the reflections, $\boldsymbol{g}_{h_1k_1l_1}$ and $\boldsymbol{g}_{h_2k_2l_2}$, which are separated by an angle, Φ, that matches the measured angle between the corresponding spots in the diffraction pattern.

2.8.3. Atomic Resolution Microscopy

A JEOL JEM-ARM200CF aberration corrected transmission electron microscope was used to provide atomic resolution images of ω precipitates within the FZ of specimens in the AW condition. It was operated at 200kV and specimens were oriented with the $[110]_\beta$ zone axis parallel to the beam direction. This enabled the orientation relationship expressed by Silcock et al. [Silcock et al., 1956] $(0001)_\omega // (\bar{1}11)_\beta$ and $(11\bar{2}0)_\omega // (1\bar{1}0)_\beta$, to be exploited and ω to be resolved. High angle annular dark field (HAADF) scanning transmission electron microscopy (STEM) images were acquired of the precipitates and surrounding β-Ti matrix. Those images were analyzed using fast Fourier transforms (FFT) and inverse FTTs (IFFT) to observe the lattices of the β-Ti and ω precipitates more clearly. The collection angle for HAADF-STEM imaging was between 90-370 mrad.

3. Results and Discussion

3.1. Mechanical Testing

Uniaxial tensile testing in conjunction with the 3D DIC photogrammetry system, ARAMIS, was performed on tensile specimens containing an autogenous EB weld perpendicular to the tensile direction. These results do not reflect the properties of Ti-5553 alone, but a combination of properties from the weld and BM. All specimens were observed to fracture within the WZ. Representative tensile curves for selected specimens from each condition (AW, 700°C/4 hours, 800°C/1 hour, and 800°C/1 hour + 600°C/4 hours) are shown in Figures 3.1 through 3.4. It can clearly be seen that the specimens, except those heat-treated at 700°C/4 hours, exhibited no ductility. The specimens heat-treated at 700°C/4 hours plastically deformed, evidenced by the distinct yield point in the tensile curve of Figure 3.2 and the continually increasing stress until failure after yielding. It should be noted, however, that no visible necking

or plastic deformation was observed during testing of these specimens. Similarly, the AW condition and the two remaining PWHT conditions, 800°C/1 hour and 800°C/1 hour + 600°/4 hours, experienced no visible deformation. The average true plastic strain exhibited by the specimens heat-treated at 700°C/4 hours was 7.1%. Because the specimens heat-treated at 700°C/4 hours were the only ones that experienced plastic deformation, only an average yield strength could be determined for these specimens. It was found to be 864 MPa by using the 0.02% strain offset method.

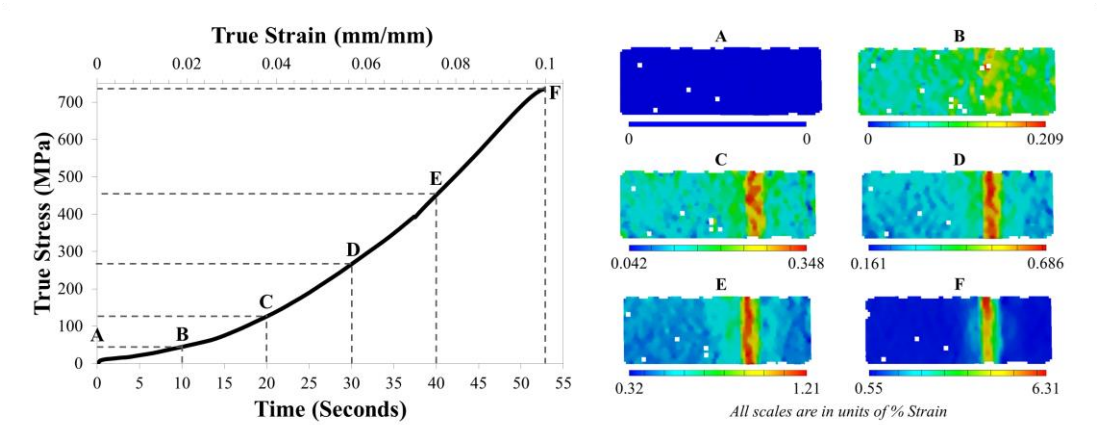

Figure 3.1. (left) Representative tensile results of true stress versus time and true strain for a EBW Ti-5553 tensile specimen in the AW condition and (right) corresponding localized strain distributions from ARAMIS for the same tensile specimen at times of 0 seconds (A), 10 seconds (B), 20 seconds (C), 30 seconds (D), 40 seconds (E), and immediately prior to failure (F) – approximately 53 seconds (the tensile direction is oriented horizontally).

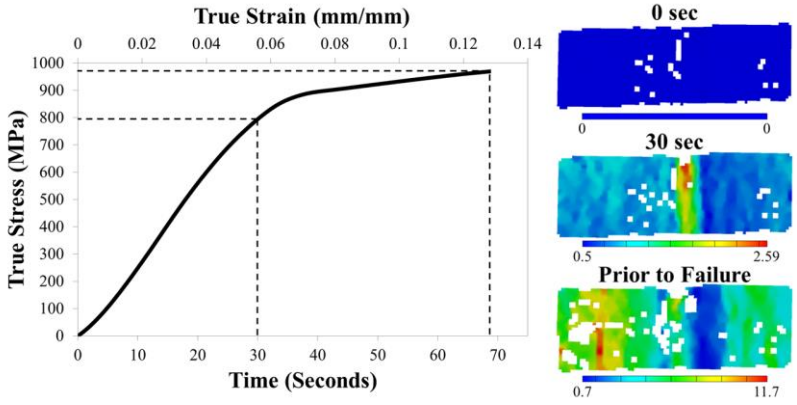

Figure 3.2. (left) Representative tensile results of true stress versus time and true strain for a EBW Ti-5553 tensile specimen heat treated at 700°C/4 hours and (right) corresponding localized strain distributions from ARAMIS for the same tensile specimen at times of 0 seconds, 30 seconds, and immediately prior to failure – approximately 67 seconds (the tensile direction is oriented horizontally).

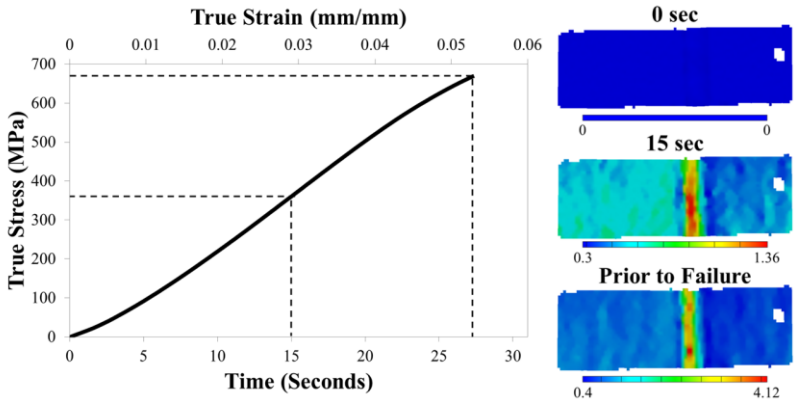

Figure 3.3. (left) Representative tensile results of true stress versus time and true strain for a EBW Ti-5553 tensile specimen heat treated at 804°C/1 hour and (right) corresponding localized strain distributions from ARAMIS for the same tensile specimen at times of 0 seconds, 15 seconds, and immediately prior to failure – approximately 24 seconds (the tensile direction is oriented horizontally).

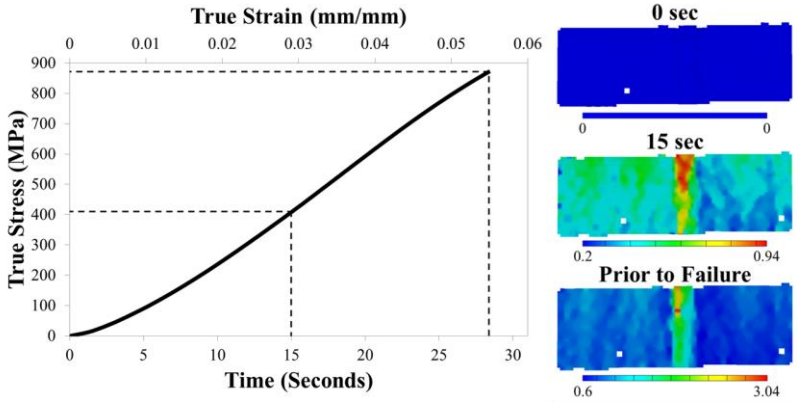

Figure 3.4. (left) Representative tensile results of true stress versus time and true strain for a EBW Ti-5553 tensile specimen heat treated at 804°C/1 hour then aged at 600°C/4 hours and (right) corresponding localized strain distributions from ARAMIS for the same tensile specimen at times of 0 seconds, 15 seconds, and immediately prior to failure – approximately 26 seconds (the tensile direction is oriented horizontally).

The ultimate tensile strength (UTS) for each specimen was taken as the maximum stress at failure. The average UTS for each of the four conditions, AW, 700°C/4 hours, 804°C/1 hour, 804°C/1 hour + 600°C, were determined to be 735 MPa, 975 MPa, 647 MPa, and 873 MPa, respectively. A summary of the results are given in Table 3.1. Compared to the UTS of Ti-5553 reported by Harper [Harper, 2004], Fanning [Fanning, 2005] and Mitchel et al. [Mitchel et al., 2011], which were significantly greater than 1000 MPa in some heat-treated conditions, the present values are clearly lower. The UTS for Ti-5553 reported in literature are greater due to the

absence of welds, which can function as defects in tensile specimens during loading because of abrupt changes in microstructure, geometry, and localized changes in mechanical properties. The presence of α-phase and of ω-phase (both of which will be discussed in 3.4) can severely affect the mechanical properties of the weld zone. The PWHTs clearly affected the UTS when compared to that of the AW condition. The PWHTs at 700°C/4 hours and 804°C/1 hour followed by aging at 600°C/4 hours imparted increases in UTS by 33% and 19%, whereas the PWHT at 804°C/1 hour decreased the UTS by 12%.

Table 3.1. Average yield and ultimate tensile strengths along with the localized tensile strain in the vicinity of the WZ from ARAMIS for EBW Ti-5553.

Condition	**Average True YS (MPa)**	**Average True UTS (MPa)**	**Localized Strain in the Vicinity of the Weld Zone (%)**
AW	N/A	735	6.31
700°C/4h, AC	864	975	9.5
804°C/1h, AC	N/A	647	4.12
804°C/1h, AC + 600°C/4h, AC	N/A	873	3.04

In order to determine the average localized strain within the WZs of each specimen, ARAMIS was used to map the strain distribution in the vicinity of the WZs. Figures 3.1 through 3.4 also show strain distribution maps from ARAMIS for selected time intervals. Strain becomes localized within the weld zone, which leads to subsequent fracture through the weld zone. The average, peak localized strains recorded prior to fracture are displayed in Table 3.1. Due to their relative ductility, the specimens heat-treated at 700°C/4 hours also accommodated the highest degree of localized strain within the WZs prior to fracture, with an average value of 9.5%. The specimens heat-treated at 804°C/1 hour + 600°C/4 hours, on the other hand, accommodated an average localized strain of 3.04% prior to fracture. Specimens in the AW condition and those heat-treated at 804°C/1 hour accommodated strains of 6.31% and 4.12%, respectively. Harper reported results for unweled Ti-5553 subjected to similar heat treatments consisting of only

solutioninzing at 910°C then cooling to room temperature or solutionizing at 910°C/15 minutes then aging at 660°C/4 hours, at 810°C/2 hours then at 610°C or 510°C for 4 hours, or at 700°C/2 hours then at 610°C or 510°C for 4 hours, for which the elongations were 6%, 6.2%, 2.4%, 1.3%, 9.6%, and 2.5%, respectively. The localized strains found in the vicinity of the WZs in EBW Ti-5553 fall within the range of the elongations reported by Harper for Ti-5553, implying that the WZs can accommodate strains comparable to bulk, un-welded Ti-5553.

Microhardness measurements were made from the BM, across the WZ, to the BM in 200 μm increments. The results are shown graphically in Figures 3.5 and 3.6 and the average hardness for the BM, HAZ, FZ for each condition are given in Table 3.2. In the AW condition the hardness of the HAZs and FZs decreased below that of the BM (363 HV) to average values of 325 HV and 313 HV, respectively. Each subsequent PWHT, however, homogenized the hardness of the specimens and resulted in equivalent hardnesses across the BM, HAZ, and FZ for each specimen. The PWHT at 700°C/4 hours increased the hardness of the HAZs and FZ as well as the BM to an average hardness of 390 HV. The PWHT conducted at 804°C/1 hour provided little strengthening and homogenized the hardness to an average value of 323 HV. Heat-treating the EBW specimens at 804°C/1 hour + 600°C/4 hours imparted an average hardness across the specimen of 426 HV. These results show a similar trend between the AW condition and the three PWHT conditions; however, the heat treatment at 804°C/1 hour followed by aging at 600°C/4 hours imparted in a higher hardness than the PWHT at 700°C/4 hours, whereas the PWHT at 700°C/4 hours resulted in a higher UTS than the PWHT at 804°C/1 hour + 600°C/4 hours.

Table 3.2. Average hardness of the BM, HAZ, and FZ in EBW Ti-5553 (all values are Vickers hardness – HV).

Condition	**BM**	**HAZ**	**FZ**
AW	363	325	313
700°C/4h, AC	----------	390	----------
804°C/1h, AC	----------	323	----------
804°C/1h, AC + 600°C/4h, AC	----------	426	----------

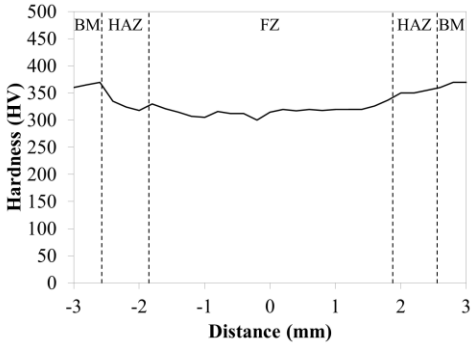

Figure 3.5. Hardness profile across the weld from BM to BM in EBW Ti-5553 in the AW condition.

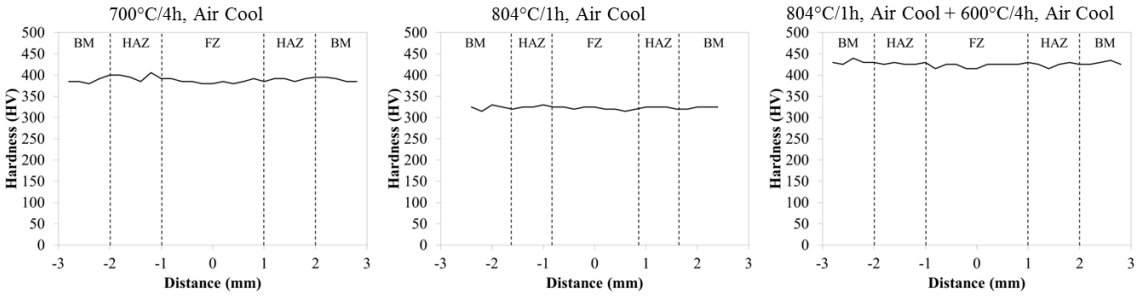

Figure 3.6. Hardness profiles across the welds from BM to BM in EBW Ti-5553 subjected to PWHTs (left) at 700°C/4 hours, (center) at 804°C/1 hour, and (right) at 804°C/1 hour followed by aging at 600°C/4 hours.

3.1.1. Section 3.1 Summary

Mechanical testing showed that the PWHT improved the strength of the WZs over the AW condition in all cases except for the PWHT at 804°C/1 hour. This PWHT reduced the hardness of the FZ, HAZs, and BM below that of the as-received material and failure occurred at lower stresses than in the AW condition. The average UTS (the stress at fracture) for the EBW Ti-5553 specimens were all low compared to reported values for Ti-5553 with similar thermal histories. Interestingly, no macroscopic ductility was exhibited by any of the specimens. However, 3D DIC revealed that strain was localized within the WZs of every specimens and that the peak localized strains in vicinity of the WZs were similar or greater than reported values for un-welded Ti-5553 given similar heat treatments.

3.2. Microstructure

3.2.1. As-Welded Condition

Figure 3.7 shows a representative cross-section of an entire electron beam weld including the FZ, HAZs, and BMs in Ti-5553. Due to the very fine, rolled structure of the BM, its microstructure appears black. Columnar grains, characteristic of directional solidification in welds can be clearly observed to exist within the FZ. At higher magnifications (Figure 3.8a), cellular dendrites are evident; their presence can be attributed to high solute content and constitutional supercooling. This is typical in alloys with high solute contents experiencing relatively shallow temperature gradients [Porter and Easterling, 2004]. It should also be noted that the columnar grains within the fusion zone grew epitaxially from grains within the HAZ at the FZ/HAZ boundary as seen in Figure 3.8b. This is evident at the interface between the FZ and HAZ where grains from the HAZ extend beyond the boundary and transform into the columnar grains of the FZ. Epitaxial growth is common in fusion welds during solidification, because the partially melted grains between the FZ and HAZ, which are favorably oriented (where the ⟨100⟩ direction is most closely parallel to the direction of heat flow), serve as preferential sites for the start of solidification and formation of grains within the weld pool.

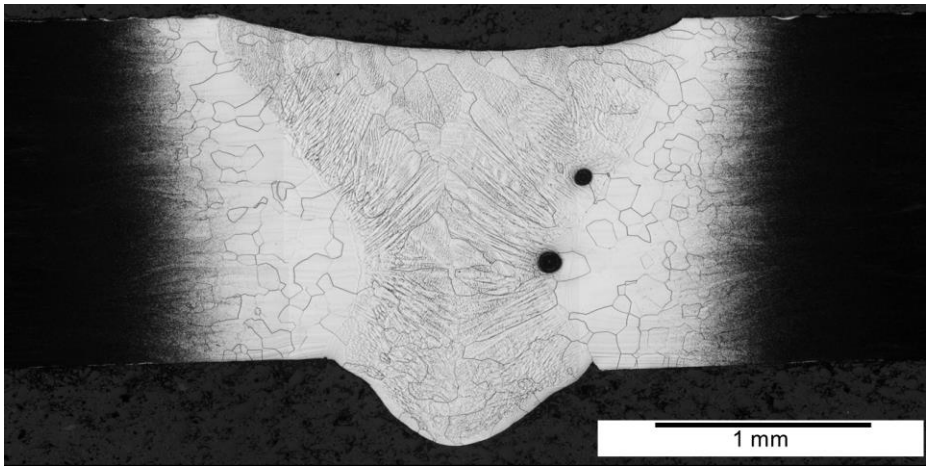

Figure 3.7. Representative image of the weld cross-section from an EBW Ti-5553 specimen in the as-welded condition (etched in Kroll's using an etch-polish-etch technique). The two black spots at the FZ/HAZ boundary are pores, which developed during solidification [Sabol et al., 2012].

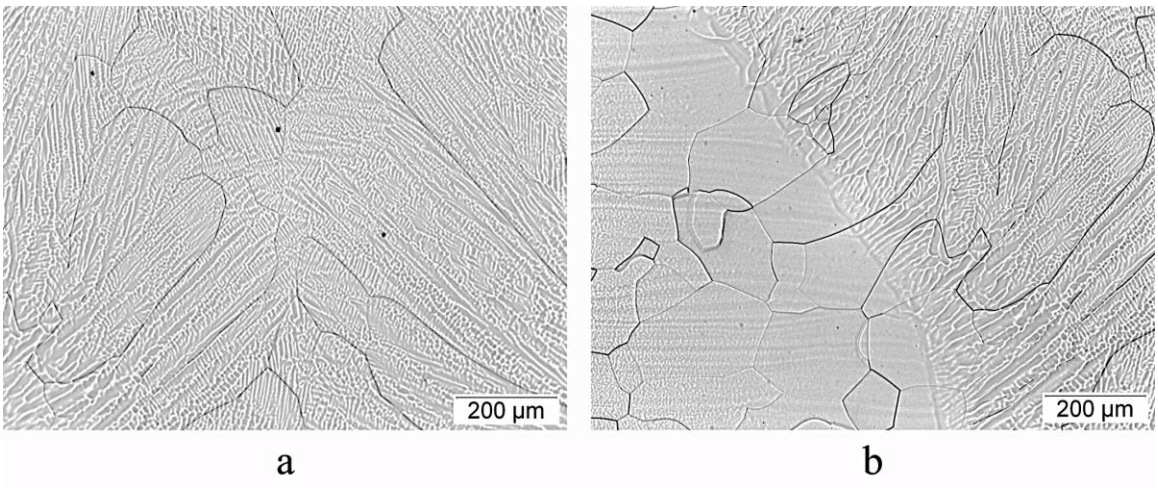

Figure 3.8. Representative images from and EBW Ti-5553 specimen in the as-welded condition of (a) the weld centerline in the fusion zone detailing the cellular dendritic structure and (b) the boundary between the heat affected zone (left side in b) and the fusion zone (right side in b) [Sabol et al., 2012].

The HAZs consist of equiaxed grains, which are larger at the FZ/HAZ boundary and decrease in size with distance away from the FZ (Figure 3.9). The equiaxed morphology of the grains and decreasing size with distance from the FZ is consistent with the thermal gradient experienced by the HAZ. The entire HAZ is heated to temperatures that fall within the β-phase regime (856°C-1700°C), a solid and single-phase region. Temperatures near the maximum temperature limit of the β-phase regime are experienced close to the FZ/HAZ, while regions closer to the HAZ/BM transition experience temperatures much lower and nearing the lower temperature limit of the β-phase regime. Fundamentally, higher temperatures increase the rate of grain growth and promote the formation of larger grains, which explains the decreasing grain size in the HAZ with distance from the FZ. Simultaneously, remaining at elevated temperatures above the β-transus (856°C) causes all second phases to go into solution as well as incite recrystallization of the previous grain structure ultimately leading to equiaxed grains containing no precipitates.

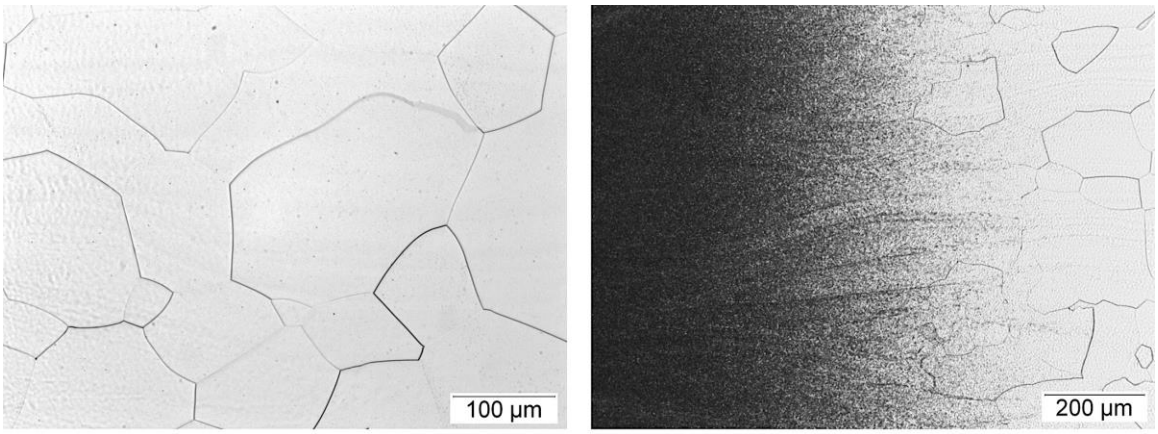

Figure 3.9. Representative images from an EBW Ti-5553 specimen in the as-welded condition of (a) the equiaxed grains within the HAZ and (b) the transition from the HAZ to the BM [Sabol et al., 2012].

In the regions of the FZ and HAZs no secondary phases are evident. This is due to the temperatures experienced by the FZ and HAZs, which were above the β-transus temperature (856°C) for Ti-5553 in the single-phase β regime. Within this single-phase regime, all second phases should go back into solution leaving only β. It is well known for metastable β alloys that upon quenching from any temperature above the β-transus, an entirely β structure will be retained at room temperature. The high β-stabilizer content of Ti-5553, like other metastable β-Ti alloys, promotes the stabilization of β upon cooling and suppresses α and the martensitic variants of α (α′ and α″). Recalling Figure 2.2, Ti-5553 should sit just beyond the M_s line and is expected to retain β upon quenching, which supports the observed lack of precipitates in the FZ and HAZ. This, coupled with the high cooling rate associated with EBW (~5000 °C/s as estimated from the power input – 450W, travel speed – 8.5 mm/s, plate thickness – 1.6 mm, and BM temperature – 23°C), strongly suggests that EBW Ti-5553 should retain a fully β structure in the HAZs and FZ after welding. While α, α′, and α″ may be suppressed, ω-phase is known to form from the decomposition of β upon cooling from elevated temperatures no matter the cooling rate. However, it cannot be resolved using LOM or SEM techniques because it is reported to be

present on the order of 5-10 nm and coherent with the β matrix [Sukedai et al., 1991; Nag et al., 2009, Devaraj et al., 2012]. Confirmation of its presence is discussed later in 3.4.2.

3.2.2. Post Weld Heat Treatment Conditions

Subsequent to EBW, PWHTs were performed on the AW specimens to see the effects of precipitation on microstructure and mechanical properties. Figure 3.10 shows cross-sections of EBW Ti-5553 specimens after PWHTs at 700°C/4 hours (Figure 310a), 804°C/1 hour (Figure 3.10b), and 804°C/1 hour followed by aging at 600°C/4 hours (Figure 3.10c). In stark contrast to the AW condition (Figure 3.7), the PWHTs precipitated a second phase, which is clearly evident within the FZs and HAZs of the three heat-treated specimens. Not only were the microstructures of the FZs and HAZs altered, but that of the BMs was also changed. This change is evident in the shape and size of the precipitates within the BM, which was unchanged from the as-received material in the AW specimens. The grain structures of the FZs, HAZs, and BMs were not altered from that of the AW condition, i.e. columnar grains still existed in the FZs and equiaxed grains whose size decreased with distance from the FZ remained in the HAZs while the rolled grain structure still remained in the BM. The PWHTs did, however, delineate the sub-critical HAZ (SCHAZ) – a region that was subjected to temperatures below the β-transus, 856°C, but still high enough to cause some dissolution of the α during welding – within the specimens, which was not discernable in the AW condition. Because of the appearance of the SCHAZ, the region closest to the FZ can be denoted as the critical HAZ (CHAZ) wherein the temperature, like in the HAZ of the AW specimens, was above the β-transus (critical temperature) within the β-phase regime (856°C-1700°C). That the SCHAZ was not apparent in the AW specimens, does not mean that it did not exist, but rather that it was less obvious due to it's the retention of the microstructure found in the as-received BM. The SCHAZ is most noticeable in the specimens heat-treated at 700°C/4hours and can be seen just beyond CHAZ (Figure 3.10a), but it is present in all specimens.

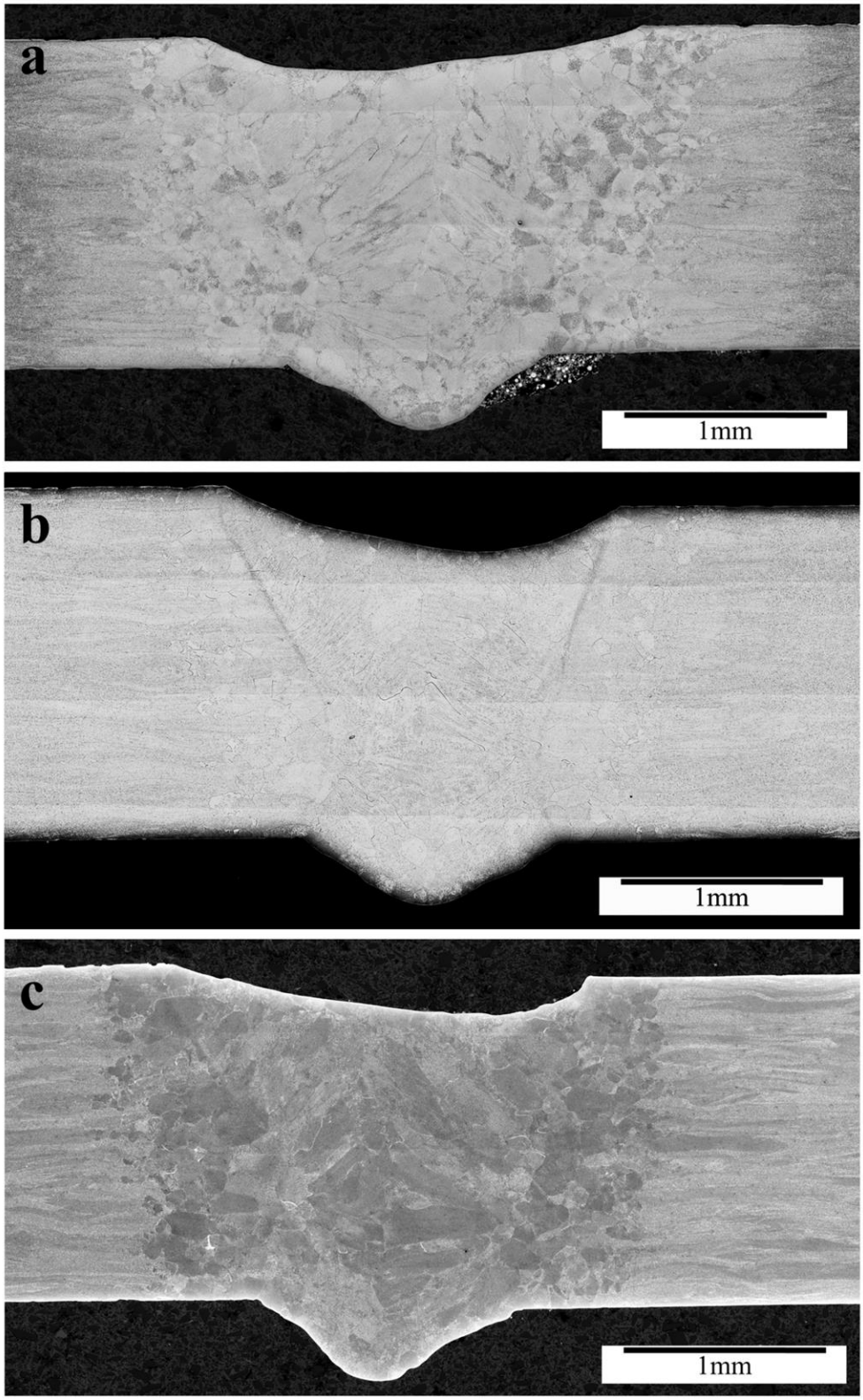

Figure 3.10. Representative images of weld cross-sections from EBW Ti-5553 after PWHTs at (a) 700°C/4 hours, (b) 804°C/1 hour, and (c) 804°C/1 hour followed by aging at 600°C/4 hours (etched in Kroll's using an etch-polish-etch technique).

Figure 3.11 shows images of the BM, SCHAZ, CHAZ, and FZ from each of the PWHT specimens at higher magnifications. Each of the three PWHTs produced different microstructures within the FZ, CHAZ, SCHAZ, and BM consisting of α that precipitated as platelets within the β grains and as continuous layers at the β grain boundaries. The formation of α at grain boundaries is unavoidable in solute lean and metastable β-Ti alloys [Lütjering and Williams, 2007; Polmear, 1995]. The precipitates were identified as α, because other phases, such as α′ (martensite), are suppressed due to the high β-stabilizer content and ω-phase, which is too small and coherent with the β matrix to be resolved by LOM or SEM techniques. However, ω-phase cannot be discounted. Confirmation of its presence, as well as α's, is discussed in section 3.4. The difference between the microstructures produced from the different PWHTs is the size, shape, and distribution of the α platelets. In the specimens heat-treated at 700°C/4 hours a relatively fine dispersion of small, uniform α platelets was found to decorate the interiors of the grains as seen in Figure 3.11a-d. Larger α platelets, coarsely dispersed within the β grains were observed in the specimens heat-treated at 804°C/1 hour (Figure 3.11e-h). The heat treatment at 804°C/1 hour followed by aging at 600°C/4 hours resulted in a microstructure consisting of a combination of coarse, dispersed α platelets (due to the heat treatment at 804°C/1 hour), surrounded by significantly smaller, finely dispersed α platelets (due to the second heat treatment at 600°C/4 hours, Figure 3.11i-l).

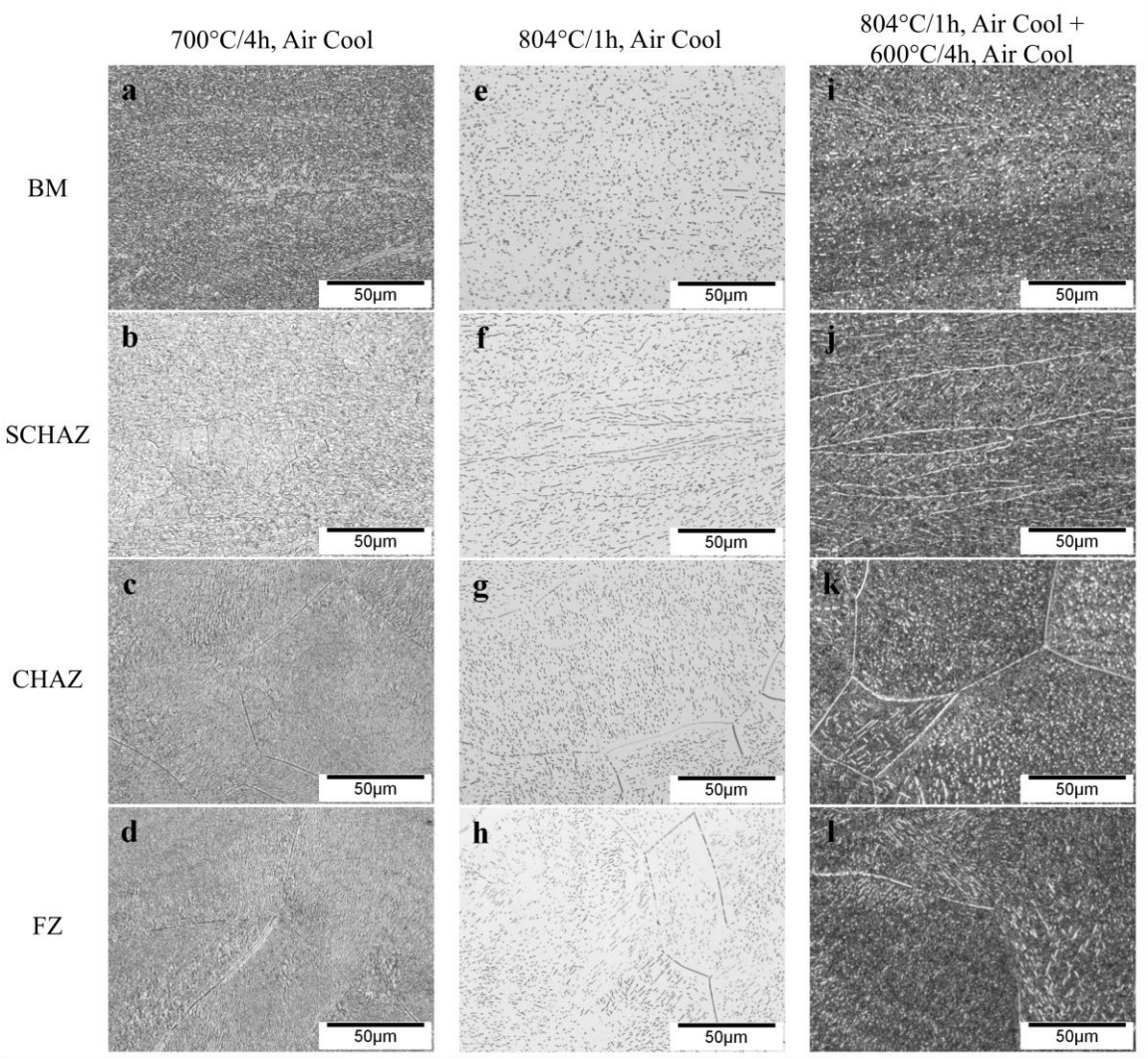

Figure 3.11. Representative images of the BM, SCHAZ, CHAZ, and FZ from each of the PWHTs at (a-d) 700°C/4 hours, (e-f) 804°C/1 hour, and (i-l) 804°C/1 hour followed by aging at 600°C/4 hours.

While the α platelets in the specimens heat-treated at 804°C/1 hour could be easily resolved using LOM techniques, those in the specimens subjected to the other two heat-treatments could not be clearly observed. SEM techniques, however, provided higher resolution, with which to see the α precipitates. In the BMs a definite difference in the morphology, size, and distribution of the α precipitates can be seen between the three PWHTs (Figure 3.12) as well as in the BM in the AW condition (Figure 3.13). The BMs consisted of mixed precipitate morphologies and sizes of globular and plate-like α with strings of globular α at the grain

boundaries. Precipitates within the BM of specimens heat-treated at 700°C/4 hours took on a predominantly globular or semi-cuboidal shape with interspersed plates. The precipitates are uniformly distributed and most closely resemble those found in the BM of the AW specimens, however, with fewer plate-like precipitates. Grain boundaries in the same PWHT specimens contain strings of elongated, globular α, which delineate the rolled grain morphology of the BM. The sparsest and most non-uniform precipitates were exhibited by the specimens heat-treated at 804°C/1 hour. The BM contained globular and plate-like α on a scale of similar size to those in the specimens heat-treated at 700°C/4 hours, but with a significantly lower volume fraction of α. Grain boundary α was still present, but not as obvious as in the other PWHT specimens or AW specimens. The grain boundary α is most noticeable as the plate-like precipitates, directionally oriented with the rolling direction (horizontally across the page). The specimens heat-treated at 804°C/1 hour followed by aging at 600°C/4 hours contained an almost bi-modal distribution of precipitates. Globular α exists primarily at the grain boundaries with some of the grain boundary α becoming continuous layers. Within the grains fine, uniformly dispersed α platelets were found that assumed a somewhat needle-like shape and were arranged in a semi-basket weave or hatch pattern.

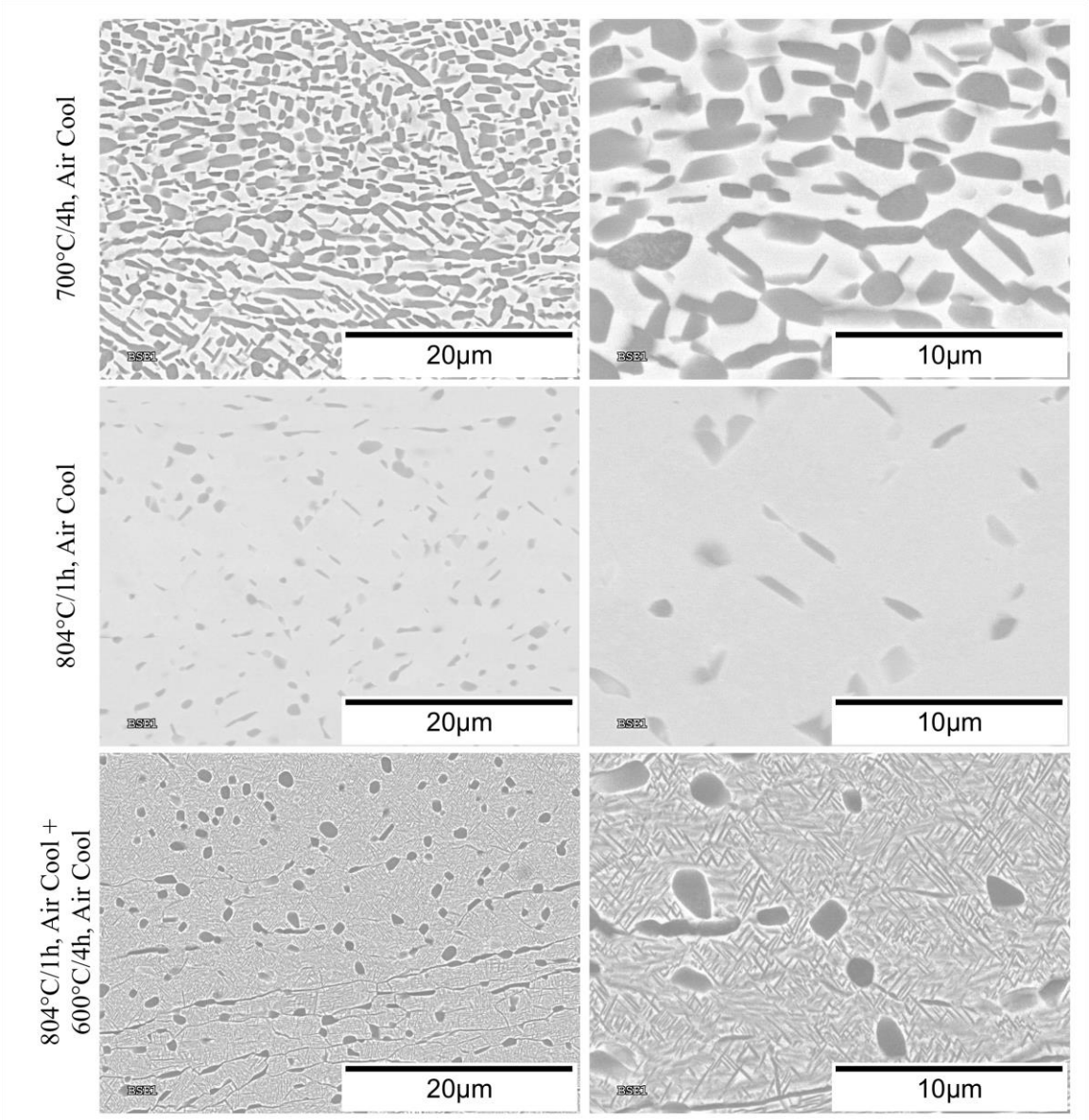

Figure 3.12. Backscatter secondary electron images of the BM in each of the PWHT conditions at lower magnification (left) and higher magnification (right).

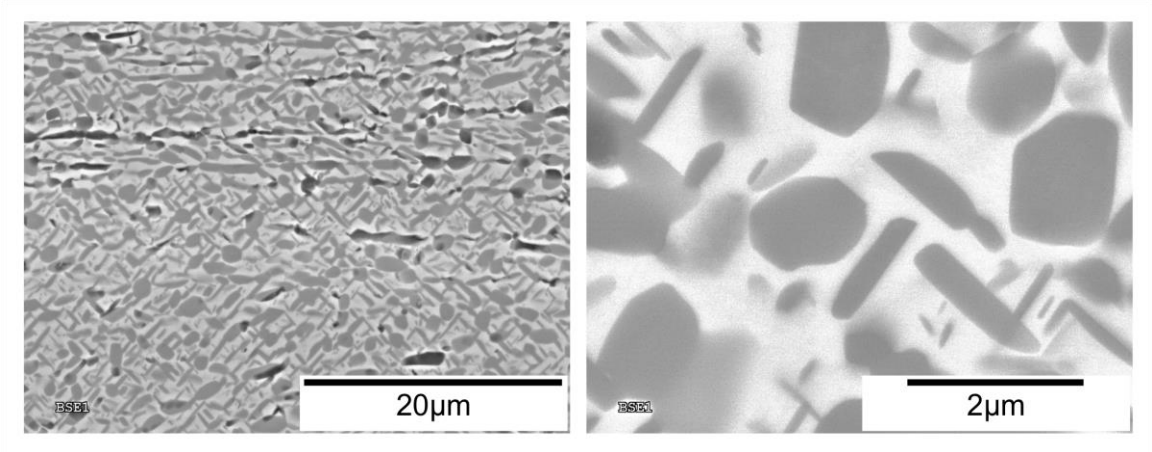

Figure 3.13. Backscatter secondary electron image of the BM in the AW condition at lower magnification (left) and higher magnification (right).

The SCHAZs in the PWHT specimens displayed increasingly more continuous layers of α at the grain boundaries and almost no globular α precipitates (Figure 3.14). The plates in the SCHAZ of specimens heat-treated at 700°C/4 hours became finer and uniformly dispersed with relatively uniform size. In specimens heat-treated at 804°C/1 hour α plates in the grain interiors were not prevalent, but the occurrence of α along the grain boundaries increased as did α's size compared to the BM. The SCHAZs of specimens heat-treated at 804°C/1 hour followed by aging at 600°C/4 hours had considerably greater amounts of continuous grain boundary α than the SCHAZs of the two other PWHT conditions. The SCHAZs also had the same fine, uniform, evenly dispersed platelets as those found in the BM.

Specimens heat-treated under the same conditions contain CHAZs and FZs that are almost identical to one another (Figures 3.15 and 3.16). The only difference is the size and shape of the grains; the FZ is made up of columnar grains while the CHAZ is made up of equiaxed grains. In these two regions, continuous grain boundary α is present and plate-like α precipitates are present throughout the interior of the β grains. The α platelets in the specimens heat-treated at 700°C/4 hours are fine (~1-5 µm) and homogeneously distributed, whereas the precipitates in specimens heat-treated at 804°C/1 hour appear coarser and are coarsely distributed. The specimens heat-treated at 804°C/1 hour followed by aging at 600°C/4 hours have elements

similar to each of the PWHT microstructures. These specimens combine the coarse precipitates found in specimens heat-treated at 804°C/1 hour and the fine, uniform precipitates similar to those found in the specimens heat-treated at 700°C/4 hours. However, unlike the precipitates formed in the specimens heat-treated at 700°C/4 hours, the α precipitates are finer and are more densely distributed.

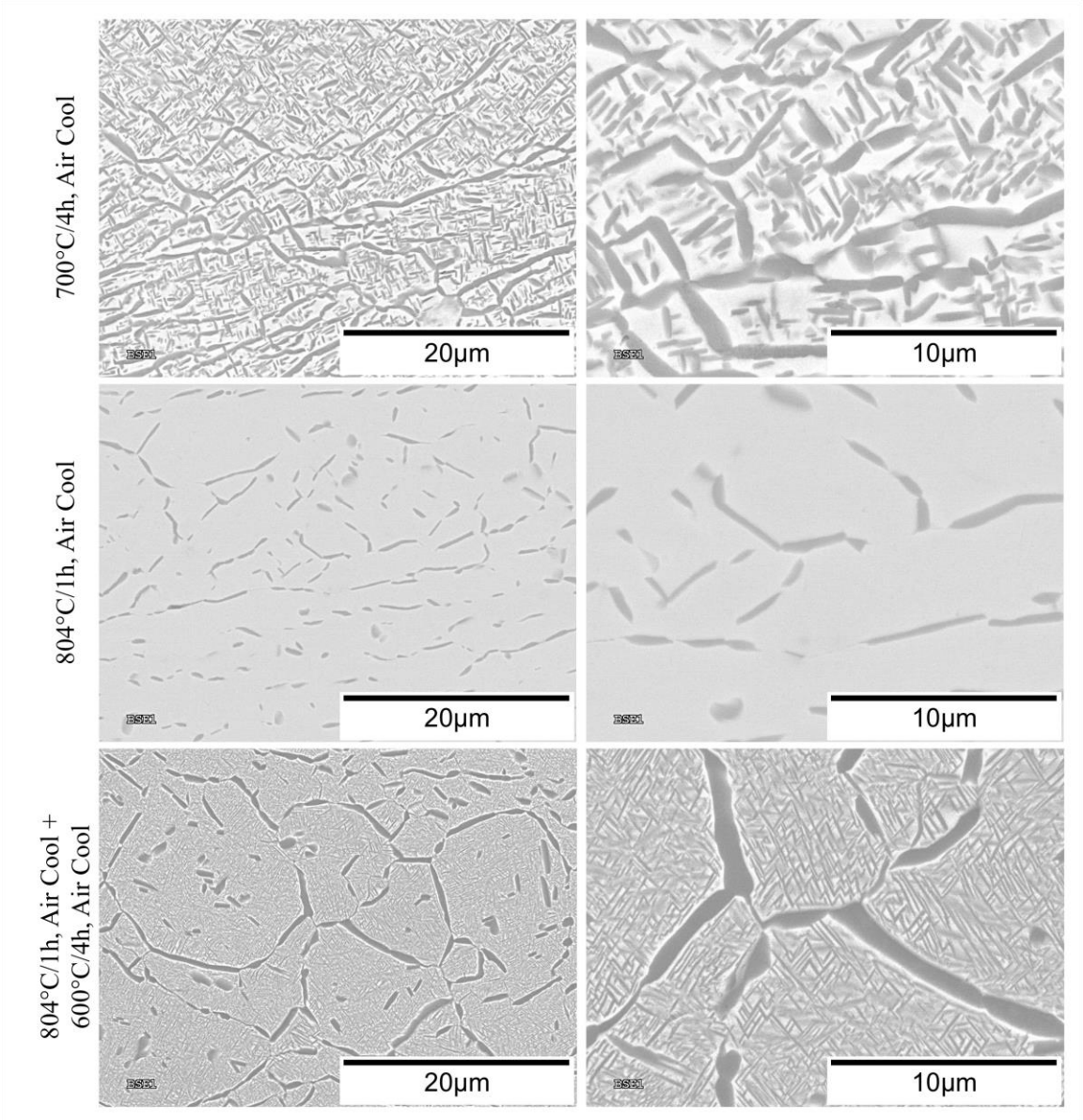

Figure3.14. Backscatter secondary electron images of the SCHAZ in each of the PWHT conditions at lower magnification (left) and higher magnification (right).

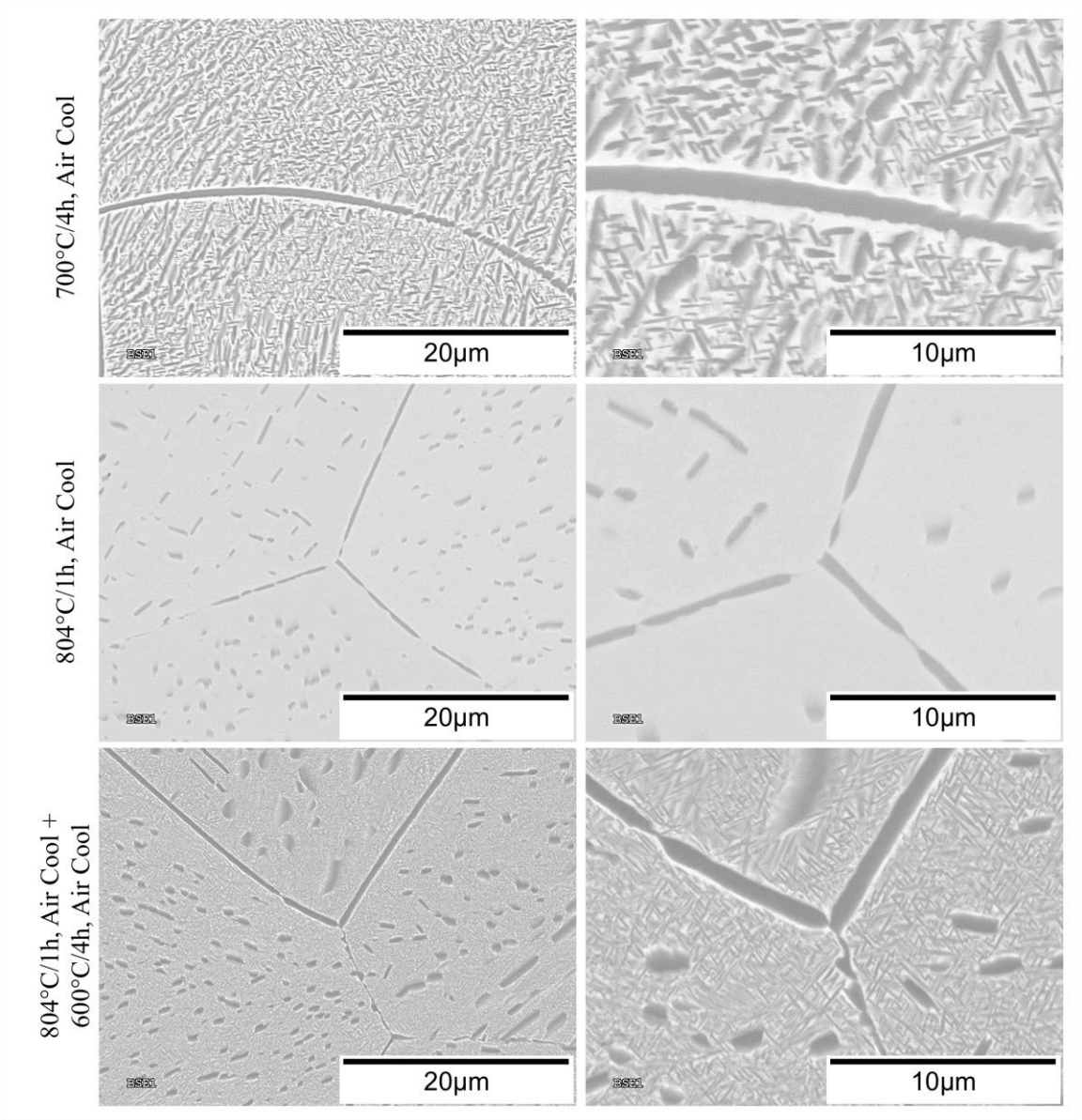

Figure3.15. Backscatter secondary electron images of the CHAZ in each of the PWHT conditions at lower magnification (left) and higher magnification (right).

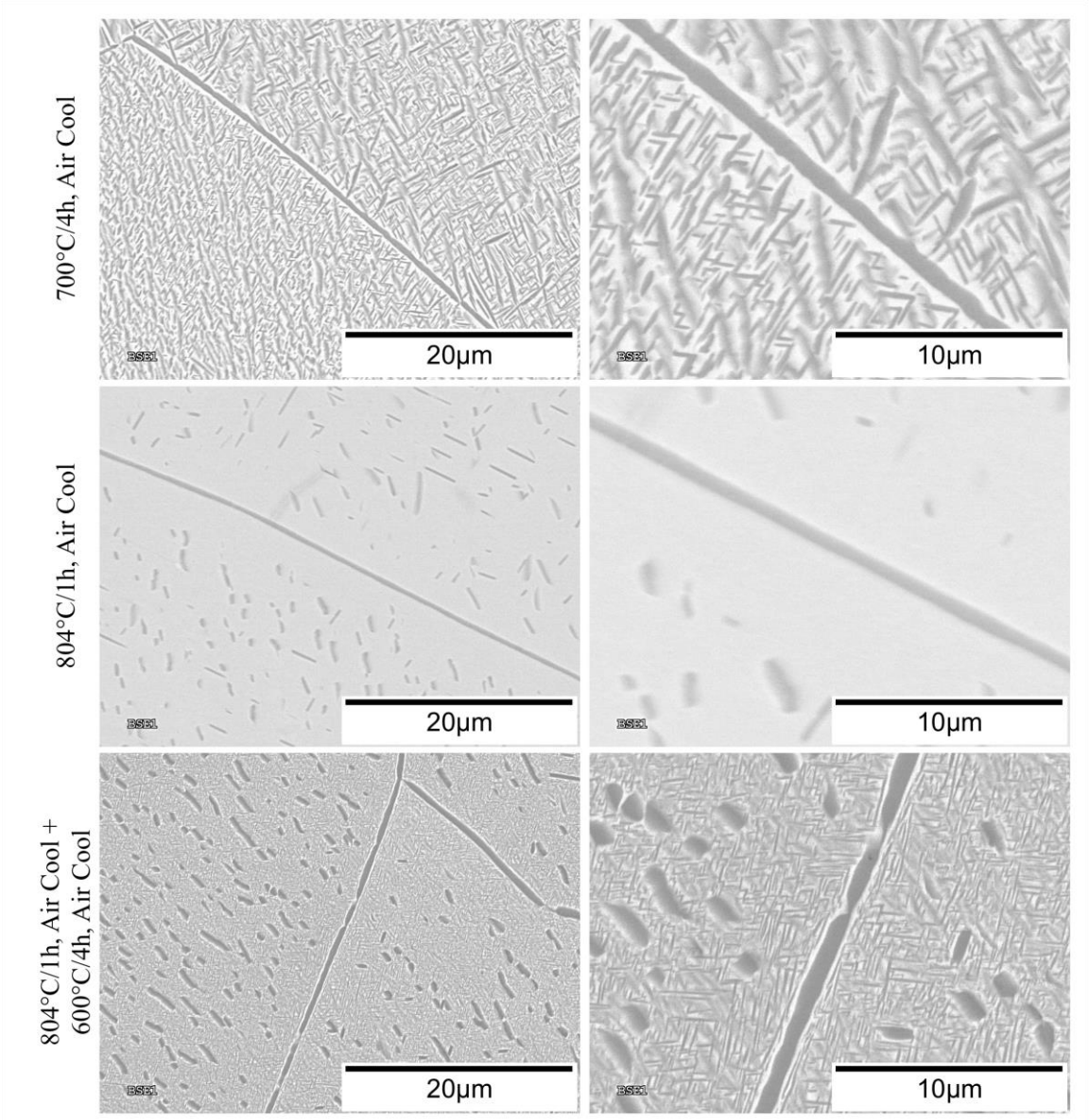

Figure3.16. Backscatter secondary electron images of the FZ in each of the PWHT conditions at lower magnification (left) and higher magnification (right).

The differences in α precipitate size and distribution can be explained by the simple application of the lever law and pseudo binary phase diagram. Using the lever law, the relative amounts of phases can be determined at the three different PWHT temperatures as follows

$$X_\beta = \frac{C_o^{Ti-5553} - C_\alpha^{Ti-5553}}{C_\beta^T - C_\alpha^T} \qquad \text{Eq. 3.1}$$

$$X_\alpha = \frac{C_\beta^{Ti-5553} - C_o^{Ti-5553}}{C_\beta^T - C_\alpha^T} \qquad \text{Eq. 3.2}$$

where X_β and X_α are the fractions of β and α present in the microstructure at a given temperature, respectively, according to the equilibrium pseudo binary phase diagram. $C_o^{\text{Ti-5553}}$ is the nominal composition of Ti-5553, C_β^T is the composition of the β-phase at a given temperature, and C_α^T is the composition of the α-phase at a given temperature.

The lever law shows that, at higher temperatures, the fraction of α is reduced and the fraction of α can be determined from tie lines in the equilibrium pseudo binary phase diagram (Figure 3.17), where $(C_\beta^{804°C} - C_o^{\text{Ti-5553}}) < (C_\beta^{700°C} - C_o^{\text{Ti-5553}}) < (C_\beta^{600°C} - C_o^{\text{Ti-5553}})$. This is experimentally confirmed by the smaller number of α precipitates in the specimens heat treated at 804°C/1 hour and the greater number of α precipitates in specimens subjected to 700°C/4 hours. At higher temperatures, diffusion is also faster, which allows atoms to migrate greater distances in shorter amounts of time. This causes coarser microstructures to develop with smaller fractions of α precipitates, because the β-phase is further stabilized due to the increased mobility of heavier atoms, such as Mo, that segregate to the β matrix. As temperatures decrease, the lever law demonstrates that the fraction of α increases compared to the fraction of β. This is clearly evident in the specimens heat-treated at 700°C/4 hours and at 804°C/1 hour followed by aging at 600°/4 hours. The α precipitates are finest and most densely distributed in the specimens exposed to the second aging treatment at 600°C/4 hours after heat treatment at 804°C/1 hour. The lower temperatures decrease diffusivity and the distance over which atoms can travel in a given time. By decreasing the temperature, the volume fraction of α is increased and the diffusivity of the solute elements is decreased, which effectively reduces the stability of the β-phase. Because the β-phase is less stable, precipitation of a dense network of fine α precipitates occurs. But given sufficient time, the α precipitates would likely coarsen due to the Gibbs-Thompson effect wherein sparse, large particles are more energetically favorable [Porter and Easterling, 2004].

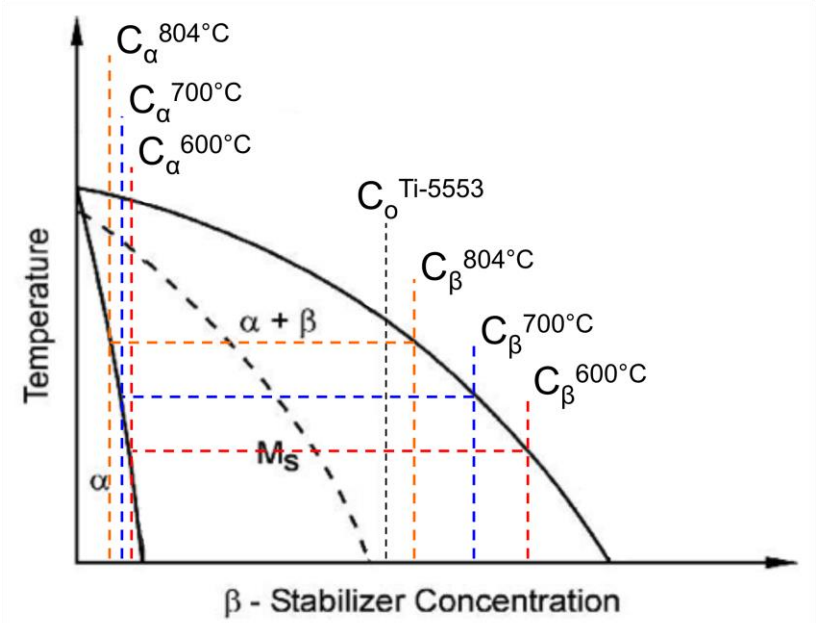

Figure 3.17. Schematic of the equilibrium pseudo binary phase diagram showing the compositions associated with the α- and β-phases at the heat treatment temperatures (700°C, 804°C, 600°C) as well as the nominal [Mo]eq composition of Ti-5553.

Also noticed in the PWHT specimens, particularly in the FZ and CHAZ, were precipitate free zones (PFZs) adjacent to the grain boundary α. The PFZs, also known as soft zones in Ti-alloys (PFZ and soft zone are used interchangeably) varied in width in the specimens heat-treated at 804°C/1 hour followed by aging at 600°C/ 4 hours, at 700°C/4 hours, and at 804°C/1 hour from narrowest (0.5 μm) to widest (6 μm), respectively. These PFZs/soft zones can be seen in Figures 3.15 and 3.16 on either side of the grain boundary α. The remnant soft zones developed in the first step of heat-treating at 804°C/1 hour can be seen in specimens that underwent the duplex heat treatment at 804°C/1 hour and at 600°C/4 hours. Regions, approximately 6 μm wide on either side of the grain boundary α, are devoid of coarse precipitates and are of the same widths as the PFZs observed in the specimens subjected to only the heat treatment at 804°C/1 hour. Upon further aging at a lower temperature and longer time, 600°C/4 hours, fine α precipitates formed within the remnant PFZs caused by the first heat treatment at 804°C/1 hour. Narrow PFZs then developed between the grain boundary α and the fine α precipitates in the remnant PFZs, which were approximately 0.5 μm wide on either side of the grain boundary.

Compared to the PFZs in the specimens heat-treated at 700°C/4 hours, which were slightly wider (~1 μm), the PFZs of the specimens heat-treated at 804°C/1 hour followed by aging at 600°C/4 hours were much more uniform and distinct. It is evident that the width of the PFZs is proportional to the aging temperature.

While the exact reasons for the formation of grain boundary PFZs are not well known, they have been found to exist in Al-alloy systems, Ni-base superalloys, and Ti-alloy systems [Unwin et al., 1969; Okuda et al., 2004; Bechetti, 2013; Qazi et al., 2005; Liu et al., 2014; Lütjering and Williams, 2007; Lütjering et al. 2007; Sauer et al., 2001]. The PFZs arise due to heat-treatments promoting the precipitation of strengthening phases in these alloys. Lütjering et al. [Lütjering et al. 2007] suggest that during the formation of grain boundary α upon aging, Al and O (α-stabilizers) diffuse to the forming layers. This leaves a region depleted in Al and O, effectively stabilizing β. One can then infer that as the aging temperature increases, the diffusion rate of the α-stabilizers to the grain boundary α increases, while at the same time the stability of the β-phase increases at higher temperatures (see Figure 3.17). Because the α-stabilizer diffusion rate increases, the distance over which the α-stabilizers can travel in a given time period also increases leading to wider soft zones.

The postulation for the formation of soft zones adjacent to grain boundary α in β-Ti alloys put forth by Lütjering et al. [Lütjering et al., 2007] provides sound reasoning for the occurrence of soft zones adjacent to grain boundary α in EBW Ti-5553 subjected to PWHTs. Coupled with the simultaneous formation of α plates within the β grains, which grow in a similar fashion with respect to the diffusion of α-stabilizers, the two theories can be used to explain the soft zones found within the FZ and HAZs. Herein the competing precipitation events of α at the grain boundaries and grain interiors may cause a region depleted of α-stabilizing elements. The formation of grain boundary α and precipitation of α platelets within the β grains essentially "sucks" α-stabilizers from the matrix. At the same time, the matrix becomes effectively enriched

in β-stabilizing elements. In theory, this alone should make further precipitation of fine α plates in an α-stabilizer-deficient (β-stabilizer-rich) region difficult, because of the reduced stability of α and increased stability of β. In contrast, uniform precipitation of fine α plates occurred within the remnant PFZs, as observed in the specimens heat-treated at 804°C/1 hour followed by aging at 600°C/4 hours.

However, Nag et al., [Nag et al., 2009a] showed that elemental partitioning during the formation of α-phase in Ti-5553 as a result of aging at 700°C and slow cooling from 1000°C occurred over very small distances (tens of nanometers). Because of this, it can be said that a large, global change in composition is not needed to precipitate α-phase. Only local enrichment in the presence of ω may be responsible for fine scale α-phase nucleation.

Concentration profiles of the alloying elements (Al, Mo, V, Cr, and Fe) across the widths of the PFZ on both sides of a grain boundary were acquired (Figures 3.18-3.20). The peaks (Al) and troughs (Mo, V, Cr, Fe) at zero and at distances up to ±6 μm away correspond to α at the grain boundary and α plates at the ends of the PFZs, respectively. The profiles do not show significant depletion or enrichment of the α- or β-stabilizing elements, except within α precipitates, such as the grain boundary α or α plates at the ends of soft zones. In the α precipitates, the composition is enriched in Al and depleted of Mo, V, and Cr (and to some extent Fe). Of particular interest are the specimens, which were subjected to a heat treatment temperature of 804°C (Figures 3.19 and 3.20). Little distinction can be made between the two concentration profiles, except the slight change in composition of the PFZs in the specimens heat-treated at 804°/1 hour and at 804C/1 hour followed by aging at 600°C/4 hours, which may be attributed to the precipitation of fine α in the latter. This suggests that the PFZs formed during PWHTS in EBW Ti-5553 have compositions of major alloying elements that vary from the bulk by negligible amounts. Ultimately the formation of these PFZs in Ti-5553 does not inhibit

subsequent precipitation of α, because the composition within the PFZs is relatively homogeneous from specimen to specimen.

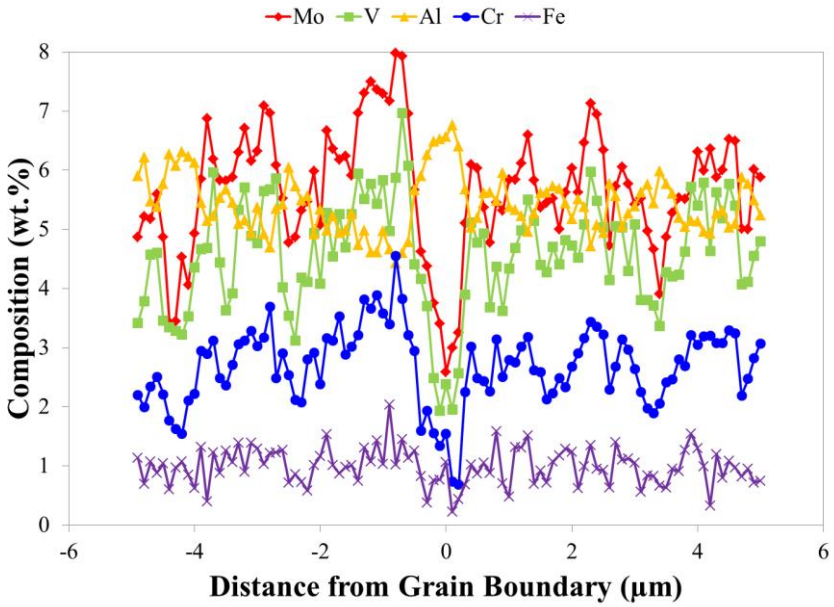

Figure 3.18. Representative composition profile acquired across a grain boundary for a specimen post weld heat treated at 700°C/4h.

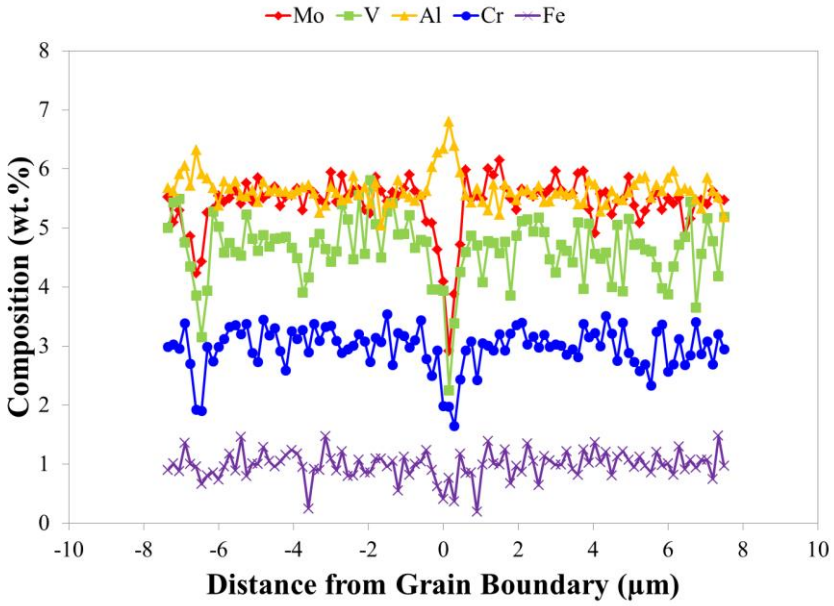

Figure 3.19. Representative composition profile acquired across a grain boundary for a specimen post weld heat treated at 804°C/1 hours.

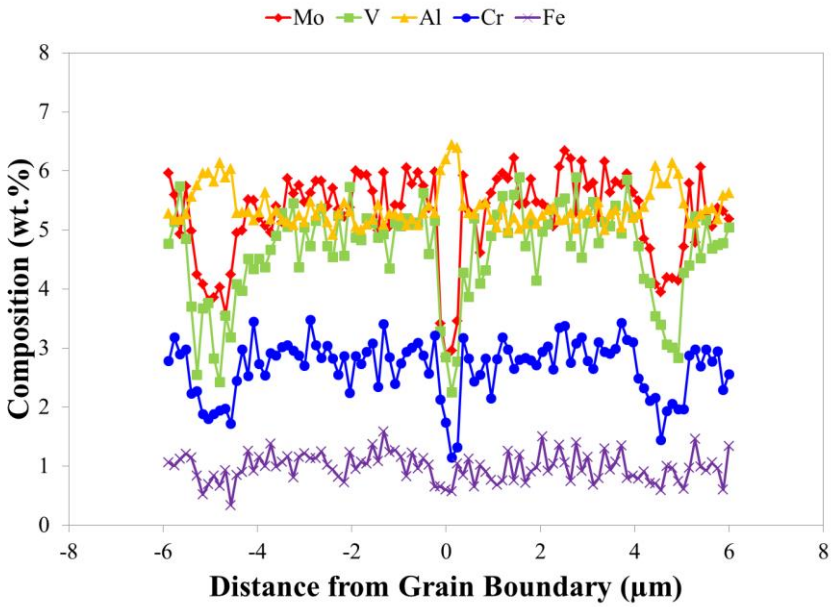

Figure 3.20. Representative composition profile acquired across a grain boundary for a specimen post weld heat treated at 804°C/1 hours followed by aging at 600°C/4 hours.

Due to the fact that the concentration of alloying elements in the PFZs did not change significantly to promote the stabilization of β, the PFZs likely formed due to vacancy diffusion near the grain boundaries. Grain boundaries act as sinks for excess vacancies and at elevated temperatures, the vacancy concentration of a material increases by orders of magnitude from that at room temperature. Not only does the concentration increase, but so does the diffusivity of the vacancies. However, since vacancies have such a high diffusivity they may be "lost" in the vicinity of a grain boundary, because of the discrete discontinuity of the lattice at the boundary [Porter and Easterling, 2004]. Upon aging, the vacancy concentration near the grain boundary will be close to the equilibrium concentration for the aging temperature (deficient in vacancies), while farther away from the grain boundary, the concentration will be closer to that at the solution treatment temperature (enriched in vacancies). In order for nucleation to occur, a critical vacancy supersaturation must be exceeded, which is sensitive to aging temperature and quench rate. The width of the PFZs is determined by the concentration of vacancies, which is relatively low at lower temperatures and high at relatively higher temperatures. At low temperatures, where the

driving force for precipitation is high, narrow PFZs will form, while at higher temperatures the opposite is true. Therefore, the formation of PFZs in the PWHT specimens is most likely caused by vacancy diffusion to the grain boundaries, wherein higher temperatures increase diffusion of vacancies that become lost at the grain boundaries and at the same time inhibiting precipitation, making the PFZ wider.

Since the concentration changes by negligible amounts within the PFZ (Figures 3.#21-3.#23), specifically in the PFZs in specimens subjected to a heat treatment temperature of 804°C, and because vacancy diffusion possibly plays a large part in the formation of PFZs, the subsequent precipitation of α in the PFZ upon aging further at 600°C/4h can be explained by α nucleating in the presence of ω. Many authors have provided evidence to support this [Azimzadeh et al., 1998; Omhori et al., 1998; Williams et al., 1969; Prima et al, 2006]. Nag et al. [Nag et al., Acta Metal., 2009] and Nag et al. [Nag et al., 2012] have even shown this to be possible in Ti-5553 during aging after solutionizing. In the case of the present work on EBW Ti-5553, ω has been confirmed to be present after PWHTs at 804°C/hr suggesting that at this temperature, which is above the ω-solvus for Ti-5553 (ω solvus ~350°C-400°C) [Nag et al., Acta Mater., 2009], and time ω has not completely dissolved upon cooling. Confirmation of ω's presence in the PWHT specimens is discussed in section 3.4.2. Because ω is still present at the beginning of the aging treatment at 600°C, it can serve as a precursor for the precipitation of fine, uniformly dispersed α particles within the remnant PFZs and elsewhere. After aging at 600°C for 4 hours, ω was no longer present (section 3.4.2), but fine α precipitates were observed. This means that sufficient time was available for α to form at ω sites and coarsen, while ω was consumed by its formation or dissolved.

Another way to explain the precipitation of fine α plates in the remnant PFZs during aging at 600°C for 4 hours is to think in terms of Gibbs free energy. Figure 3.21 shows schematic diagrams of the Gibbs free energy versus $[Mo]_{eq}$ at 804°C, 700°C, and 600°C for the Ti-5553

system. As the temperature decreasess the propensity for the stabilization of α increases compared to that of β. This can also be seen in the pseudo binary phase diagram in Figure 3.17, which can be constructed from Gibbs free energy diagrams. If the concentration of α- and β-stabilizers in the PFZs changes by negligible amounts, then precipitation of α-phase during subsequent heat treatments in these regions is possible based on Gibbs free energy. However, if the concentration in a region becomes enriched in β-stabilizers (the $[Mo]_{eq}$ increases slightly from the nominal) it is possible for β to be stabilized as shown by Nag et al. [Nag et al. 2012] in their work on phase transformations from β to α based on compositional fluctuations in Ti-5553.

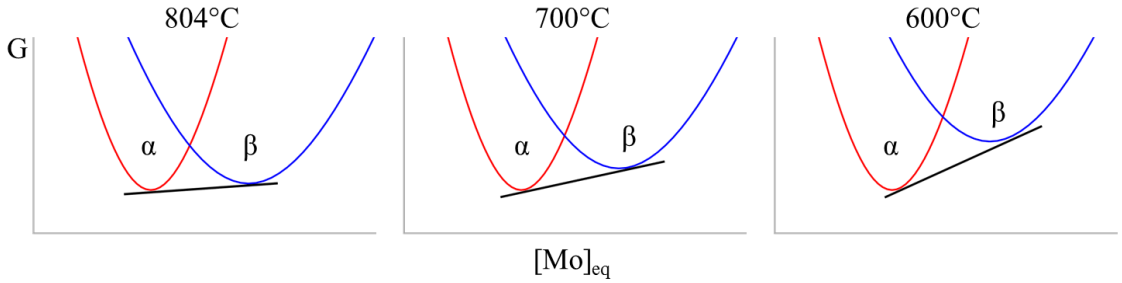

Figure 3.21. Schematics of Gibbs free energy versus temperature for the three PWHT temperatures, 804°C, 700°C, and 600°C (left, center, right).

3.2.3. Section 3.2 Summary

LOM and SEM revealed the microstructures of the EBW Ti-5553 in the AW and PWHT conditions. A fully β microstructure was obtained in the HAZs and FZ as a result of cooling to room temperature after welding. Cellular dendrites formed in the FZ as a result of segregation during solidification. The PWHTs resulted in the precipitation of α at the grain boundaries and α plates in the grain interiors. The size of the α plates was proportional to the PWHT temperature; however, the distribution of the plates became coarser as their size increased. PFZs adjacent to the grain boundary α were also observed in the PWHT specimens. Specimens heat-treated at 700°C/4 hours and at 804°C/1 hour followed by aging at 600°C/4 hours exhibited the narrowest PFZs, while those specimens heat-treated at 804°C/4 hour developed the widest PFZs. Remnants of the PFZs formed during heat-treatment at 804°C/1 hour were observed in the specimens

subjected to two PWHT treatments. They were marked by the appearance of coarse α precipitates at distances from the grain boundaries equal to the width of the PFZs in the specimens heat-treated at 804°C/1 hour. These remnant PFZs filled in with fine α plates after aging at 600°C/4 hours and narrower PFZs developed between them and the preexisting grain boundary α. Negligible compositional changes were found to occur over the widths of the PFZs, indicating that their formation is associated with vacancy diffusion at a given temperature. Vacancy diffusion may also account for the precipitation of α in the remnant PFZs; however, it is also likely that ω acts as a precursor for α nucleation in these regions that causes subsequent precipitation during aging.

3.3. Solidification

3.3.1. Scheil Analysis

As stated in section 3.2, the FZ consists of cellular dendrites as a result of solidification during welding. The cellular dendrites signify a breakdown of planar growth interfaces due to constitutional supercooling [Porter and Easterling, 2004]. They also suggest some degree of elemental segregation. Figure 3.22 shows a representative backscatter electron (BSE) image and the corresponding concentration profile for the FZ in a specimen of EBW Ti-5553 in the AW condition. The location from which the concentration profile was acquired is indicated by the white line on the BSE image.

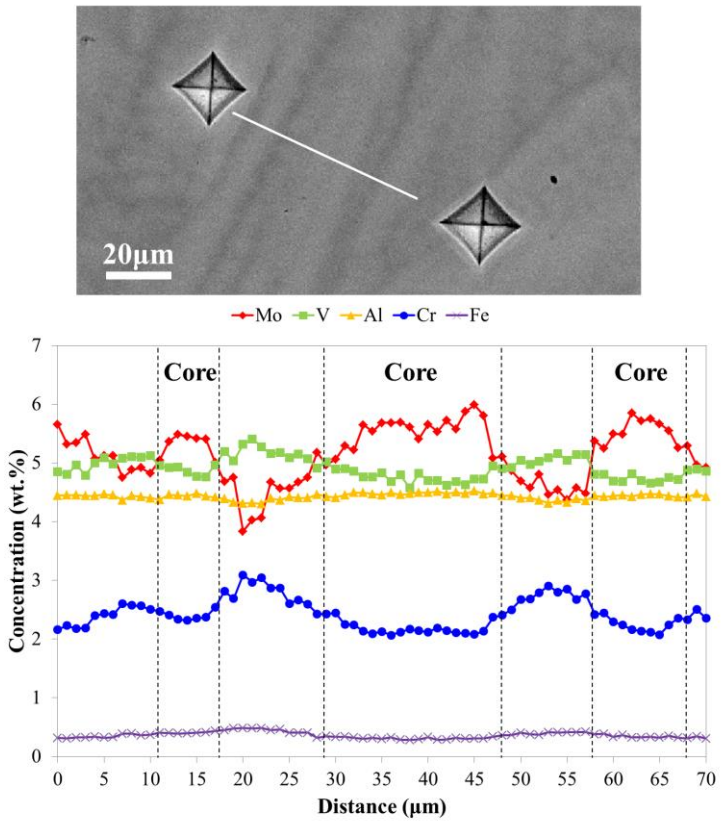

Figure 3.22. Backscatter secondary electron image of cellular dendrites in the FZ of an EBW Ti-5553 specimen in the AW condition (top) and the corresponding concentration profiles of alloying elements across the cellular dendrites generated by EPMA (bottom). The white line in the backscatter image designates the location from which the concentration profiles were acquired.

It should be noted that the average concentration of Al, and to some extent Cr, in the FZ decreased to 4.66 wt.% from the nominal composition (5.03 wt.%) as a result of EBW welding. Figure 3.23 shows the concentration profile obtained across the FZ. This loss of Al is due to evaporation during welding. With relatively higher vapor pressures, Al and Cr have a greater tendency to evaporate compared with V, Mo, and Ti during welding. This vaporization of alloying elements during high energy density fusion processes has been seen by Block-Bolton et al. [Block-Bolton et al., 1984] in 6xxx, 7xxx, 5xxx, and 2xxx series Al alloys, wherein Mg and Zn experienced losses within the weld pool. Sanchez-Amaya et al. [Sanchez-Amaya et al., 2009] also found that evaporation of volatile elements, such as Mg, during laser welding of AA5083 was possible. In another study on the effects of alloy element loss due to vaporization in Al

alloys, Cieslak et al., [Cieslak et al., 1988] found elemental vaporization due to laser welding was detrimental to the hardness of the FZ.

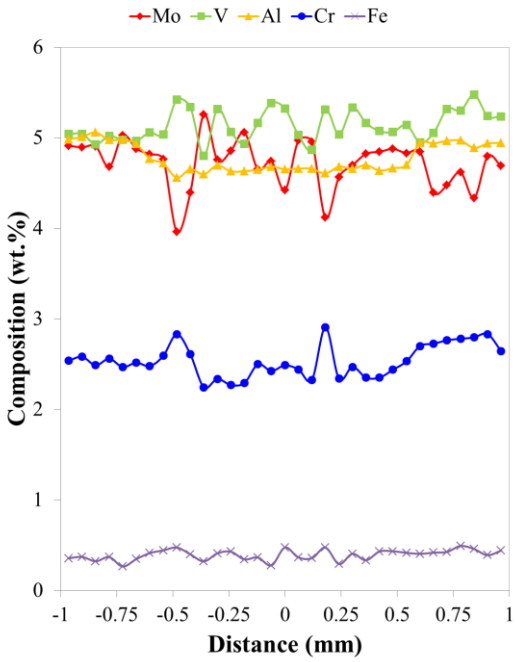

Figure 3.23. EPMA concentration profiles across the FZ from one HAZ to the other showing the depletion of Al in the FZ after EBW of Ti-5553. The FZ composition of Al is approximately 4.66 wt.%Al compared to the nominal composition of 5.03 wt.%Al before EBW.

The combination of the BSE image and the concentration profiles provides convincing evidence that solute segregation occurs during solidification of the FZ. It is evident in the BSE image that the dendrite cores are brighter than the interdendritic regions, meaning that heavier elements were not rejected from the advancing solid into the liquid during solidification. The concentration profiles in Figure 3.22 confirm that the dendrite cores are enriched in Mo and depleted of V, Cr, and to some extent Fe. The interdendritic regions, on the other hand, are depleted of Mo and enriched in V, Cr, and Fe. Al, however, tends to remain in the dendrite cores, but its profile remains relatively flat across the dendrites as seen in Figure 3.22. Even though Al is smaller than the other elements including Ti, it is one of the slower diffusing elements in both α- and β-Ti [Lütjering and Williams, 2007]. Using diffusion data from Gale and Totemeier [Gale and Totemeier, 2004] the diffusivities of the alloying elements of Ti-5553 in α- and β-Ti were

calculated, which showed that Al was one to two orders of magnitude slower than Mo, V, and Cr. Al diffuses slowly through Ti and solute redistribution during solidification has consequently little effect on elemental partitioning of Al at the solid/liquid interface. With this in mind, the small amount of segregation of Al found across the cellular dendrites is reasonable.

The redistribution of solute elements during solidification may be approximated using the Scheil equation (Eq. 3.#).

$$C_s = kC_o(1 - f_s)^{k-1} \qquad \text{Eq. 3.3}$$

$$k = \frac{C_S}{C_L} \qquad \text{Eq. 3.4}$$

C_s is the composition of the solid, C_o is the nominal concentration, C f_s is the fraction of solid, k is the partition coefficient and C_L is the composition of the liquid. The partition coefficient, k, may be used to assess whether a solute element has a strong tendency to segregate to the liquid or solid during segregation. If k is greater than 1 for a particular element, that element will segregate to the solid. Conversely, when k is less than 1 for a particular element, that element will segregate to the liquid. In general, the Scheil equation describes solute redistribution when there is no diffusion in the solid and complete diffusion in the liquid. However, the assumption that solid state diffusion is negligible must first be justified before the Scheil equation can be used.

In order to show that the Scheil equation is valid for the EBW Ti-5553 system, a dimensionless diffusion parameter, α, must be calculated. α is defined as:

$$\alpha = \frac{D_s t_f}{L^2} \qquad \text{Eq. 3.5}$$

Where D_s is the diffusivity of the solute in the solid, t_f is the solidification time, and L is half the dendrite arm spacing (λ/2, λ=14.10±1.89 μm). The solidification time may be thought of as the cooling time between the liquidus and terminal solidus temperatures, i.e. $t_f=\Delta T/\varepsilon$, where ε is the cooling rate. Substituting in for t_f and λ, Eq. 3.5 becomes:

$$\alpha = \frac{4D_s\Delta T}{\varepsilon\lambda^2} \qquad \text{Eq. 3.6}$$

ΔT was approximately 30°C and was found by using a Ti-Mo binary phase diagram [Hansen and Anderko, 1958] and a Mo concentration of 8.8 wt.% Mo (the $[Mo]_{eq}$ of Ti-5553). Figure 3.24 shows a plot of the calculated α parameters for Mo, V, Cr, and Al. The diffusivities of Mo, V, Cr, Al, and Fe were calculated at T=1700°C, the approximate liquidus temperature, using activation energies and pre-exponentials given by Gale and Totemeier [Gale and Totemeier, 2004].

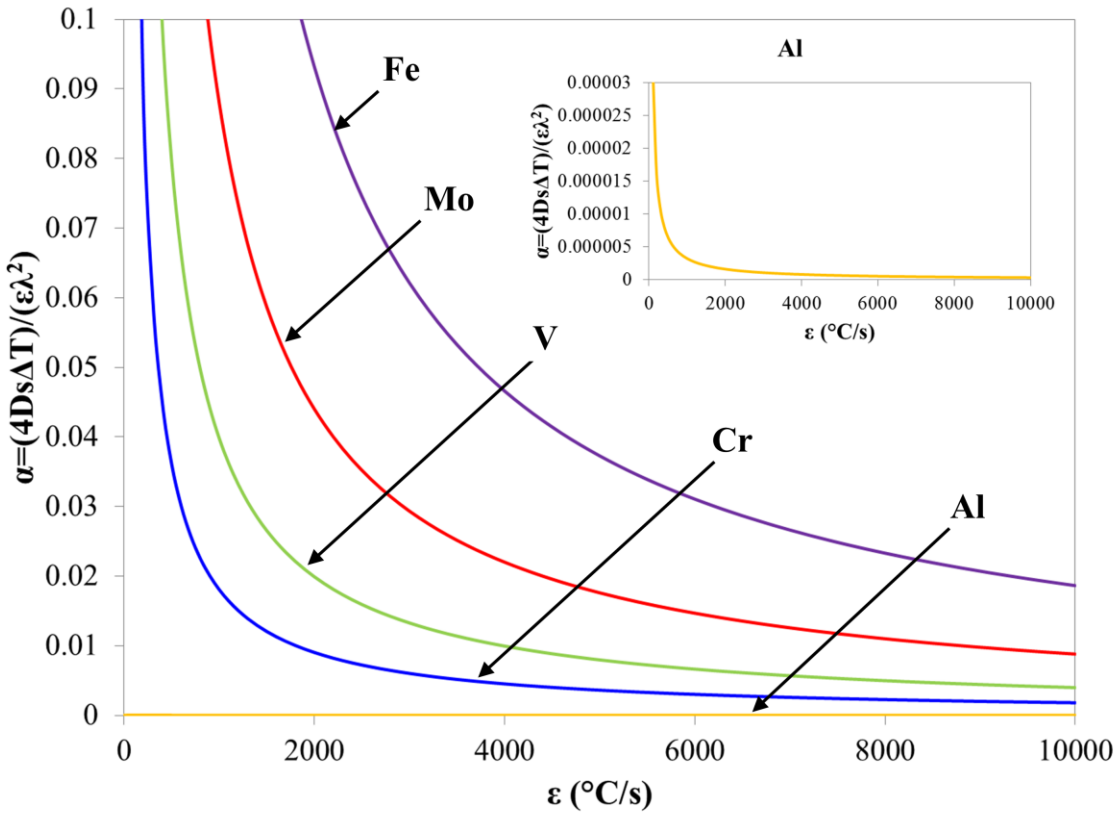

Figure 3.24. Dimensionless α parameter as a function of cooling rate for the main alloying elements in Ti-5553.

As seen in Figure 3.24, the α parameters are all well below 1, particularly at faster cooling rates. The smaller α is for a given cooling rate, the less significant is solid state diffusion. This can be seen in the Brody-Flemmings equation (Eq. 3.7).

$$C_s = kC_o\left(1 - \frac{f_s}{1+\alpha k}\right)^{k-1} \qquad \text{Eq. 3.7}$$

When $\alpha<<1$, or approximately 0, the Brody-Flemmings equation reduces to the Scheil equation (Eq 3.3). In this work, the use of the Scheil equation for the assumption of negligible diffusion in the solid can be justified once the cooling rate is known.

Using SmartWeld, a program developed by Eisler and Feurschbach [Eisler et al., 1997] at Sandia Nation Laboratories, the heat flow during EBW of Ti-5553 will be simulated. SmartWeld uses Rosenthal's equation [Rosenthal, 1941] (Eq. 3.8) to calculate the temperature distribution based on welding parameters such as, power, travel speed, and plate thickness.

$$\frac{2\pi(T-T_o)kg}{Q} = \exp\left(\frac{Vx}{2\alpha}\right) K_o\left(\frac{Vr}{2\alpha}\right) \qquad \text{Eq. 3.8}$$

Where T is the temperature, T_o is the workpiece temperature before welding, k is the thermal conductivity of the material, g is the material thickness, Q is the heat transferred to the workpiece, α is the thermal diffusivity ($\alpha=k/(\rho C_s)$), K_o is the modified Bessel function, and r is the radial distance from the origin. The benefits of using this SmartWeld are that it is quick, calculates relatively accurate peak temperatures and sizes of the HAZ and BM, and covers a variety of materials. Rosenthal's equations for heat flow, however, assume steady-state heat flow, a point heat source, negligible heat of fusion, constant thermal properties, no heat loss from the workpiece surface, and no convection in the weld pool. These assumptions make the analytical solutions useful for developing test parameters, verifying welding routines and predicting the size and shape of FZs and HAZ. The analytical soulutions, however, should be used with caution when operating under non-equilibrium (i.e. non-steady-state) conditions due to phase transformation kinetics that are not taken into account under steady-state conditions.

SmartWeld's material database is limited to only Ti-6Al-4V, with respect to Ti and Ti-alloys. Therefore, in order to validate the use of Ti-6Al-4V's thermal properties in place of those for Ti-5553, the specific heat (C_s) for multiple β-Ti alloys and Ti-6Al-4V were plotted as a function of temperature (Figure 3.25). Values of C_s for Ti-5553 have not been reported and are not available. For this reason, values of C_s for VT22 and Beta 21 were used as comparisons to

Ti-6-4. Good agreement between C_s for the two β-Ti alloys, VT22 and Beta 21, and Ti-6Al-4V can be seen in Figure 3.25, suggesting that C_s is similar for various Ti alloys. The C_s for VT22 agrees particularly well with that of Ti-6Al-4V, which is important since Ti-5553 was derived from VT22. Because of this, it can be assumed that the heat distribution calculated by SmartWeld for Ti-6-4 is also valid for Ti-5553.

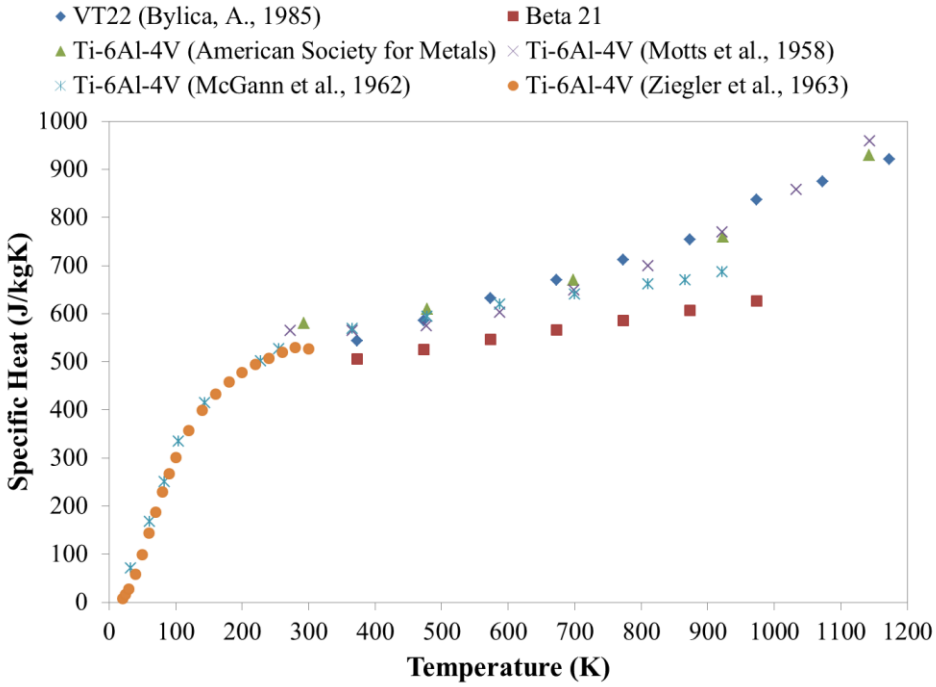

Figure 3.25. A comparison of specific heat as a function of temperature for VT22, Beta 21, and Ti-6Al-4V.

Despite of some of the short comings of Rosenthal's equations and SmartWeld's limited material database for Ti and Ti alloys, SmartWeld provided sufficient information regarding temperature distribution. Based on input of material thickness (1.6 mm), power (450 W), travel speed (8.5 mm/s), and workpiece temperature (23°C), SmartWeld calculated the peak temperature as a function of time. From it, a reliable approximation of the FZ cooling rate in EBW Ti-5553 was determined to be 5399°C/s. This cooling rate agrees with those reported for EBW by Debroy et al. [DebRoy et al., 1995], Munitz et al. [Munitz et al. 2000], Vishwakarma et al. [Vishwakarma et al., 2008], and Wu [Wu, 1981]. Using this cooling rate, it can be determined

from Figure 3.24 that the α parameter is much smaller than 1 for Mo, V, Cr, and Al and Fe. It is therefore safe to assume that diffusion in the solid is negligible and the Scheil equation is valid for assessing solute partitioning in EBW Ti-5553.

Figure 3.26 shows the results of the Scheil analysis where the concentrations of Mo, V, Cr, Al, and Fe are plotted against the fraction solid. The plots are in good agreement with the experimental concentration profiles in Figure 3.22. At f_s=0, the Scheil results indicate that the dendrite core will be enriched in Mo and Al and depleted of V, Cr, and Fe. At f_s=1, the Scheil results predict that the interdendritic regions are enriched in V, Cr, and Fe and depleted of Mo and Al. However, the Scheil results over- and underestimate the compositions at 0 and 1 fraction solid. This is the case, because the Scheil equations do not account for the diffusivities of the alloying elements, solidification time, or the interaction one solute elements with other solute elements. It assumes that the partition coefficient embodies these effects. Bermingham et al. [Bermingham et al. 2009], in their work on cast Ti-Cr alloys that retained β upon cooling with Cr contents of 6 wt.% and greater, showed that the concentrations predicted by the Scheil equation reasonably modeled solute segregation during solidification. However, they also showed the Scheil equations over- and underestimated the concentrations at the dendrite cores and interdendritic regions, respectively.

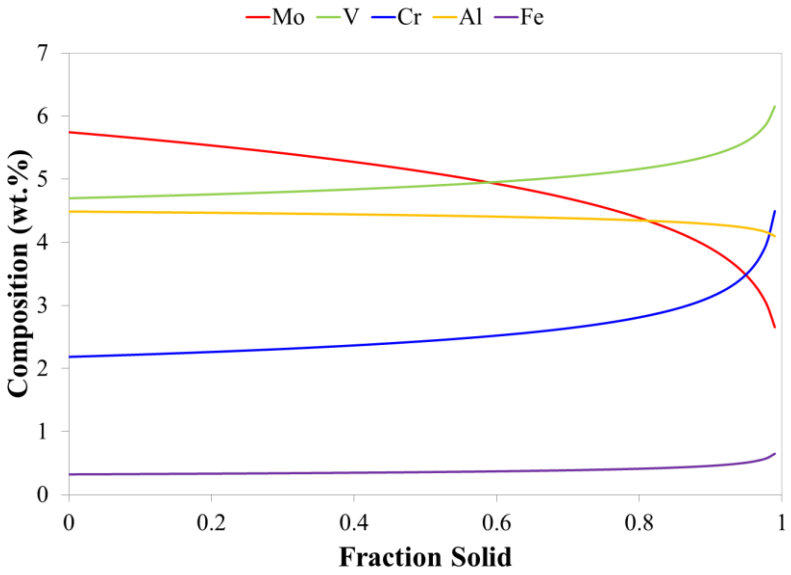

Figure 3.26. A plot of composition versus fraction solid based on the Scheil calculations for solute partitioning during solidification in the FZ of EBW Ti-5553.

3.3.2. Effects of PWHTs on Homogenization

The aging treatments precipitated α to strengthen the retained β-phase in the WZs of EBW Ti-5553. However, after aging, cellular dendrites were still visible within the FZs using BSE imaging. This indicated that the PWHTs were not adequate treatments with which to homogenize the FZs in EBW Ti-5553. As shown in Figures 3.27–3.29, segregation is still pronounced in the BSE images and in the concentration profiles across the cellular dendrites. The main reason for limited homogenization is the fact that the PWHTs were designed as precipitation hardening treatments. Since the FZs and HAZs were comprised of retained β in the AW condition, the effect of precipitation strengthening on the FZ was of importance. A true homogenization treatment above the β-transus would successfully homogenize the FZ, but perhaps at the expense of grain growth. Depending on the amount of residual stress/strain remaining in the grains after welding and varied grain size throughout the HAZs and FZs, recovery, recrystallization, and grain growth may occur at different rates and temperatures throughout the WZ during a homogenization treatment. In the AW condition, EBW Ti-5553 retained a fully β microstructure within the FZ and HAZs, which has the equivalent effect of

solutionizing the AW specimens. The equiaxed grains within the HAZ are indications that recovery, recrystallization, and grain growth already took place and occurred at different rates based on the grain sizes near the BM (temperatures closer to the β-transus) and FZ (temperatures closer to the melting point). Exposing the WZ to temperatures above the β-transus may result in excessive grain growth if homogenization times are long and could adversely affect mechanical properties in the WZ according to the Hall-Petch equation. Therefore, only aging treatments at sub-transus temperatures were carried out.

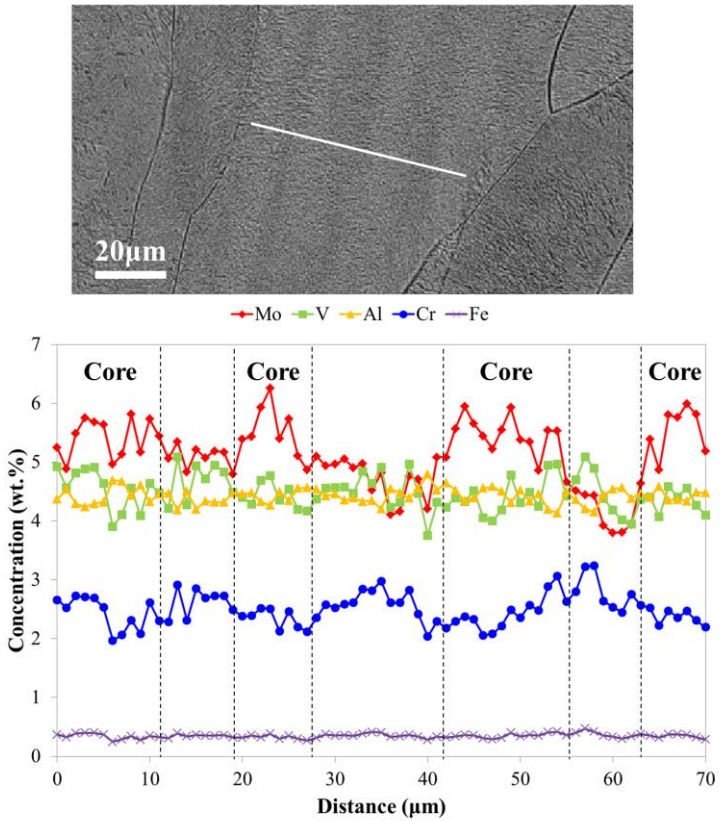

Figure 3.27. Backscatter secondary electron image of cellular dendrites in the FZ of an EBW Ti-5553 specimen heat treated at 700°C/4h (top) and the corresponding concentration profiles of alloying elements across the cellular dendrites generated by EPMA (bottom). The white line in the backscatter image designates the location from which the concentration profiles were acquired.

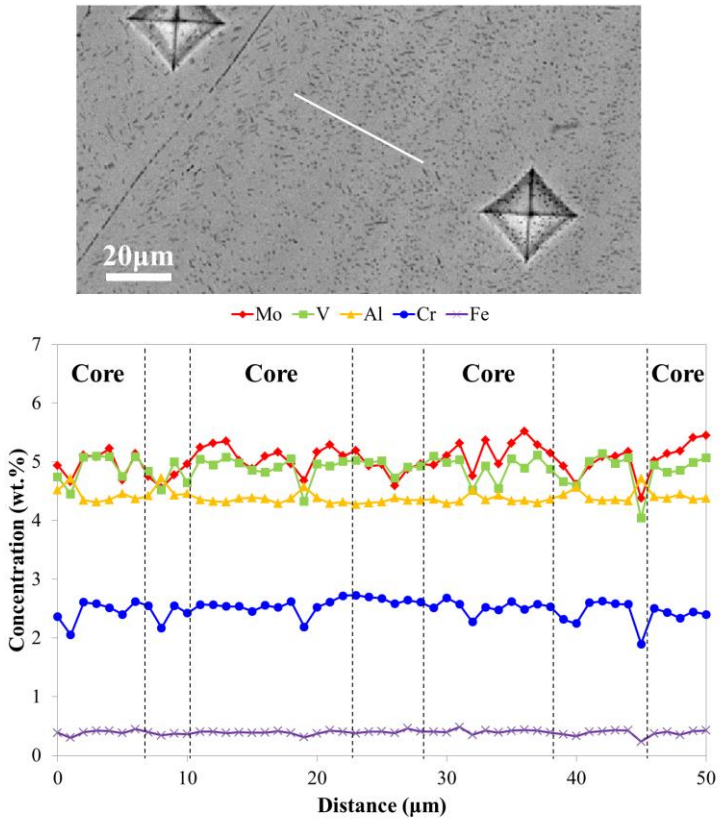

Figure 3.28. Backscatter secondary electron image of cellular dendrites in the FZ of an EBW Ti-5553 specimen heat treated at 804°C/1h (top) and the corresponding concentration profiles of alloying elements across the cellular dendrites generated by EPMA (bottom). The white line in the backscatter image designates the location from which the concentration profiles were acquired.

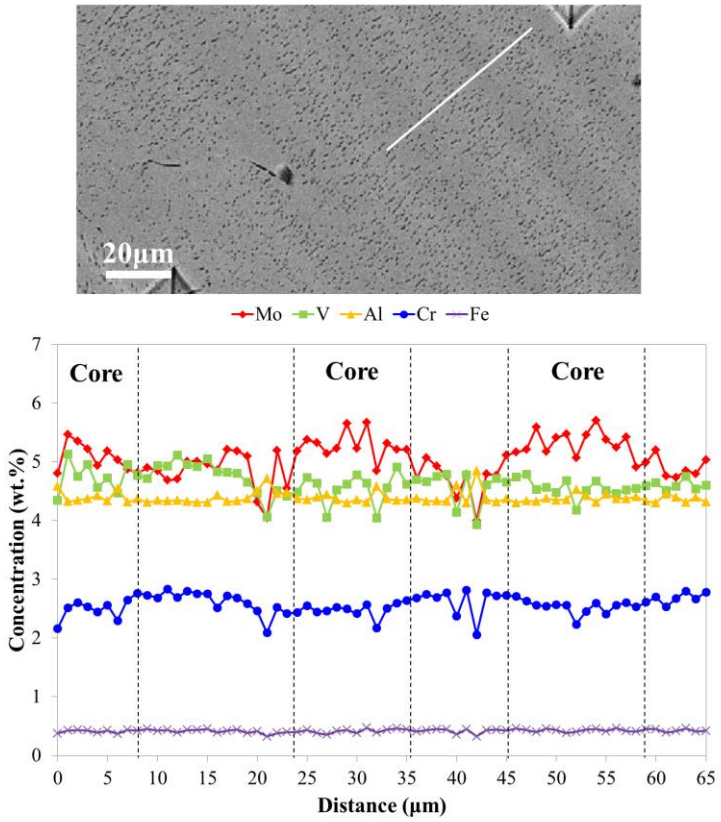

Figure 3.29. Backscatter secondary electron image of cellular dendrites in the FZ of an EBW Ti-5553 specimen heat treated at 804°C/1h followed by aging at 600°C/4h (top) and the corresponding concentration profiles of alloying elements across the cellular dendrites generated by EPMA (bottom). The white line in the backscatter image designates the location from which the concentration profiles were acquired.

In order to better understand the effects of the PWHTs on homogenization of the FZ in EBW Ti-5553, the index of residual segregation for was calculated. The index of residual segregation, δ, is useful for estimating the PWHT times and temperatures required for effective homogenization [DuPont, Lippold, and Kiser, 2009]. δ can be defined in terms of experimentally determined compositions and as a function of time, diffusivity, and dendrite arm spacing as given in equations 3.9 and 3.10.

$$\delta = \frac{C_M - C_m}{C_M^o - C_m^o} \qquad \text{Eq. 3.9}$$

$$\delta = exp\left(-\frac{4\pi^2 Dt}{\lambda^2}\right) \qquad \text{Eq. 3.10}$$

Where C_M and C_m are the maximum and minimum concentrations that exist at the interdendritic region and dendrite core after some time at the PWHT temperature, respectively. C^o_M amd C^o_m are the initial concentrations that exist in the same regions prior to homogenization. D is the diffusivity of a particular solute element in the matrix, t is the PWHT time in seconds, and λ is the dendrite arm spacing (measured to be 14.10±1.89 μm) . In both cases, δ is initially 1 at the start of homogenization and decreases to zero as the concentration gradient relaxes. Ideally, δ should be zero at the end of a homogenization treatment, but it is generally accepted that when δ reaches values below 0.1 the FZ is considered to be homogenized [DuPont et al., 2011].

Typically, the slowest diffusing element dictates the PWHT time and temperature, because it will take the longest to reduce its concentration gradient from the dendrite core to the interdendritic region. In Ti and Ti-alloys, Mo is the slowest diffusing element in the system, which can be seen in Figure 3.30. Therefore, experimental data obtained from EPMA profiles across the cellular dendrites in the FZ of EBW Ti-5553 for Mo will be used in determining δ and analyzing the effects of the PWHTs on homogenization of the FZ. δ was determined using equation 3.9 for the PWHT temperatures of 700°C, 804°C, and 600°C. It was found that the indexes of residual segregation for Mo at 700°C/4, 804°C/1h, and 600°/4h (for 600°C, C^o_M and C^o_m were taken as C_M and C_m from the specimens heat treated at 804°C) were, 0.955, 0.418, and ~1, respectively. From these values of δ for Mo at 700°C and 804°C, effective diffusivities were calculated using equation 3.10, from which the relation between δ and PHWT time was plotted (Figure 3.31). A plot of δ for Mo at 600°C was not included, because δ was approximately 1, meaning the aging treatment at 600°C/4h had negligible effects on the remaining concentration gradient from the previous heat treatment. Figure 3.31 shows that the two heat treatments could not effectively homogenize the FZ.

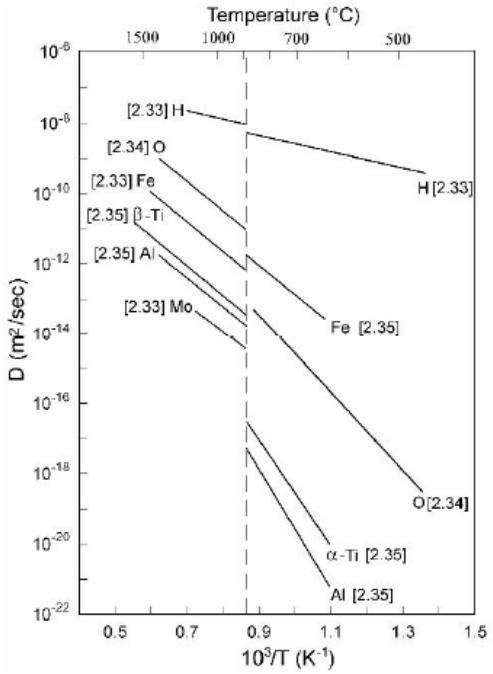

Figure 3.30. Arrhenius diagram of Ti self-diffusion and diffusion of selected alloying elements in the β and α phases. The dashed line represents the β-transus of pure Ti (882°C) [Lütjering and Williams, 2007].

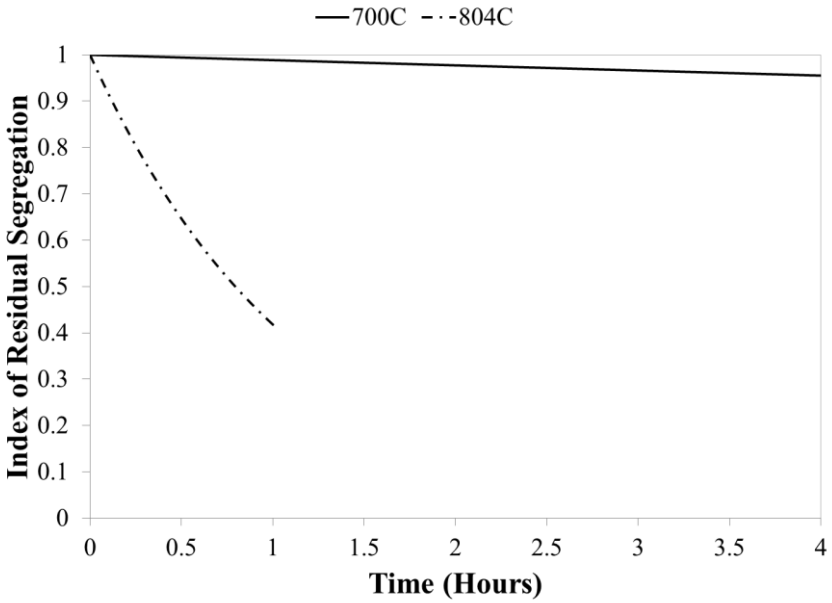

Figure 3.31. A plot of the index of residual segregation, δ, versus time for PWHT temperatures and times of 700°C for 4 hours and 804°C for 1 hour. Data for 600°C for 4 hours is not shown because δ was approximately 1, meaning no homogenization occurred.

Even though the PWHTs provided insufficient homogenization at the given temperatures and times, the PHWT at 804°C/1h did provide some homogenization (δ=0.418). If the PWHT

were longer, homogenization is possible in EBW Ti-5553 at 804°C. Figure 3.32 is the same plot as in Figure 3.31 for the PWHT at 804°C/1h, but extrapolated out to 3 hours. In approximately 2.9 hours, homogenization ($\delta<0.1$) is achieved at 804°C. 2.9 hours is not unpractical, but heat treatments below the β-transus in any Ti-alloy promotes precipitation of a second phase. As seen in EBW Ti-5553 specimens heat treated at 804°C/1h, coarse α precipitates form within 1 hour. Holding any longer at this temperature would subsequently coarsen these particles and impart little strength to the FZ.

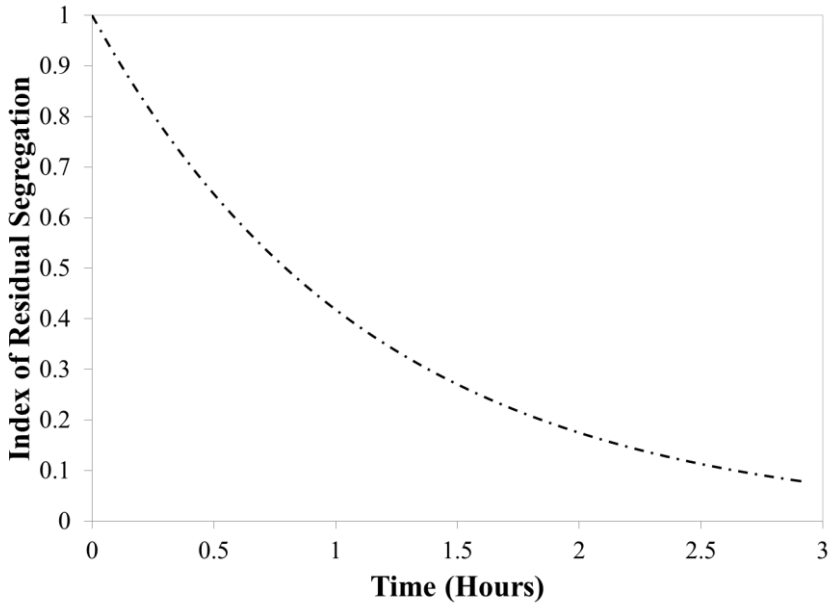

Figure 3.32. Extrapolated plot of δ for Mo out to 3 hours for a PWHT temperature of 804°C. An acceptable degree of homogenization (δ<0.1) is achieved in approximately 2.9 hours.

For true homogenization to take place in EBW Ti-5553, heat treatments must be conducted above 856°C in the single phase, β regime. At temperatures above the β-transus diffusion should be orders of magnitude higher for some elements (Figure, 3.30), making homogenization easier and ultimately faster. Figure 3.33 shows theoretical homogenization temperatures and times for EBW Ti-5553 if a heat treatment were to be conducted at or above 856°C. As the temperature increases, the time at which homogenization is complete ($\delta<0.1$) decreases significantly. Compared to the PHWT for 1 hour at 804°C, a heat treatment at 856°C

results in complete homogenization in approximately 37 minutes. Because the results plotted here are for this specific EBW process, they don't necessarily represent what would actually happen in practice. Part size, dendrite arm spacing, and heating rate would play significant roles in how a component responded to a homogenization treatment. For example, a casting 10 cm in diameter and 10 cm tall and a 2 mm thick EBW sheet whose FZ measured 1.5 mm across, would not be homogenized in the same amount of time even for a similar dendrite arm spacing and identical heat treatment schedule.

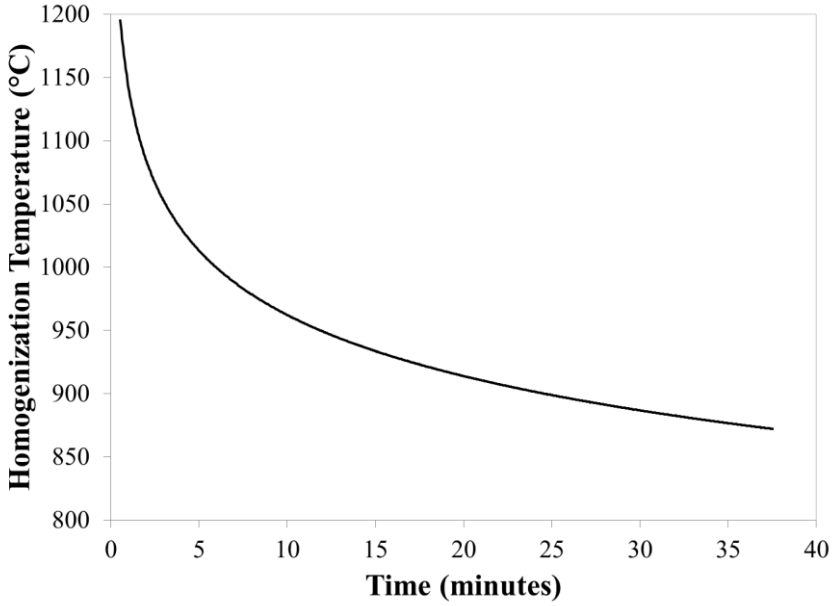

Figure 3.33. Theoretical homogenization temperatures versus homogenization times for PHWTs performed above the β-transus (856°C) for EBW Ti-5553.

The PWHTs used in this investigation of EBW Ti-5553 make relatively poor homogenization treatments, because they were designed as precipitation treatments. Some relaxation of the concentration gradient across the cellular dentrites in the FZs does occur, but it is superseded by precipitation. At temperatures below the β-transus, i.e. within the α+β regime, alloying elements are still able to diffuse down concentration gradients, albeit slowly over long distances. However, it is more favorable to precipitate a second phase instead of reducing the

concentration gradient, hence the ineffectiveness of the PWHTs to homogenize the FZ in EBW Ti-5553.

3.3.3. Section 3.3 Summary

As a result of solidification, cellular dendrites formed within the FZ of EBW Ti-5553. Their formation indicates the breakdown of planar solid/liquid interfaced due to constitutional supercooling. Subsequently, solute segregation across the interface occurred leaving dendrite cores enriched in Mo and Al and interdendritic regions enriched in V, Cr, and Fe. Scheil approximations agreed relatively well with the experimentally acquired composition profiles across the cellular dendrites. The Scheil approximations, however, slightly over- and underestimated the dendrite core and interdendritic compositions compared to the experimental compositions. Even though the PWHTs were not homogenization treatments, heat treating at 804°C for 1 hour did relax the concentration gradient by approximately 58% across the dendrites to some degree, while heat treating at 700°C for 4 hours and at 600°C for 4 hours had negligible effects on homogenization. Overall, the PWHTs were poor homogenization treatments due to the fact they were implemented to provide precipitation strengthening. For complete homogenization in a practical time and without causing excessive grain growth, heat treatment must be carried out above the β-transus of Ti-5553.

3.4. Identification of Precipitates within the Fusion Zone

Observation using LOM and SEM techniques showed that no precipitates of resolvable size existed in the specimens in the AW condition. The same techniques evidenced precipitates taking on typical morphologies of α precipitates at grain boundaries and within grains in the PWHT specimens. Images of these precipitates can be seen in Figures 3.11 – 3.16. However, it is possible that ω may be present as athermal ω or isothermal ω in each condition (AW or PWHT). Athermal ω is more likely to be present in the AW specimens, because of its tendency

to form upon cooling from above the β-transus in metastable β-Ti alloys, whereas isothermal ω is likely to be present in the PWHT, because of its formation during relatively low temperature heat treatments and heating. ω does go back into solution upon holding at temperatures between 400°C-550°C [Donachie, 2000] and at higher temperatures within the α+β regime for sufficient durations. In some instances [Azimzadeh et al., 1998; Omhori et al., 1998; Williams et al., 1969; Prima et al, 2006; Nag et al., Acta Mater., 2009] ω acts as a precursor for the precipitation of α instead. Because the crystal structures of athermal ω (trigonal) and isothermal ω (hexagonal) are relatively similar and have the same lattice parameters (a=0.460 nm and c=0.282 nm) [Silcock, 1956; Bagariatski, et al. 1959] their diffraction patterns are difficult to separate and differentiation of the two can typically only be made by knowing the processing schedules of the material, in which they were observed. α, on the other hand, is readily identifiable due to its expected precipitation in metastable β-Ti alloys as well as its typical macroscopic morphology at grain boundaries and as plates.

In order to confirm the identities of precipitates present within the FZs of EBW Ti-5553 in the AW and PWHT conditions, transmission electron microscopy was employed. Of particular interest, were the $[113]_\beta$ and $[001]_\beta$ zone axes in metastable β-Ti alloys and Ti-5553, which are known to contain superlattice reflections from ω and α, respectively. Other zone axes, such as the $[111]_\beta$, $[110]_\beta$, and $[112]_\beta$, are also known to contain reflections for these phases in the diffraction patterns. However, due to the orientation of the grains within the FZ (approximately parallel to the $\{001\}_\beta$ direction, FIB specimens containing those zone axes were difficult to obtain without complex FIB procedures. To identify the precipitates, specimens were oriented along either the $[113]_\beta$ or $[001]_\beta$ zone axes or along both zone axes to best show the ω- and α-phases. Selected area diffraction (SAD) patterns and dark field (DF) images were then acquired. Figures 3.34 through 3.37 show the SAD patterns and corresponding DF images for specimens in the AW and PWHT conditions.

3.4.1. α

From light optical and scanning electron microscopy α was observed to precipitate in the FZ as intragranular platelets and at β grain boundaries only in the PWHT specimens as described in section 3.2. Even though the identification of α was accomplished through light optical and scanning electron techniques, it was based on comparative observations of the morphology, size, and location of α as well as prior knowledge of α forming in β-Ti alloys upon heat treatment. Therefore, unequivocal confirmation of its identity is needed. To do this, TEM techniques were employed and specimens were oriented relative to the beam directions such that the $\langle 11\bar{2}0\rangle_\alpha // \langle 100\rangle_\beta$ OR was met. SAD patterns and DF images were collected for the specimen containing α.

In every specimen, excluding those in the AW condition, the $[100]_\beta$ zone axis pattern displayed indications of the presence of α. Figures 3.34 through 3.36 show the $[100]_\beta$ zone axis patterns and DF images of the α precipitates in specimens heat-treated at 700°C/4h at 804°C/1h, and at 804°C/1h followed by aging at 600°C/4h. These zone axis patterns contained either superlattice reflections from the $[1120]_\alpha$ zone or lattice streaking. The latter, as seen in Figure 3.35a for the specimens heat-treated at 804°C/1h, suggests that extremely fine α particles are present, but not yet fully developed, which supports the theories that α precipitates from ω precursors (section 3.4.2. describes the presence of ω in these specimens) [Azimzadeh et al., 1998; Omhori et al., 1998; Williams et al., 1969; Prima et al, 2006; Nag et al., 2009b].

Specimens heat-treated at 700°C/4h and at 804°C/1h followed by aging at 600°C/4h exhibited distinct superlattice reflections caused by α (Figures 3.34a and 3.36a). Many of the reflections appear to be satellite reflections around the $\{200\}_\beta$ and $\{110\}_\beta$ type reflections. This is particularly evident in Figure 3.36a, in which 4 reflections of discrete intensity surround the β reflections. In specimens heat-treated at 700°C/4h superlattice reflections are present as only one variant, α1 (red squares), as shown in Figure 3.34b, whereas two variants, α1 and α2 (red squares and circles, respectively), are present in specimens heat treated at 804°C/1h followed by aging at

600°C/4h (Figure 3.36b). Figure 3.37a-d show DF images using four of the present $\{1011\}_{\alpha 2}$ reflections. It is clearly evident from this that the α-phase does not nucleate and grow at random, but rather it obeys ORs. It is interesting to point out that the $[100]_{\beta}$ zone axis pattern in Figure 3.36a somewhat resembles the start of a ring diffraction pattern, wherein equivalent reflections, due to various crystallographic orientations, lie on concentric circles/rings about the central spot.

The superlattice reflections surrounding the β reflections, as well as those located between the 000 and $\{110\}_{\beta}$ type reflections and those between the $\{200\}_{\beta}$ and $\{110\}_{\beta}$ type reflections, are consistent with the α-phase superlattice reflections reported by Rhodes et al. [Rhodes et al., 1975] in their work on the precipitation of α in metastable β-Ti alloys. They found similar satellite reflections around the $\{200\}_{\beta}$ and $\{110\}_{\beta}$ type reflections as well as in between the 000 and $\{110\}_{\beta}$ type reflections. The reflections surrounding the $\{200\}_{\beta}$ and $\{110\}_{\beta}$ type reflections, were termed as "flankers." Some of the reflections, particularly the flankers around the $\{110\}_{\beta}$ reflections, were seen to be concentrically arced around the central spot, but did not occur in the Burgers OR [Rhodes et al., 1975].

They put forth that all of the superlattice reflections caused by the $[1120]_{\alpha}$ zone in the $[100]_{\beta}$ zone axis pattern are a result of precipitates that are extended in the direction of the electron beam whose reciprocal lattice points intersect the Ewald sphere [Rhodes et al., 1975]. Approximate rotations of 15° of a Burgers oriented α about the normal to a $\{41\bar{1}0\}_{\alpha}$ plane resulted in simulated diffraction patterns of the $[100]_{\beta}$ containing reflections identical to those observed in the $[100]_{\beta}$ zone axis patterns from experimental work, which was cited as the cause of the observed reflections [Rhodes et al., 1975].

Similar $[100]_{\beta}$ zone axis patterns were obtained for EBW Ti-5553 specimens heat-treated at 804°C/1h followed by aging at 600°C/4h, however a set of two $\{0001\}_{\alpha 2}$ type reflections are present, where only one is present in the patterns reported by Rhodes et al. This

may be a result of rotation about another α plane normal, which affects the α2 variants more than the α1 variants. In any case, multiple variants of α-phase are present.

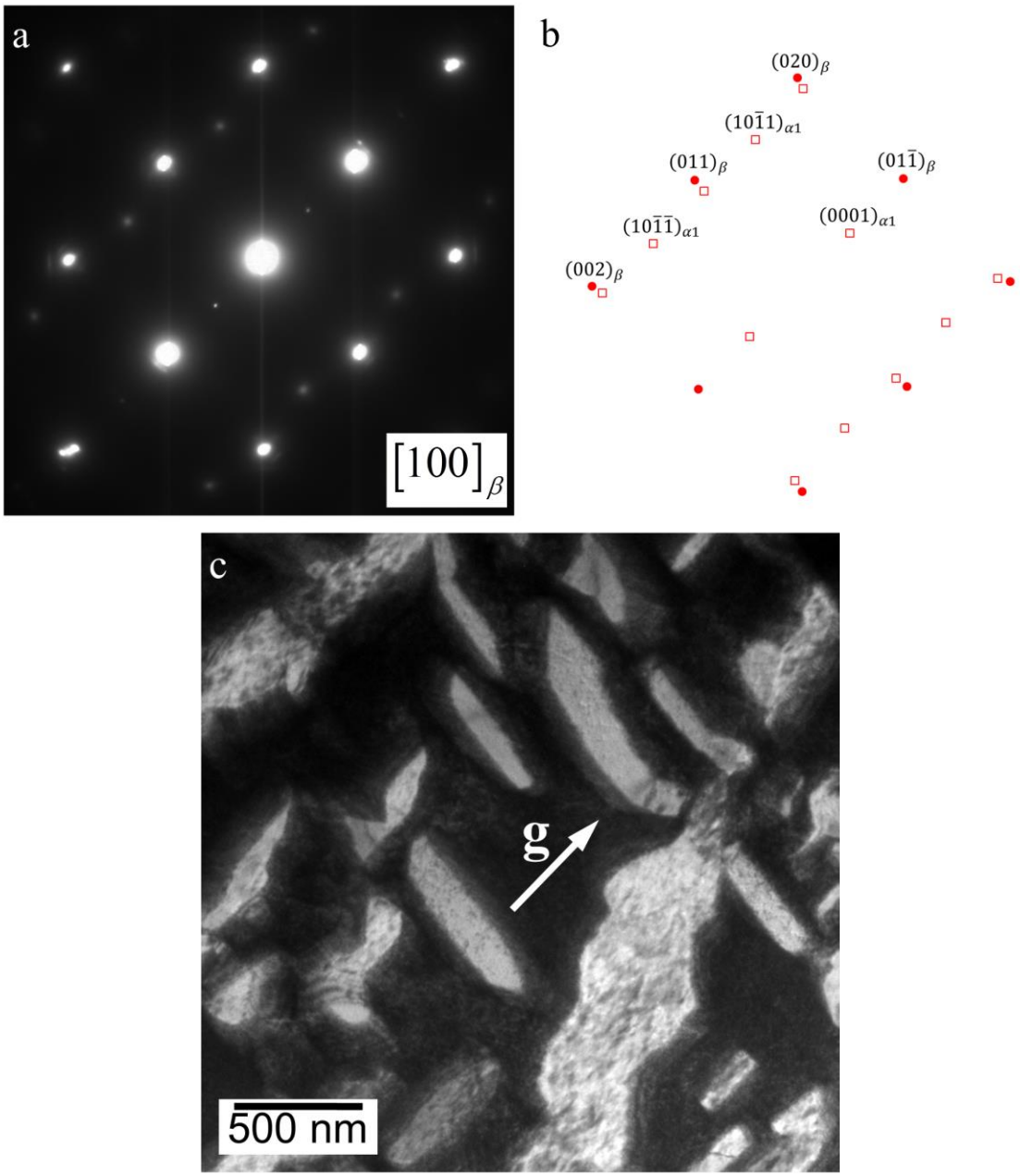

Figure 3.34. (a) SAD pattern of the $[100]_\beta$ *zone axis, (b) indexed schematic of (a), and (c) the accompanying* 0001_α *DF image from the FZ of a specimen heat treated at 700°C/4 hours. The indices in red boxes correspond to the α-phase.*

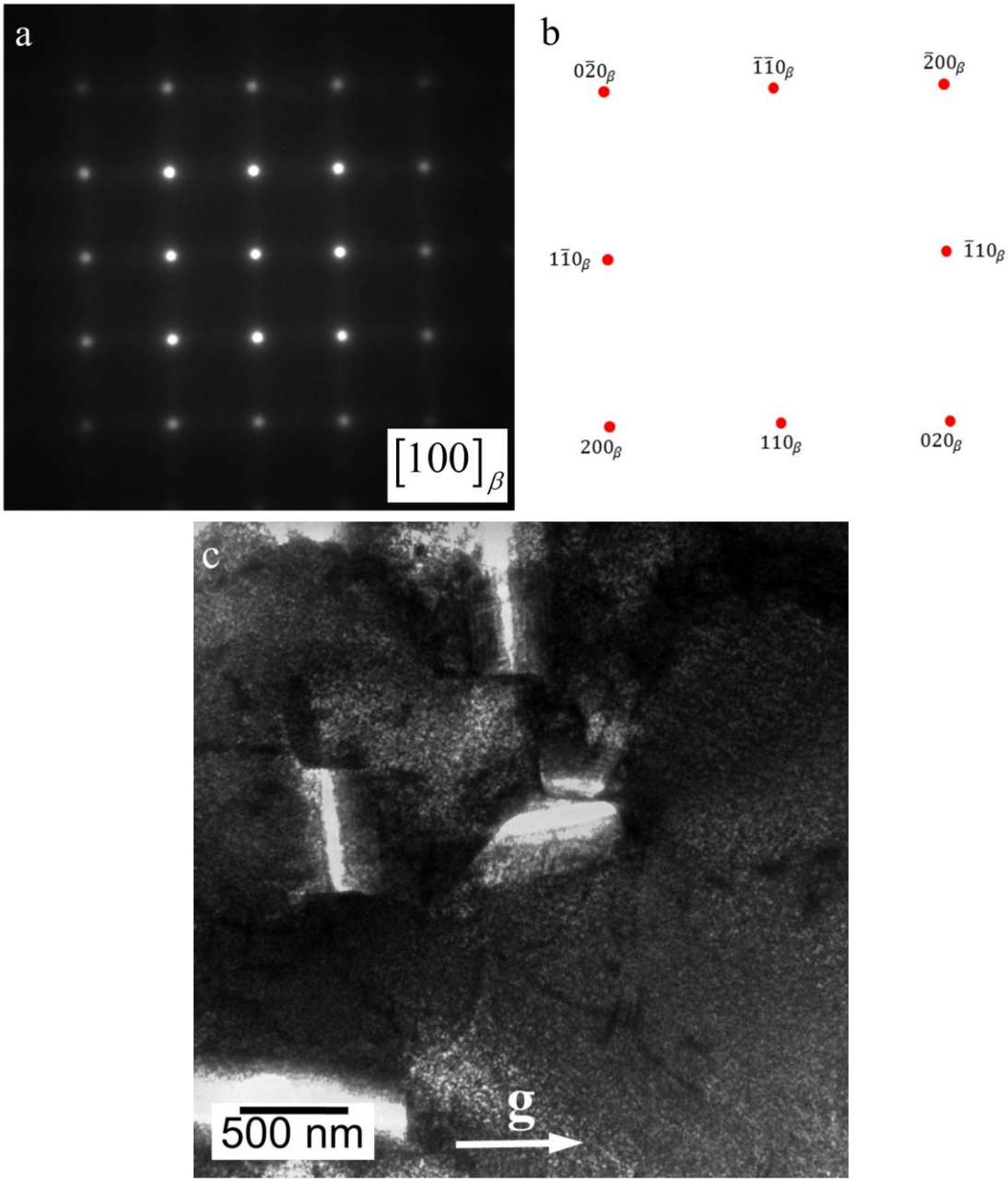

Figure 3.35. (a) SAD pattern of the $[100]_\beta$ *zone axis, (b) an enlarged schematic of (a), and (c) the accompanying* 0001_α *DF image from the FZ of a specimen heat treated at 804°C/1 hour. The indices in red boxes correspond to the α-phase.*

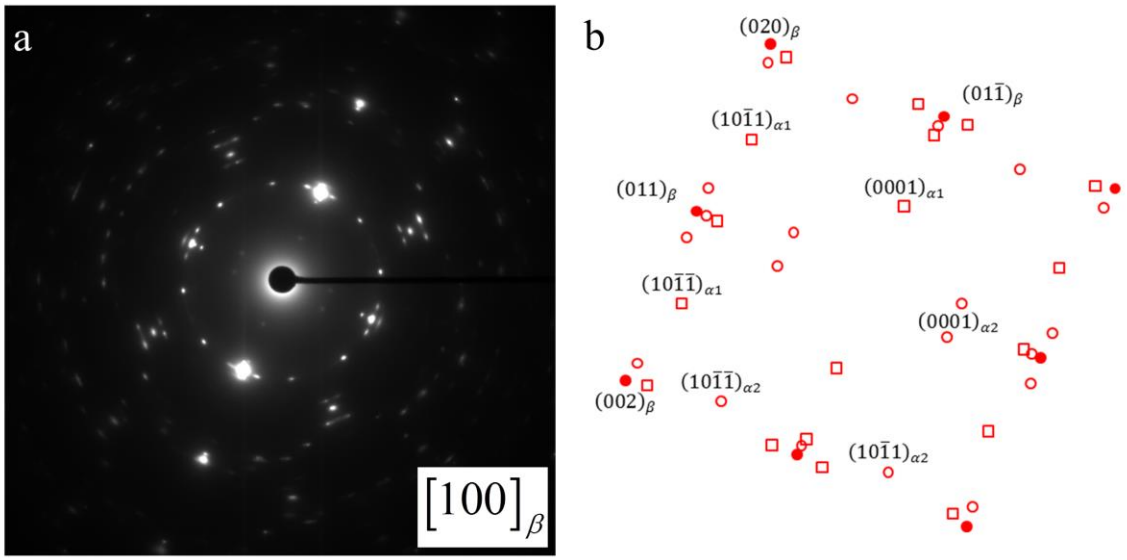

Figure 3.36. (a) SAD pattern of the $[100]_\beta$ zone axis and (b) an enlarged schematic of (a) from the FZ of a specimen heat treated at 804°C/1h followed by aging at 600°C/4h. The indices in red boxes and circles correspond to the α1 and α2 variants, respectively.

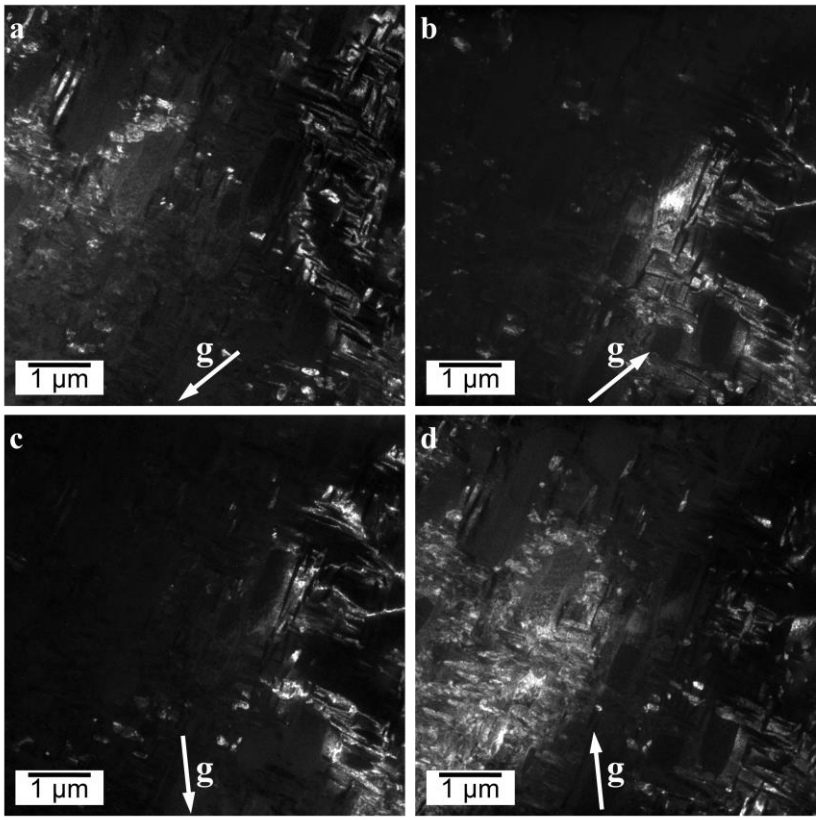

Figure 3.37. DF images from the FZ of specimens heat treated at 804°C/1h followed by aging at 600°C/4h acquired using the (a) $10\bar{1}\bar{1}_{\alpha 2}$ reflection, (b) $\bar{1}0\bar{1}\bar{1}_{\alpha 2}$ reflection, (c) $10\bar{1}1_{\alpha 2}$ reflection, and (d) $\bar{1}0\bar{1}1_{\alpha 2}$ reflection.

3.4.2. ω

In the AW condition superlattice reflections were present at $1/3(211)_\beta$ and $2/3(211)_\beta$. These reflections correspond to the ω-phase and have been indexed as shown in Figure 3.38a-b. The $[113]_\beta$ zone axis pattern acquired from the FZ in the AW specimens is very similar to the $[113]_\beta$ zone axis patterns reported for binary β-Ti systems as well as Ti-5553, which contain ω precipitates [Harper, 2004; Nag et al., 2009]. According to Silcock et al. [Silcock et al., 1958] the OR for ω and β is $(0001)_\omega // (\bar{1}11)_\beta$ and $\langle 11\bar{2}0\rangle_\omega // \langle 1\bar{1}0\rangle_\beta$, of which the latter is most relevant in this investigation. The indices determined for the reflections caused by the presence of ω are in agreement with Silcock et al.'s OR and the indices reported by Nag et al. [Nag, et al., 2008]. Because EBW produces a microstructure of retained β, it can be thought of as somewhat analogous to quenching to room temperature after solution treating above the β-transus. Drawing this analogy, one can confidently reason that ω should form in the FZ after solidification and during further cooling to room temperature. Cooling from above the β-transus of Ti-5553 (856°C) to room temperature has been shown to produce ω in Ti-5553 by Nag et al. [Nag et al., 2009], and Harper [Harper, 2004]. In Figure 3.38a and c, the SAD pattern and DF image verify that ω is present in the EBW Ti-5553 specimens in the AW condition. It is most likely present as athermal ω, because the EB weld was continuously cooled from above the β-transus to room temperature with no intermediate isothermal holds below the β-transus. An isothermal hold would have caused the athermal ω to transform to isothermal ω, or initiated the precipitation of α. It is possible, however, for athermal and isothermal ω to simultaneously exist, because athermal ω is the incomplete shuffle transformation of β to isothermal ω.

Using the OR determined by Silcock [Silcock, 1958], it is reasonable to explain the appearance of these reflections as the overlapping patterns of the $[113]_\beta$ zone axis and the $\langle 11\bar{2}0\rangle_\omega$ zone axis with its origin at the $\{110\}_\beta$ reflections of the $[113]_\beta$ zone axis pattern. This

produces spots at the 1/3 and 2/3 positions between the 000 and $\{211\}_\beta$ reflections when rotated approximately ±73° from the horizontal. This is in agreement with De Fontaine et al.'s work [De Fontaine et al., 1971] wherein the $\{211\}_\beta$ and $\{110\}_\beta$ reflections are zone normals for two of the four ω variants.

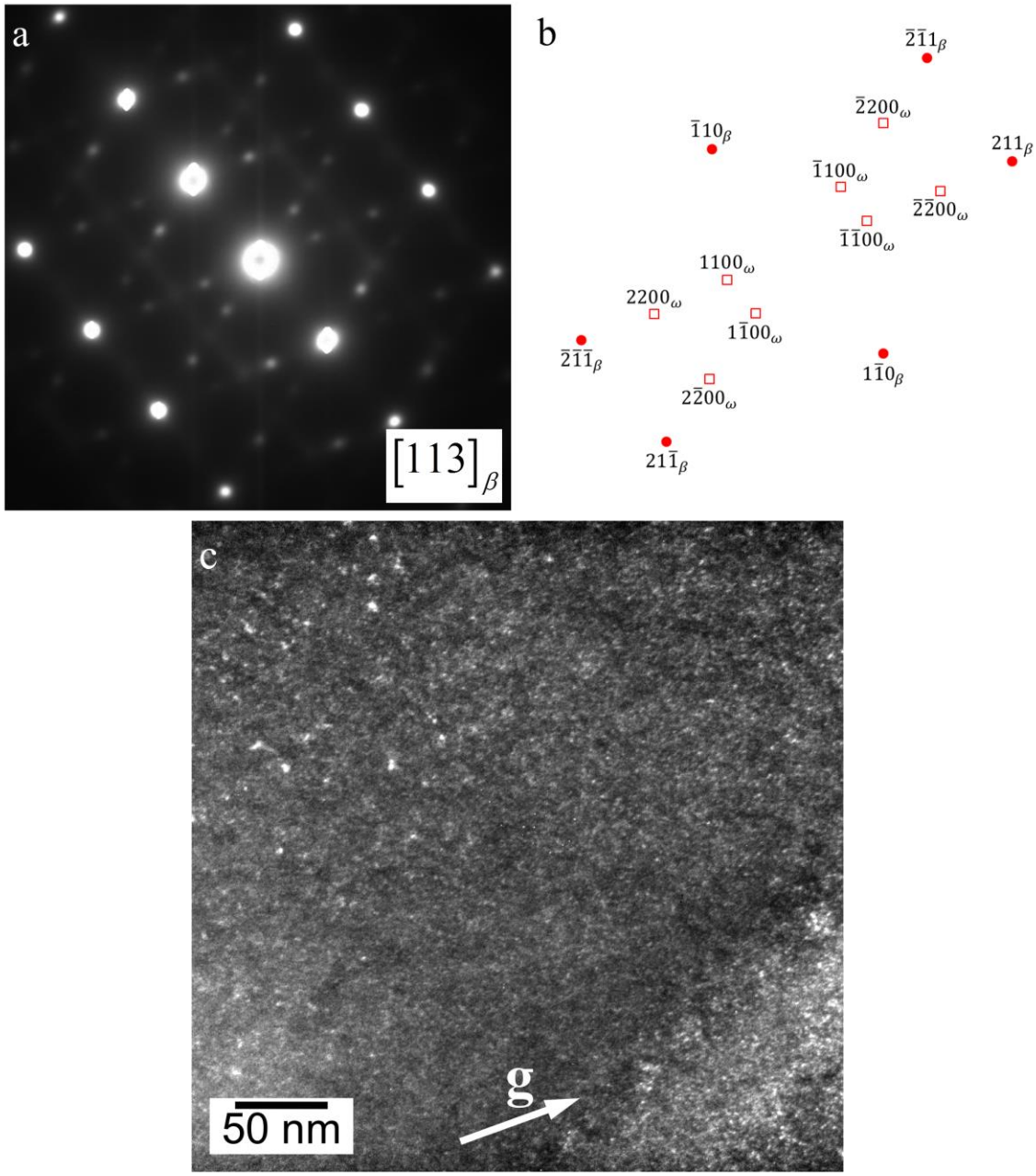

Figure 3.38. (a) SAD pattern of the $[113]_\beta$ *zone axis, (b) an enlarged schematic of (a) and (c) the accompanying* $\bar{1}\bar{1}00_w$ *DF image from the FZ of a specimen in the AW condition. The indices in red boxes correspond to the ω-phase.*

Reflections at $1/3(211)_\beta$ and $2/3(211)_\beta$ were also present in the $[113]_\beta$ zone axis patterns acquired from the FZ of specimens heat-treated at 804°C/1 hour (Figure 3.39). Their presence confirms that ω exists in these specimens as well. A DF image using the $\bar{1}\bar{1}00_\omega$ reflections revealed that the ω precipitates are slightly coarser than those in the specimens in the AW condition (Figure 3.39c). The coarsening may be attributed to exposure to elevated temperatures, at which the shuffle reaction from β to ω can achieve a more complete structure, i.e. athermal ω to isothermal ω (Figure 1.8). Once isothermal ω forms it may coarsen depending on temperature and time at temperature. Devaraj et al. [Devaraj et al., 2012] have seen this to occur in Ti-Mo alloys annealed at 475°C for 48 hours wherein the average ω precipitate size was reported to be approximately 80 μm. The transformation from athermal ω to isothermal ω may also account for the brighter ω superlattice reflections and more intense streaking in the SAD pattern (Figure 3.39) compared to the analogous SAD pattern acquired for specimens in the AW condition (Figure 3.38). Because the change from β to isothermal ω results in a continuum of intermediate transformations [De Fontaine, 1973], many stages of the transformation exist due to heating through the ω+β phase regime to 804°C, which give rise to the intense lattice streaking and more intense superlattice reflections. However, heating to 804°C and holding for 1 hour did not result in complete transformation of athermal ω to isothermal ω or cause the ω precipitates to disappear. This suggests that the heat treatment time was not sufficient to eliminate ω by dissolution into β or being consumed by the nucleation and growth of α. However, it is apparent from Figures 3.35 and 3.39 that α and ω exist simultaneously in the FZ of specimens heat treated at 804°C/1h, meaning that α did form either heterogeneously or homogeneously from ω.

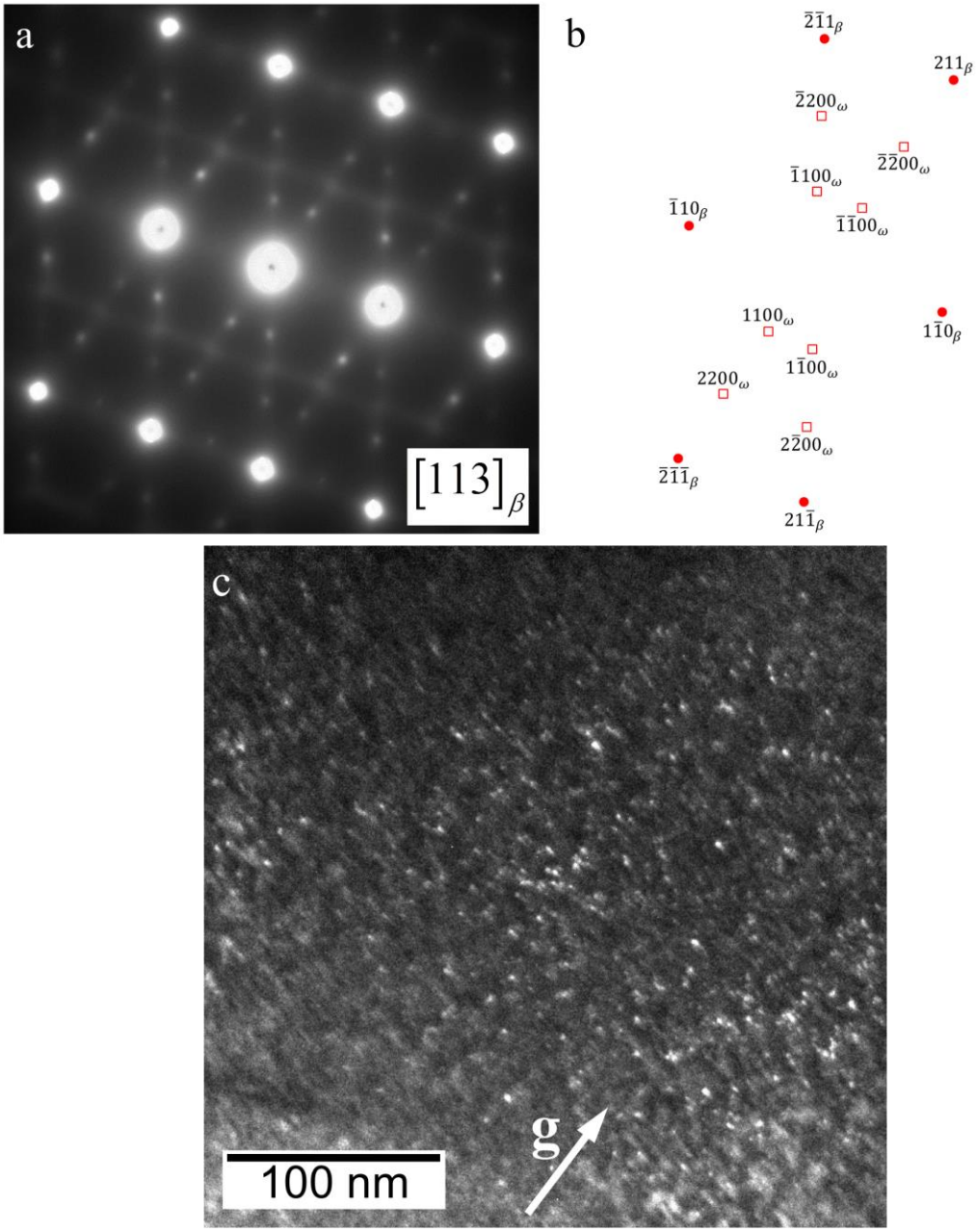

Figure 3.39. (a) SAD pattern of the $[113]_\beta$ *zone axis, (b) an enlarged schematic of (a) and (c) the accompanying* $\bar{1}\bar{1}00_w$ *DF image from the FZ of a specimen heat treated at 804°C/1 hour. The reflections in red boxes correspond to the ω-phase.*

Specimens heat-treated at 700°C/4h and at 804°C/1h followed by aging at 600°C/4h exhibited no indications of the ω-phase. Figures 3.40 and 3.41 show the $[113]_\beta$ SAD patterns acquired from the FZs of specimens heat-treated at 700°C/4h and specimens heat-treated at 804°C/1h followed by aging at 600°C/4h, in which no superlattice reflections exist. The absence

of the superlattice reflections for the ω variants suggests that ω dissolved and/or acted as a precursor for α during the heat treatments at 700°C and 600°C for 4 hours. During these two PWHTs, α precipitated as fine platelets, which were confirmed in the $[100]_{\beta}$ zone axis patterns and DF images in the previous section (3.4.1), and are indicative of α nucleation in the presence of ω. Authors, who have reported ω-assisted α precipitation, have seen similar results [Azimzadeh et al., 1998; Omhori et al., 1998; Williams et al., 1969; Prima et al, 2006; Nag et al., Acta Mater., 2009]. The disappearance of ω is said to transpire as a result of aging above the ω-solvus where α precipitation is favored. Depending on the time allotted for α precipitation, ω and α may be present simultaneously (shorter aging times) or only α will exist (longer aging times) as seen here in EBW Ti-5553 specimens subjected to 4 hour aging times. For β-Ti alloys in particular, systems comprised of α, ω, and β, or α and β, or ω and β may develop upon cooling to room temperature, but β alone has not yet been reported to exist without having ω and/or α precipitate.

In the specimens subjected to either of the two PWHTs wherein ω was not found, it can be said that ω assisted in the precipitation of fine α particles and was consumed in the process or dissolved into the β matrix during the 4 hours at the aging temperatures. As for the specimens, in which ω was confirmed to exist, i.e. those in the AW condition and those heat treated at 804°C/1h, ω was quenched in after cooling from above the β-transus or sufficient time was not available for dissolution of the ω-phase.

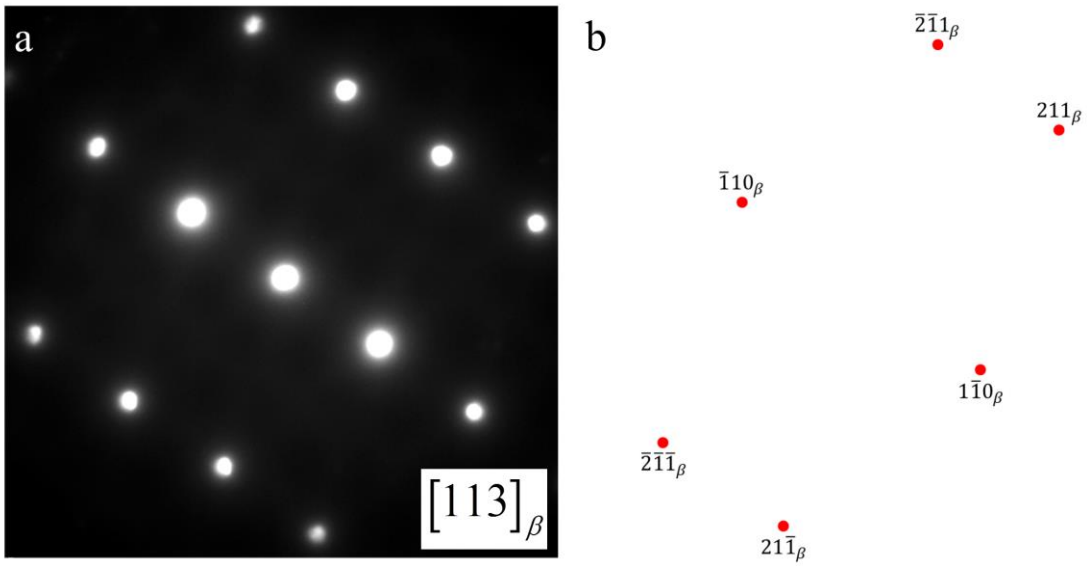

Figure 3.40. (a) SAD pattern of the $[113]_\beta$ *zone axis and (b) an enlarged schematic of (a) from the FZ of a specimen heat treated at 700°C/4 hours. The indices in red boxes correspond to the ω-phase.*

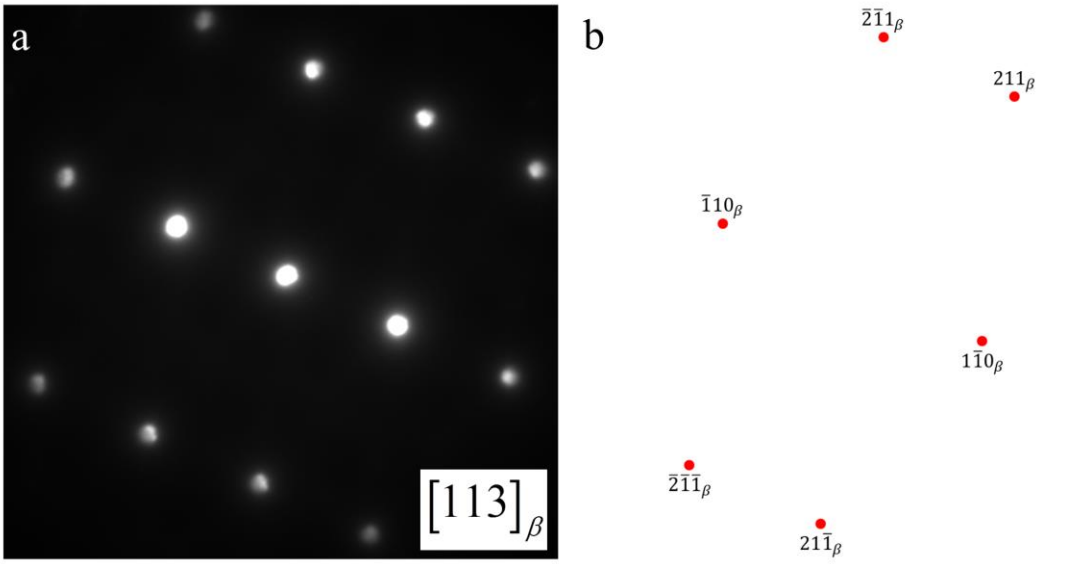

Figure 3.41. (a) SAD pattern of the $[113]_\beta$ *zone axis and (b) an enlarged schematic of (a) from the FZ of a specimen heat treated at 804°C/1 hour followed by aging at 600°C/4 hours. The indices in red boxes correspond to the ω-phase.*

3.4.3. Section 3.4 Summary

TEM analysis of the EBW Ti-5553 specimens confirmed the presence of ω and α. In specimens containing ω, superlattice reflections appeared at $1/3(211)_\beta$ and $2/3(211)_\beta$ in the $[113]_\beta$ zone axis pattern. If α was present, superlattice reflections were found as either satellite

reflections around the $\{002\}_{\beta}$ and $\{011\}_{\beta}$ reflections, lattice streaking, between the central spot and the $\{002\}_{\beta}$ and $\{011\}_{\beta}$ reflections, or between the $\{002\}_{\beta}$ and $\{011\}_{\beta}$ reflections. ω was found to exist in the AW condition as well as after heat-treatment at 804°C/1 hour. This suggests that ω forms upon cooling from above the β-transus and is present at beginning of each PHWT. It forms as small particles, less than 10 nm in size. Heat-treating at 804°C/1 hour was not an adequate PWHT to completely eliminate ω, but it did however precipitate α. α was also confirmed to be present in the specimens heat treated at 700°C/4 hours and at 804°C/1 hour followed by aging at 600°C/4 hours, supporting the LOM and SEM results. ω, on the other hand, was not present in these specimens. This indicated that the longer heat treatments at lower temperatures provided sufficient times, during which α could nucleate in the presence of ω and ω could be consumed by the growth of α or be eliminated by dissolution into the β-phase.

3.5. HAADF-STEM Investigation of ω in the FZ of As-Welded Ti-5553

To investigate the ω-phase present in the FZ of specimens in the AW condition of EBW Ti-5553, high angle annular dark field scanning transmission electron microscopy (HAADF-STEM) was employed. Specimens were oriented with $[110]_{\beta}$ zone axis parallel to the beam direction. This was done to exploit the orientation relationship, $\langle 11\bar{2}0\rangle_{\omega}//\langle 1\bar{1}0\rangle_{\beta}$, so that the coherent ω-phase could be discerned from the β matrix. In work on a Ti-9 at.%Mo (18 wt.%Mo) alloy, Devaraj et al. [Devaraj et al. 2012] provided high resolution TEM (HRTEM) and HAADF-STEM images of the ω-phase in the same orientation. From the HAADF-STEM images, they were able to observe various stages in transformation between athermal (partially transformed) ω and isothermal (fully transformed) ω due to isothermal annealing at 475°C performed after β-solutionizing and quenching. Devaraj et al. also showed results for the displacement of atoms caused during the collapse of the $\{111\}_{\beta}$ planes upon formation of ω. In the present investigation

of EBW Ti-5553 similar results have been obtained as well as other interesting findings, which make the presence of ω in Ti-5553 comparatively unique.

Figure 3.42 shows the original and Fourier filtered HAADF-STEM images wherein multiple ω particles are clearly evident. The ω particles appear to be approximately 5 nm in diameter; however, due to the thickness of the specimens only small slivers of the particles can be observed from regions, which may not be representative of their true center. Therefore, the true diameter of the ω particles may be larger than 5nm.

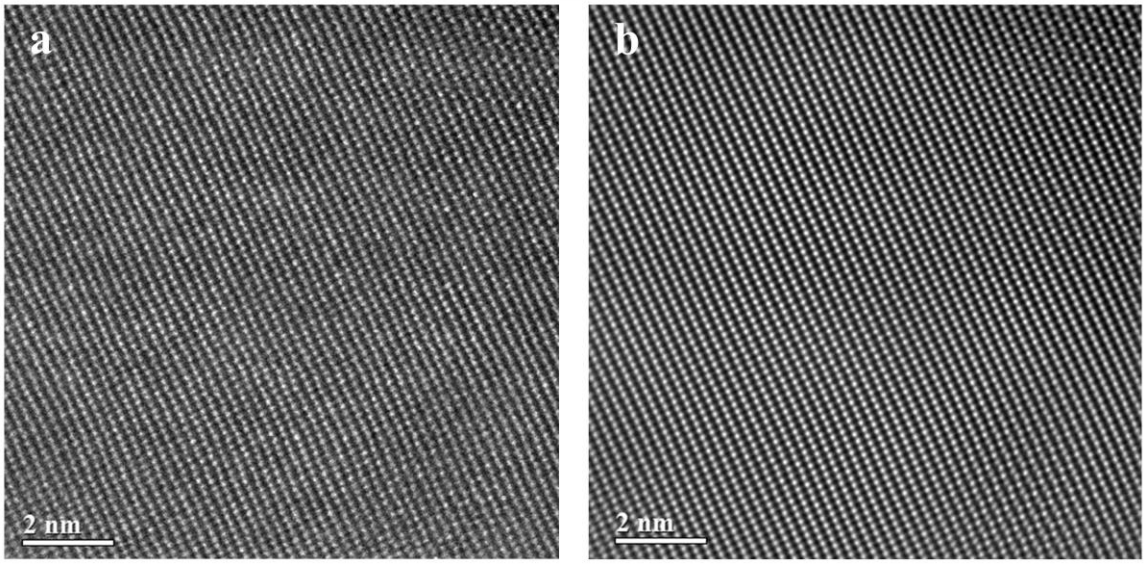

Figure 3.42. HAADF-STEM images of ω in the FZ of EBW Ti-5553 in the AW condition acquired in the $[110]_\beta$ beam direction. (a) original and (b) Fourier filtered.

ω particles were also found to be oriented in two specific orientations with respect to one another and β, i.e. two variants of ω (ω1 and ω2) exist that correspond to the superlattice reflections in the $[110]_\beta$ zone axis pattern. The $[110]_\beta$ SAD pattern, Fast Fourier Transform (FFT) of Figure 3.42a, and RGB composite of Fourier filtered images of Figure 3.42a are shown in Figure 3.43a, b, and c, respectively. $[110]_\beta$ zone axis patterns, similar to that in Figure 3.43a, have been reported that also exhibit the same superlattice reflections for ω in β-solutionized and low-temperature-aged Ti-5553 and other β alloys [Harper, 2004; Nag, 2008; Prima et al., 2006; Devaraj et al., 2012]. The FFT is analogous to the $[110]_\beta$ SAD pattern taken from the same

specimen indicating that the two ω variants are present in the image. An RGB composite of Fourier filtered images of the matrix (blue) and the two variants of ω1 (red) and ω2 (green) from Figure 3.42a was created to highlight the variants.

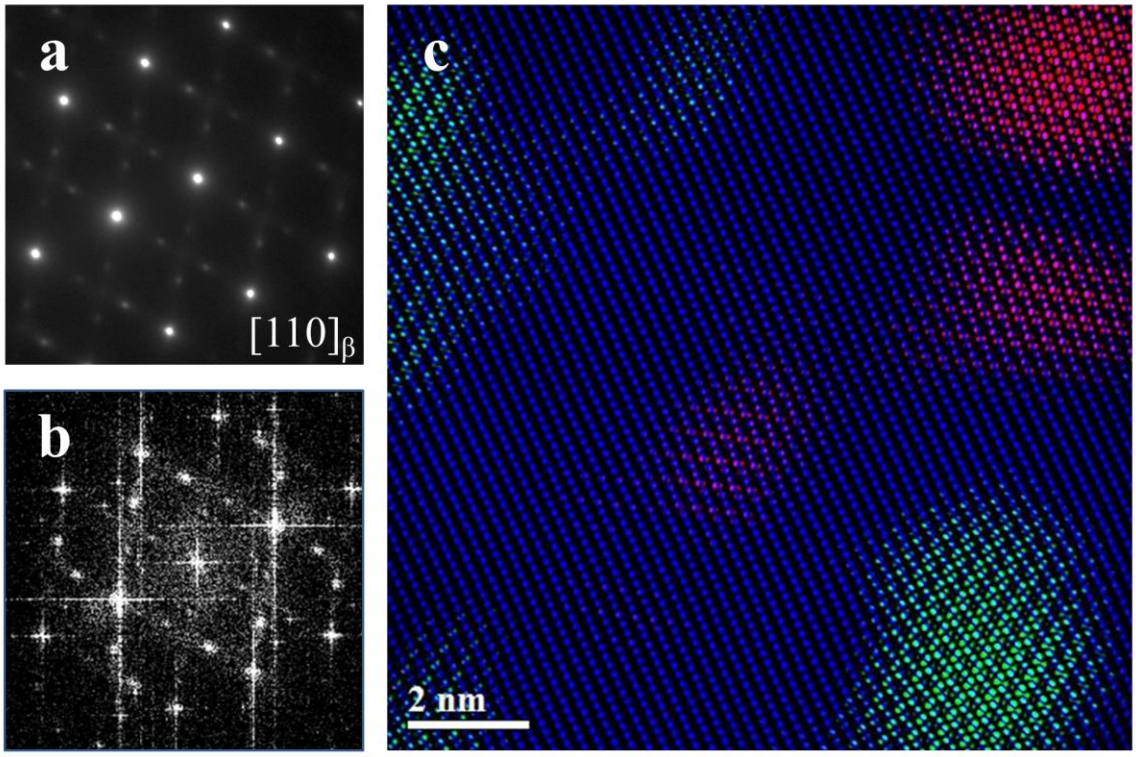

Figure 3.43. (a) [110]$_\beta$ zone axis pattern acquired from the FZ of the EBW Ti-5553 specimen in the AW condition along with the (b) fast Fourier transform of Figure 1a and (c) an RGB composite created from three separate masks of the fast Fourier transform in (b) for the β matrix (blue), the ω1 variant (red), and the ω2 variant (blue).

The values of a_ω and c_ω are geometrically based on the lattice parameter of the β-phase, measured to be a_β=3.35±0.013 Å. Therefore, the lattice parameters for ω may be calculated in the $\langle 111 \rangle_\beta$ and $\langle 112 \rangle_\beta$ directions as a function of a_β using the relations, $a_\omega = a_\beta\sqrt{2}$ and $c_\omega = a_\beta(\sqrt{3})/2$. The ω lattice parameters, a_ω and c_ω, were determined to be 4.74±0.018 Å and 2.90±0.011 Å, respectively. These values are in relatively good agreement with those reported by Silcock [Silcock, 1956] and Bagariatskii et al. [Bagariatskii et al., 1955] (a_ω=4.60 Å and c_ω=2.82 Å) considering their work focused on binary Ti-V, Ti-Mo, and Ti-Cr alloys, whereas Ti-5553 contains five alloying elements. In a review of ω-phase formation Hickman [Hickman, 1969b]

stated that the values of c and a may vary due to alloying element and alloy content, but the ratio of c to a is always 0.613. The c/a ratio for ω in Ti-5553 was determined to be 0.612, which is within experimental error. The variation in lattice parameters, a and c, from those reported by Silcock and Bagariatskii et al. can be attributed to the alloying elements (Al, Mo, V, Cr, and Fe) comprising Ti-5553. Their radii and concentrations of solute elements within the alloy cause slight changes in lattice spacing, which change the lattice parameters compared to other alloys.

Atomic ordering of the ω-phase has also been observed in the FZ of EBW Ti-5553. This ordering is evident along the $\langle 111 \rangle_\beta$, $\langle 112 \rangle_\beta$, and $\langle 110 \rangle_\beta$ directions in the HAADF-STEM images (Figure 3.44). Instead of solute atoms being randomly distributed about lattice sites as in the β matrix, which gives rise to a uniform intensity, the atoms are ordered. The HAADF-STEM images were acquired with collection angles between 90-370 mrad, making the contrast observed in the images directly proportional to the atomic number (Z) of the atoms, i.e. atoms with higher atomic numbers appear brighter and atoms with lower atomic numbers appear relatively darker. The ordering of ω in T-5553 may be thought of as a series of three repeating layers. Rows of atoms perpendicular to the $\langle 111 \rangle_\beta$, $\langle 112 \rangle_\beta$, and $\langle 110 \rangle_\beta$ directions are arranged in such a way that the intensities of the atomic columns may be seen to change from high (row 1), to low (row 2), to medium (row 3), and finally back to high, where the layering repeats (Figure 3.44). Depending on the direction, from which one chooses as a reference, the intensities may be ordered as such: high, low, medium, high, or high, medium, low, high.

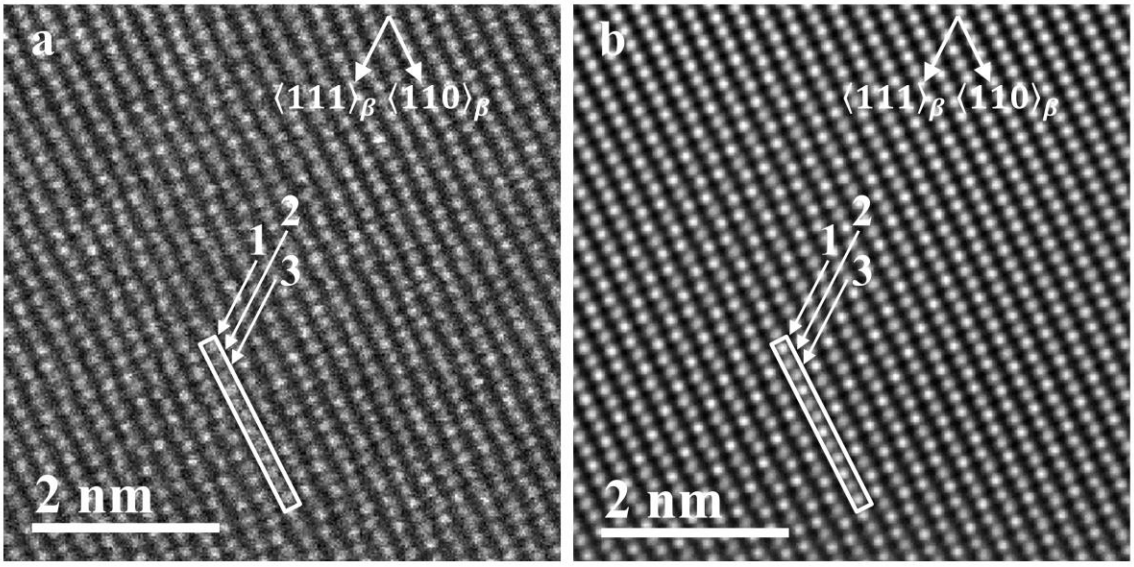

Figure 3.44. HAADF-STEM image a ω particle with the surrounding β matrix indicating the rows (1, 2, 3) and direction in which the intensities can clearly be seen to vary due to atomic contrast. (a) original and (b) Fourier filtered.

Figure 3.45 shows an intensity profile taken along the $\langle 110 \rangle_\beta$ direction, in which atomic columns display the ordering of high, low, medium, high. It is clearly evident that the intensities vary in the proposed scheme. The peak intensities are uniform for equivalent atomic columns. One could reason that the peaks of highest intensity correspond to elements with a high relative Z, peaks of low intensity correspond to elements with a low relative Z, and peaks of medium intensity correspond to elements with a medium relative Z. In the Ti-5553 system these high, low, and medium peak intensities can be related to atomic contrast caused by Mo, Al, Ti, V, Cr, or Fe or a combination of these elements occupying specific lattice sites along the atomic columns within ω. However, the intensities of the atomic columns within row 1 were noticed to have approximately the same as the average intensity in the matrix. This suggests that these columns are randomly occupied by the alloying elements, similar to the matrix. Only qualitative observations may be made at this point without atomic resolution spectral analysis.

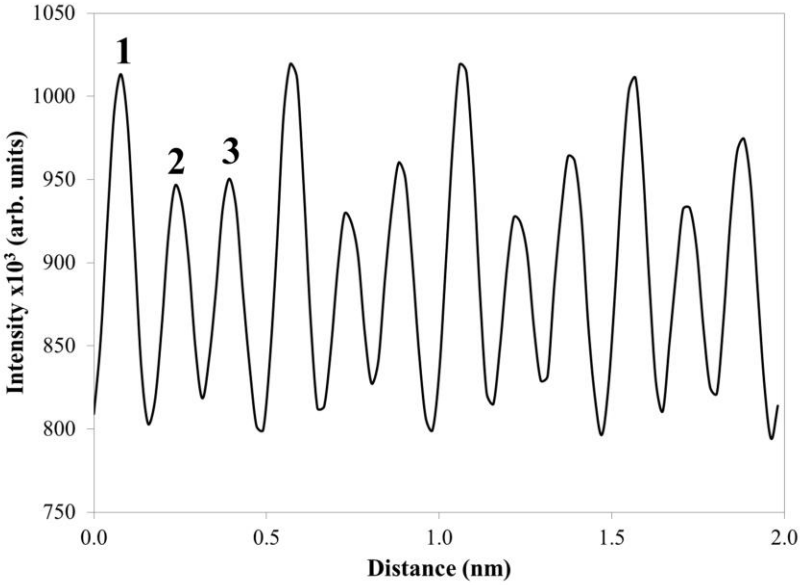

Figure 3.45. Intensity profile in the $\langle 110 \rangle_\beta$ direction showing the tri-layer atomic ordering of the ω-phase in the FZ of EBW Ti-5553 in the AW condition. Rows 1, 2, and 3 are labeled above the peaks. The location from which the profile was acquired is indicated by the white box in Figure 3.43.

Ordering of the ω-phase has been reported by Bendersky et al. [Bendersky et al., 1990], Strychor et al. [Strychor et al., 1988] Kestner-Weykamp et al. [Kestner-Weykamp et al., 1989] and Zhang et al., [Zhang et al., 1994]. However, the structures observed were admitted by the authors to "ω-like." Most of the structures were also said to have c lattice parameters that were twice that of typical ω and were found to take on coherent, ordered DO_{19}, B2, or $B8_2$ structures [Kestner-Weykamp et al., 1989; Strychor et al., 1988]. Not only did the so-called order ω take on different types not typical of ω, but they were found in Ti-Al-X (X = Nb, Cr) alloys known as titanium aluminides, not metastable β-Ti alloys.

Also observed within the ω particles is a displacement of atoms, which is expected in the shuffle (displacive) transformation of β to ω. Figure 3.46 shows schematics of cells of atoms representing β-Ti, fully transformed (isothermal) ω, and partially transformed, ordered ω with the $\langle 110 \rangle_\beta$ direction oriented normal to the page. For 2D illustration only, the cells are made up of 6 atoms, one at each corner and two along the $\langle 110 \rangle_\beta$ direction. Relative to the β-phase and corner

atoms, the atoms along the $\langle 110 \rangle_\beta$ direction (atoms in rows 2 and 3) in the partially transformed and fully transformed ω cells have displaced towards the center of each cell in the $\langle 111 \rangle_\beta$ directions. This displacement reflects the collapse of the $\{111\}_\beta$ planes in the $\langle 111 \rangle_\beta$ direction (Figure 1.8). Figure 3.47 is a plot of the overlapped intensities acquired along rows 1, 2, and 3 in the $\langle 111 \rangle_\beta$ direction. It shows that as the distance towards the center of a ω precipitate from the β matrix increases, the relative displacements of the atoms in rows 2 and 3 in relation to row 1 (which should not change) increases. The HAADF-STEM insets in Figure 3.47 are representative of the β (left) and ω (right), which depict the displacements plotted in the intensity profiles of rows 2 and 3 in comparison to row 1. A complete transformation of β to ω did not occur in the FZ of EBW Ti-5553, but rather the transformation was cut short and ended in an incomplete stage. Devaraj et al. [Devaraj et al., 2012] showed similar results in their work on a Ti-18 wt.%Mo alloy using HAADF-STEM techniques. However, upon aging for 48 hours they observed a complete transformation to isothermal ω.

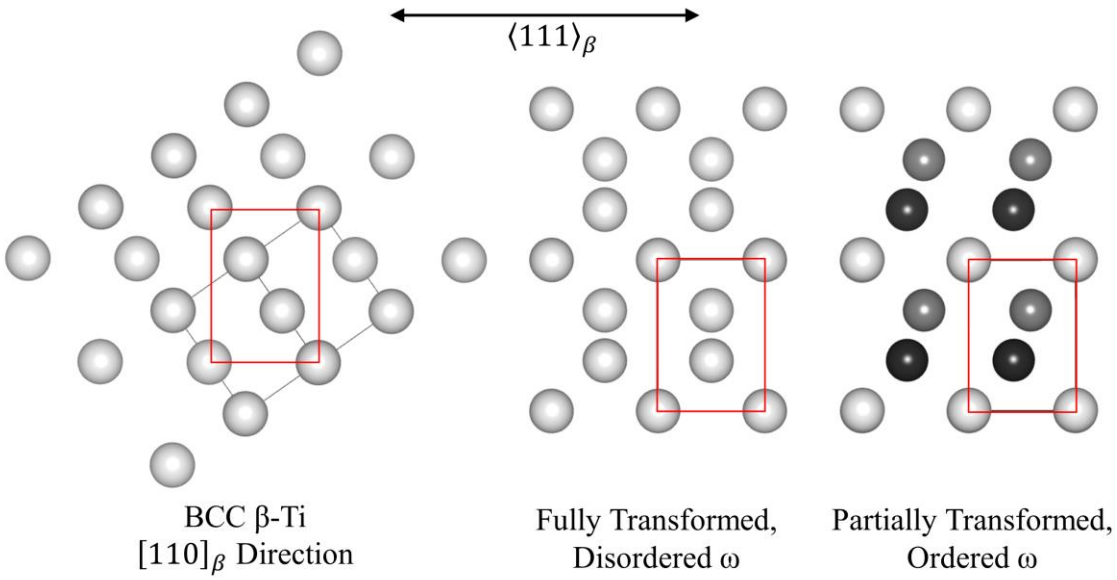

Figure 3.46. Schematic of the atomic arrangement in β (BCC), fully transformed, disordered ω (isothermal ω), and partially transformed, ordered ω as evidenced in the FZ of Ti-5553, left, center, right, respectively, with the $\langle 110 \rangle_\beta$ direction normal to the plane of the page. The red box represents an equivalent cell in each schematic. The tri-layering can be seen in the partially transformed and ordered ω.

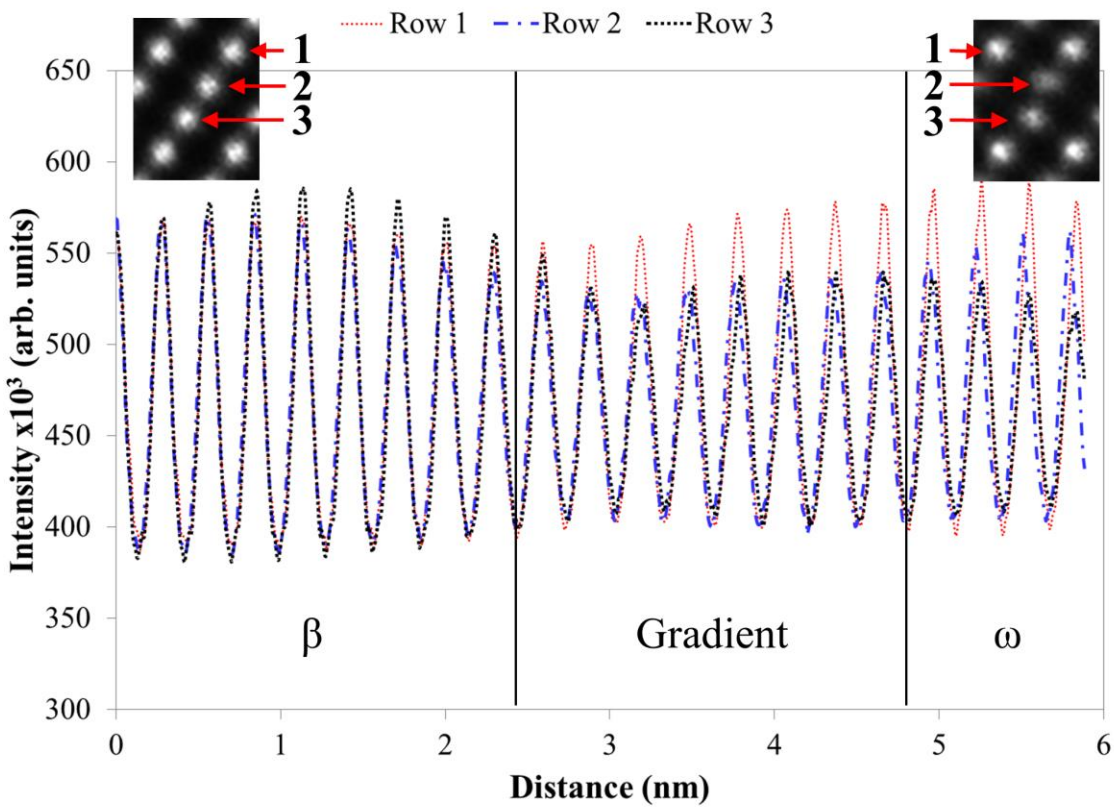

Figure 3.47. Overlaid intensity profiles for rows 1, 2, and 3 as indicated in the insets acquired along the $\langle 111 \rangle_\beta$ direction in figure 3.48 from β to ω.

ω is already known to be coherent with the β matrix. The coherency of ω in the FZ of EBW Ti-5553 in the AW condition can be seen in Figures 3.42, 3.44, and 3.48. Unlike the simplified schematics of coherent particles, in which there is an obvious interface where the particle starts and the matrix ends, ω particles in the FZ of EBW Ti-5553 in the AW condition were observed to display a gradient of atomic displacement from the β matrix to the center of the ω particle. Figure 4a shows HAADF-STEM images of a ω particle, in which the coherency with the β matrix and gradient of atomic displacement is clearly discernable. De Fontaine et al. [De Fontaine et al., 1971] explained the transformation of β to ω using the *phonon mechanistic model*, which gave rise to a continuum of different stages during the transformation from β to ω. A segment of this continuum of transformation may be seen as a gradient of atomic displacement between β and the center of the ω particle in the intensity profiles plotted in Figure 3.47 and in the

HAADF-STEM images in Figure 3.48. The β and ω structures seamlessly blend into each other, blurring a discrete boundary between the two. Within the gradient, the relative displacements of the atoms from their original positions in the β matrix increase until their displacements no longer change in the center of the ω particle. At this point, the ω particle has reached the extent of its transformation.

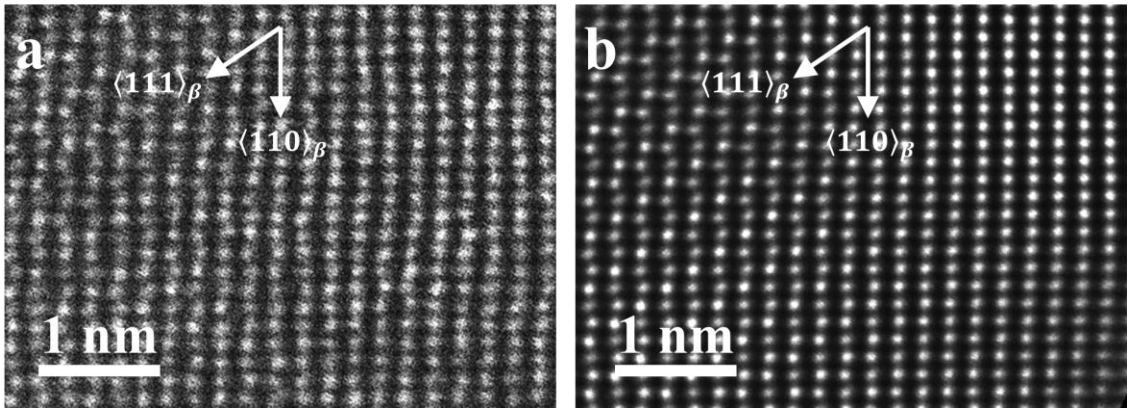

Figure 3.48. HAADF-STEM image of a ω precipitate and the surrounding β matrix wherein the atomic displacement within the ω-phase, a gradient of transition from β to ω, the coherency of the ω-phase with β, and distortion of the β lattice around the ω precipitate can be seen. (a) original and (b) Fourier filtered.

Also noticed in Figure 3.48, is a distortion of the β lattice around the ω particle along the $\langle 110 \rangle_\beta$ direction where the β lattice appears to bend in towards the center of the image. Distortion, like this are caused by lattice strain due to the presence of the ω precipitates. Though not as obvious in other locations, the distortion is present because there must be some amount of strain associated with the displacement, ordering of the atoms, shape, and crystal structure within ω that affects the surrounding β lattice. The lattice tends to distort such that it bends around the ω precipitate, suggesting that lattice is in tension rather than compression. The lattice strain and accompanying strain energy provides sites for nucleation of α during precipitation treatments in order to minimize interfacial energy between ω and β [Ohmori, et al. 1998; Williams et al. 1969].

3.5.1. Section 3.5 Summary

Atomic resolution HAADF-STEM imaging of the ω-phase in FZ of the AW specimens provided evidence as to the structure and order of the ω-phase in EBW Ti-5553. The average size of the ω particles was determined to be approximately 5 nm and coherent with the β matrix. A gradient of atomic displacement from the β matrix to the center of the ω particles was observed, which proves that the ω-phase is truly coherent with the β-phase. The displacement of the atoms within the gradient and the ω-phase, in general, is direct evidence of the collapse of the $\{111\}_\beta$ planes in the $\langle 111\rangle_\beta$ direction. Atomic number contrast in the HAADF-STEM demonstrated that the ω-phase is ordered. The ordering manifested itself as a tri-layered structure wherein the first layer consisted of atomic columns of relatively high atomic numbers, followed by the second layer of atomic columns with relatively low atomic numbers, and the third row made up of atomic columns with relatively moderate atomic numbers. The ordering, however, did not disrupt the normal crystallographic structure of the ω-phase and the lattice parameters, a and c, were found to be 4.74±0.018 Å and 2.90±0.011 Å, respectively, and are in agreement with the reported lattice parameters within experimental error. Distortion of the BCC β lattice caused by the ω particles implied that there is lattice strain and strain energy associated with the presence of ω.

3.6. Fracture of EBW Ti-5553

The results from tensile testing indicated that the material within the WZ experienced no noticeable macroscopic ductility in all conditions except for the specimens heat treated at 700°C/4h. However, the plasticity exhibited by those specimens was comparatively little in contrast to the elongation of Ti-5553 in the un-welded condition as reported by Mitchell et al. [Mitchell et al., 2011] and Fanning [Fanning, 2005]. Contrary to the tensile testing results, all of

the fracture surfaces of the FZs evidenced microvoid coalescence (dimples) as shown in Figures 3.49 through 3.52, but simultaneously exhibited trans- or intergranular fracture facets characteristic of brittle fracture. The FZs of specimens in the AW condition and the FZs of those specimens heat-treated at 804°C (Figures 3.49 and 3.51) appeared to have undergone fracture tending more towards transgranular cleavage rather than intergranular fracture. The fracture facets are flat and contain evidence of cleavage planes. Ideally, transgranular cleavage would have perfectly matching facets and be flat and featureless. However, the polycrystalline nature of the material causes cleavage to change direction when crossing a grain boundary or second phase. Complicating transgranular cleavage are particles (α and ω precipitates in this case), impurities, and pores, which may initiate localized fracture before the front of a cleavage crack reaches that particular region. At higher magnifications of the fracture surfaces (inset images in Figures 3.49 and 3.51) of the AW specimens and specimens heat-treated at 804°C/1h, the cleavage facets were observed to be littered with fine microvoids. This suggests that localized deformation manifested itself as microvoids due to the presence of α and/or ω, at which voids nucleated. The influence of ω will be discussed further in section 3.6.1.

The FZs of specimens heat-treated at 700°C/4h showed signs of both intergranular and transgranular fracture (Figure 3.50), while those of specimens heat-treated at 804°C/1h followed by aging at 600°C/4 displayed signs of only intergranular fracture (Figure 3.52). Here it is obvious that the fracture facets more closely resemble grains in three dimensions, which is indicative of intergranular fracture. In addition to the transgranular cleavage and intergranular fracture, fine microvoids on the fracture facets were observed at higher magnifications in both conditions as well (inset images in Figures 3.50 and 3.52). The intergranular appearance and presence of fine microvoids may be attributed to grain boundary α and PFZs adjacent to the grain boundary α. Grain boundary α and PFZs are detrimental to β-Ti alloys' mechanical properties, because of a distinct strength mismatch between the grain boundary α (hard) and the PFZ

(ductile) [Sauer et al., 2001; Lütjering et al., 2007]. Due to this lack of strength in PFZs and their location immediately adjacent to comparatively hard, intergranular α, fracture likely occurs along grain boundaries within the PFZs wherein intergranular fracture facets with very fine microvoids on their surfaces develop. Microvoids can develop in the PFZs, because the BCC β-phase is ductile compared to the surrounding grain boundary α and α-strengthened β grain interiors. Even though there are wide PFZs in the specimens heat-treated at 804°C/1h, fracture was noted to be transgranular, not intergranular. This is due to the coarse distribution of coarse α precipitates, which do not impart much strength to the EBW Ti-5553 as seen in the mechanical properties (section 3.1) and allow for relatively unimpeded dislocation movement and crack propagation through the grain interiors.

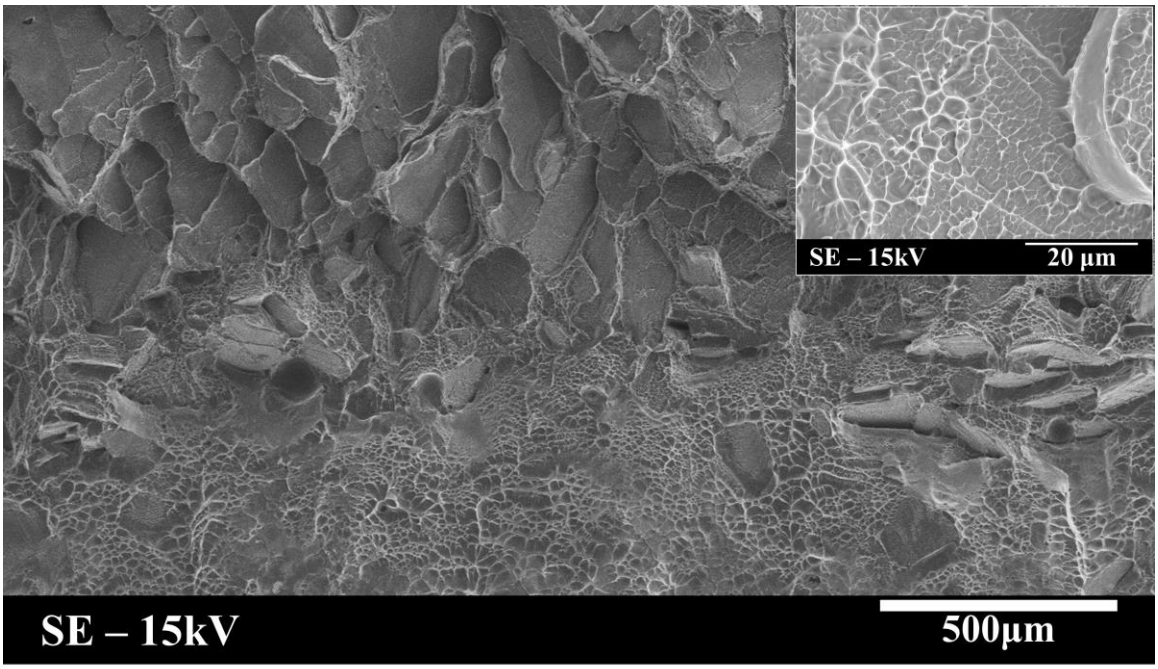

Figure 3.49. Representative secondary electron image of the fracture surface of an EBW Ti-5553 in the AW condition. The FZ (top half of image) shows indications of transgranular cleavage facets and the HAZ (bottom half) shows microvoid coalescence. The inset image of the FZ also shows clear signs of fine microvoid coalescence on the cleavage facets.

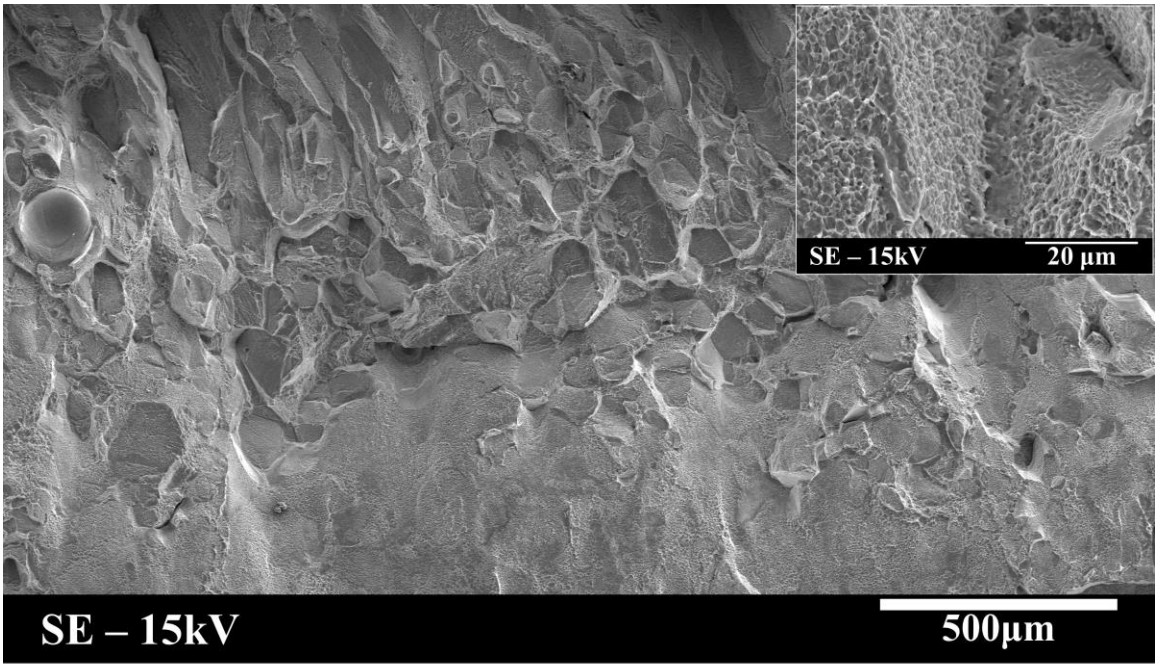

Figure 3.50. Representative secondary electron image of the fracture surface from an EBW Ti-5553 tensile specimen, which was heat-treated at 700°C/4h. The FZ (top half of image) exhibits evidence of transgranular cleavage facets and intergranular fracture and the HAZ (bottom half) shows microvoid coalescence. The inset image clearly shows the presence of microvoid coalescence on the fracture facets in the FZ (top half of image).

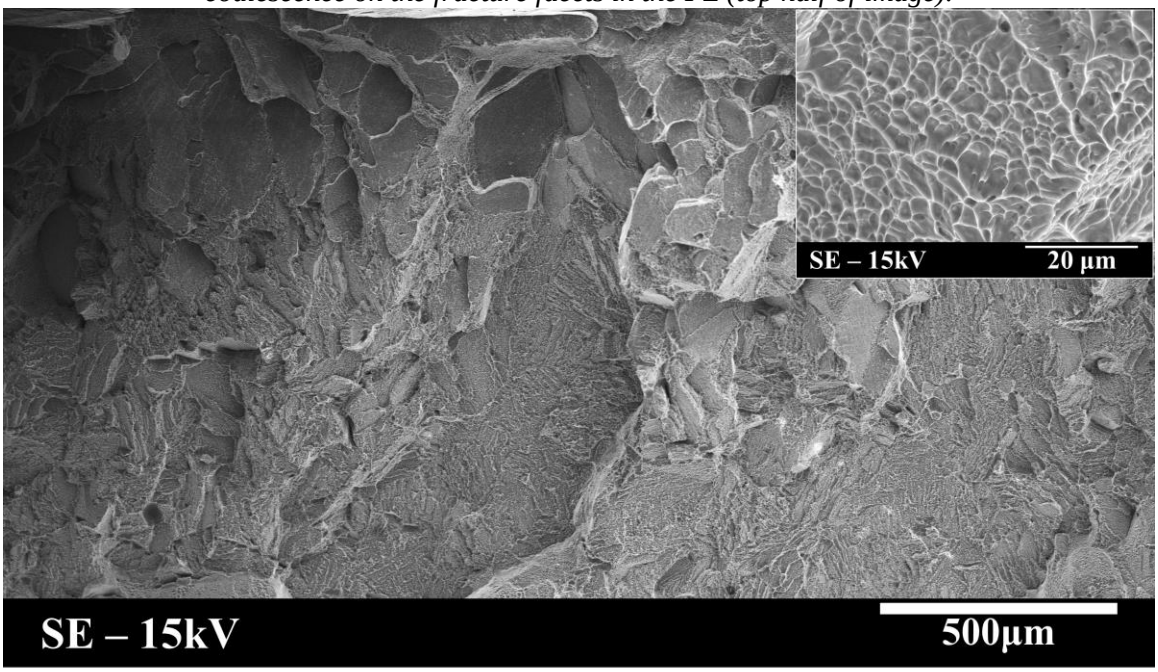

Figure 3.51. Representative secondary electron image of fracture surfaces from an EBW Ti-5553 tensile specimen, which was heat treated at 804°C/1h. The FZ and HAZ (top half and bottom half of image, respectively) exhibit evidence of transgranular cleavage. The inset image clearly shows the presence of microvoid coalescence on the fracture facets.

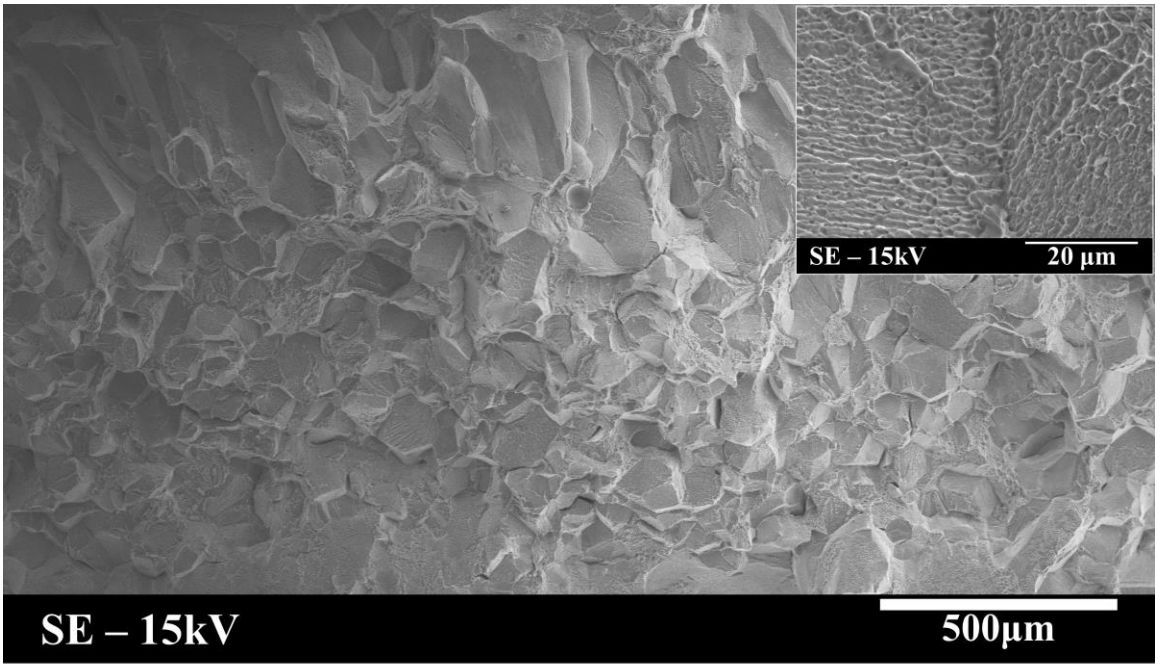

Figure 3.52. Representative secondary electron image of fracture surfaces from an EBW Ti-5553 tensile specimen, which was heat-treated at 804°C/1h followed by aging at 600°C/4h. The FZ and HAZ (top half and bottom half of image, respectively)exhibit evidence of intergranular fracture. The inset image clearly shows the presence of microvoid coalescence on the fracture facets in the FZ (top half of image).

It should be reiterated that the above observations were made for fracture observed in the FZ. Fracture in the majority of the specimens was not confined solely to the FZ, but rather to the WZ, i.e. the FZ and HAZs. Figures 3.49 through 3.52 show this as well. Specimens in the AW condition and PWHT condition at 700°C/4h show two different types of fracture occurring in the WZs. The specimens in the AW condition (Figure 3.49) exhibit transgranular fracture in the FZ (top half of the image) and typical ductile fracture, i.e. coarse microvoid coalescence, in the HAZ (bottom half of the image). Similarly, specimens heat-treated at 700°C show a mixture of transgranular cleavage and intergranular fracture in the FZ and ductile fracture in the HAZ (top and bottom of Figure 3.50, respectively). On the other hand, specimens heat-treated at 804°C/1h and at 804°C/1h followed by aging at 600°C/4h showed more or less the same type of fracture through their respective FZs and HAZs (Figures 3.51 and 3.52). The specimens heat-treated at

804°C/1h exhibited transgranular cleavage, while those heat-treated at 804°C/1 hour followed by aging at 600°C/4 hour exhibited intergranular fracture.

Supporting these observations are Figures 3.53 through 3.56, wherein the cross-sections of fracture surfaces are given for the specimens in Figures 3.49 through 3.52. It can be seen that fracture not only occurred in the FZs but also in the HAZs, except in the case of the specimen heat-treated at 804°C/1hr. In this particular specimen fracture was concentrated entirely within the FZ. Fracture through the FZ can most likely be attributed to the presence of ω and the lack of fine α platelets within the grain interiors to prohibit crack propagation and impart strength to the β-phase. Also, due to the similarly oriented grains within FZ, a cleavage plane travelling through a grain would not have to dramatically change direction when crossing a grain boundary in the FZ. Whereas in the HAZ, the grains are equiaxed and randomly oriented, making cleavage plane propagation more difficult when encountering a grain boundary. Therefore, it takes the path of least resistance – through the FZ.

By this reasoning, one might argue that similar fracture should have occurred in the other specimens. However, this is not the case. Narrow PFZs in the specimens heat treated at 700°C/1h and in those heat-treated at 804°C can act as stress concentrators and be the paths of least resistance for crack propagation. The fine distribution of α platelets in the grain interiors and grain boundary α inhibits cracks and deformation, effectively redirecting cracks to the PFZs. As for the specimens in the AW condition, it can be said that ω is responsible for the transgranular cleavage in the FZ. Without α-phase strengthening the β grains or PFZs flanking grain boundaries, cracks nucleated by dislocations shearing through ω may propagate uninterrupted through the material giving rise to the transgranular cleavage.

The change of fracture mechanisms between the FZs and HAZs in the specimens in the AW condition and those heat-treated at 700°C is not quite understood without further investigation into the precipitation events in the HAZs. It can be hypothesized, however, that due

to the temperature gradient through the HAZ during welding, that the kinetics of precipitation are different from the FZ. This could potentially give rise to coarser ω precipitates or even fully transformed, isothermal ω in the HAZ compared to the athermal ω already known to exist in the FZ. Not only could ω precipitation be affected, but also α precipitation. Harper [Harper, 2004] showed that α precipitated in Ti-5553 during furnace cooling from 910°C to room temperature. Because α is known to nucleate in the presence of ω and has been seen to precipitate upon cooling from above the β-transus in Ti-5553, it is not out of the question that the initial stages of α precipitation and growth on the nanometer scale may have occurred in the HAZs during EB welding if the thermal gradients and cooling rates promoted such transformations. The subsequent precipitation during PWHTs would then be different from that in FZ, wherein no α was observed after EB welding.

Solidification's effects on fracture cannot be discounted either. Solute segregation during solidification was seen to occur, resulting in cellular dendrites within the FZ. Thompson et al. [Thompson et al., 1977] suggested that microvoid nucleation occurs on solidification substructure, which may be used along with ω effects on formation of microvoids on the fracture facets. The composition gradients associated with the cellular dendrites may also alter the precipitation kinetics locally within the FZ, promoting α precipitation in either the dendrite cores or interdendritic regions during precipitation heat treatments without prior homogenization. Nag et al. [Nag et al., 2012] proposed that local compositional fluctuations within Ti- 5553 can result in the stability of α-phase over that β-phase compared to the bulk of the material at a given temperature. If very small composition fluctuations over small distances can shift the stability from β to α, than it may be argued that an even larger compositional inhomogeneity will have a greater effect on the precipitation of α. This would lead to inhomogeneous α precipitation within the FZ during PWHTs and ultimately affect the mechanical properties and fracture.

Figure 3.53. Cross-section of the fracture surface in Figure 3.49 showing fracture through the FZ (top) and HAZ (bottom) of the EBW Ti-5553 specimen in the AW condition.

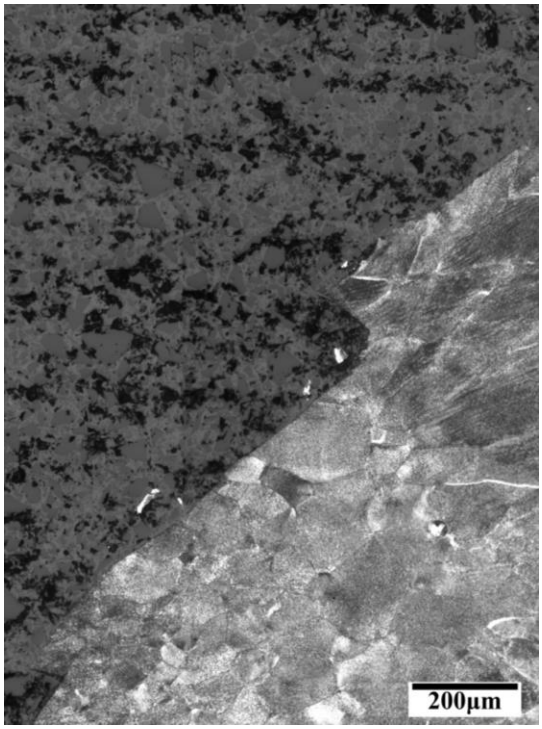

Figure 3.54. Cross-section of the fracture surface in Figure 3.50 showing fracture through the FZ (top) and HAZ (bottom) of the EBW Ti-5553 specimen heat treated at 700°C/4h.

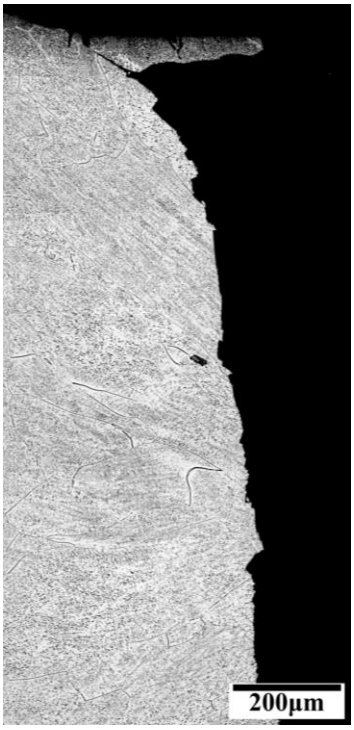

Figure 3.55. Cross-section of the fracture surface in Figure 3.51 showing fracture through the FZ (top) and HAZ (bottom) of the EBW Ti-5553 specimen heat treated at 804°C/1h.

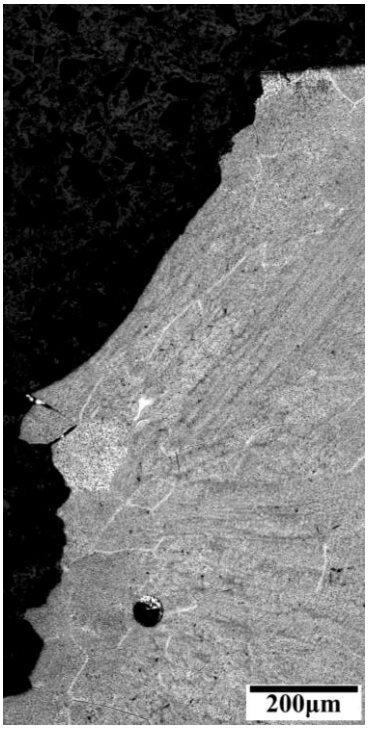

Figure 3.56. Cross-section of the fracture surface in Figure 3.49 showing fracture through the FZ (top) and HAZ (bottom) of the EBW Ti-5553 specimen heat treated at 804°C/1h followed by aging at 600°C/4h.

3.6.1. Influence of ω on Fracture

Many investigations have been undertaken in order to understand the effects of ω on the mechanical properties of β-Ti alloys, which were predominantly alloyed with transition metals [Hickman, 1969a; Hickman, 1969b; Luke et al., 1964; Luke et al., 1964; Williams et al., 1971; Bowen, 1971; Bowen, 1980]. ω-phase has been shown to embrittle β-Ti alloys due to the high stress required to shear the particles. This embrittling process caused by particle shearing may be explained by a set of dislocations gliding along a particular slip plane and shearing ω particles. This creates a softened channel, through which slip can occur more easily. Gysler et al. [Gysler et al., 1974], in work conducted on aged Ti-Mo alloys, have shown that these channels develop primarily along the $\{110\}_\beta$ planes and to a lesser extent along the $\{112\}_\beta$ and $\{123\}_\beta$ planes. The accompanying burger's vector to these slip planes is $1/2\langle 111\rangle_\beta$. Channeling of deformation by slip limits the number of slip bands and forces the slip bands to be narrow, which causes local deformation and high stress concentrations. When these slip bands meet or intersect a grain boundary, cracks nucleate and propagate as a result of the stress concentration even at low macroscopic plastic strains. Dark field images of the ω-phase in the vicinity of the slip bands indicated a lower concentration of ω particles most likely due to a large number of particle shearing instances [Gysler et al, 1974]. Because of the softened channel created in the wake of sheared ω particles, dimples due to microvoid coalescence in the β matrix develop as cracks nucleate and propagate [Gysler et al., 1974]. Likewise, narrow PFZs concentrate stress and cracks nucleate within these softened regions and propagate through the soft zones. Hence, the PFZs would serve as regions for easy crack propagation because no strengthening particles exist in these regions. This lends itself to the intergranular fracture appearance in the SEM images.

From the HAADF-STEM work performed on the AW specimens, qualitative observations may be made about ω's effect on the macroscopic brittle behavior of the FZ within

EBW Ti-5553 in the AW condition. The atomic ordering and lattice strains may impart the most dramatic effects on the ductility of the FZ. Firstly, when a phase is ordered, it typically signifies a state with the lowest possible Gibbs free energy (G) under given conditions. Any change to this order will increase G, which is unfavorable. In ordered systems, such as in the Fe_3Al system with the DO_{19} superlattice, $1/3\langle 11\bar{2}0\rangle$ dislocations in the disordered hexagonal lattice are severely hindered by the ordering, because they create disorder across the slip plane that separates the sheared and unsheared regions of the lattice [Marcinkowski et al., 1961]. Similar observations were reported by Blackburn [Blackburn, 1968] in work performed on a Ti-Al alloy containing an ordered Ti_3Al structure (DO_{19} crystal structure). He reported that dislocations, in order to continue along their path, must shear through the ordered Ti_3Al phases. Correspondingly, it is generally accepted that the ω-phase causes embrittlement in β-Ti alloys due to dislocations shearing the particles [Lütjering and Williams, 2007; Bowen, 1971; Gysler et al., 1974]. Because tri-layer ordering was observed in the ω particles in the FZ of EBW Ti-5553, it is plausible that dislocation motion through ω is consequentially more difficult. Therefore, brittle-like fracture would be more likely to occur.

The lattice strains in the surrounding matrix associated with the presence of ordered ω particles may also contribute to the brittle behavior of the FZ. Because the lattice appears to be distorted around the ω particles, with which a lattice strain is associated, dislocations may either be repulsed or attracted to these regions. In either case, dislocations would pile up at the ω/β interfaces or elsewhere and act as the sites of localized deformation or crack nucleation, ultimately initiating fracture. Coupled with the well-known embrittling effects of ω and the probable increased difficulty of dislocation motion through ordered ω, macroscopic brittle characteristics in the FZ of EBW Ti-5553 in the AW condition may be accounted for.

3.6.2. Section 3.6 Summary

Macroscopic brittle-like fracture occurred in WZs of all specimens regardless of whether the specimens were heat treated or in the AW condition. Transgranular cleavage, intergranular fracture, or combinations of the two were observed in the FZs. Accompanying this evidence of brittle fracture were fine microvoids located on the fracture facets, only visible at higher magnifications. Their presence suggested that some degree of ductility existed during tensile deformation in spite of the tensile results. The microvoids were linked to narrow PFZs acting as stress concentrators and easy paths for crack propagation in the specimens heat-treated at 700°C/4 hours and specimens heat-treated at 804°C/1 hour followed by aging at 600°C/4 hours. Because the specimens in the AW condition contained no α-phase and the specimens heat-treated at 804°C/1 hour contained sparse, coarse α precipitates that provided little strength, the microvoids were attributed to ω-phase embrittlement, which is known to result in microvoids in the wake of ω particle shearing. HAADF-STEM imaging of the ω-phase in section 3.5.1 provided evidence of ordering, coherency and lattice strains associated with the ω-phase in the AW condition, which can cumulatively exacerbate brittle fracture in the AW specimens or any specimen containing ω-phase.

4. Conclusions

The focus of this research was to analyze the microstructural response of Ti-5553 to EB welding and PWHTs as well as to correlate the microstructural findings to fracture as a result of tensile testing. Upon completion of this research the following conclusions can be made about EBW Ti-5553 and the microstructural evolution therein and its effects on fracture.

1. The PWHTs improved the mechanical properties of the WZ compared to the AW condition in all cases except for the PHWT at 804°C/1 hour.

2. No macroscopic deformation was observed in the WZs of EBW Ti-5553 in the AW or PWHT conditions, leading to brittle-like fracture. This has been attributed to the presence of ω in the AW specimens and specimens heat treated at 804°C/1 hour, the lack of fine α platelets in specimens heat treated at 804°C/1 hour, and to PFZs in the specimens heat treated at 700°C/4 hours and at 804°C/1 hour followed by aging at 600°C/4 hours.
3. The brittle-like fracture observed across the four conditions of the EBW Ti-5553 was supported by evidence of transgranular cleavage in specimens in the AW condition and specimens heat treated at 804°C/1 hour, a combination of transgranular cleavage and intergranular fracture in specimens heat treated at 700°C/4 hours, and intergranular fracture in specimens heat treated at 804°C/1 hour followed by aging at 600°C/4 hours. However, fine microvoids were on the fracture facets in each specimen, regardless of the condition, indicating some small amount of ductility attributed to the ω-phase and PFZs.
4. ω-phase was found to exist within the retained beta in the AW condition as well as in the specimens heat treated at 804°C/1h. This suggests that the ω precipitation cannot be suppressed during cooling and that a PWHT time of 1 hour was not sufficient for complete elimination of the ω-phase by dissolution or consumption by nucleation and growth of α.
    a. The lattice parameters, a and c for ω, were found to be 4.74±0.018 Å and 2.90±0.011 Å, respectively, which are slightly larger than those reported by Silcock [Silcock, 1958] and Bagariatskii et al. [Bagariatskii et al., 1959], but still within experimental error. This suggests that because of the presence of five alloying elements, the lattice parameters are slightly larger to accommodate the different atoms.

b. HAADF-STEM imaging showed that the ω in FZ of EBW Ti-5553 in the AW condition is ordered.

c. The ω-phase in the AW specimens showed an incomplete transformation of β to ω, resulting in various stages of the displacive transformation to ω in agreement with the Phonon Mechanistic Model.

Ultimately, ω has an important role in controlling mechanical properties as well as subsequent precipitation. It is apparent that it embrittles the WZ of EBW Ti-5553, which is not desireable, but its presence is required for α-phase nucleation sites in order for fine α platelets to evolve and strengthen the β-phase. For PWHT of EBW Ti-5553, a heat treatment schedule should be chosen that mitigates ω-phase's detrimental effects on ductility, yet still enables it to provide nucleation sites for the precipitation of uniformly dispersed, fine α particles

.

5. Future Work

The work presented in this dissertation covered some of the practical aspects of EBW Ti-5553, such as mechanical properties, solidification and homogenization, precipitation during PWHTs, and evaluation of fracture mechanisms, but also some in depth investigation of the ω-phase in the AW condition including HAADF-STEM imaging. However, it only scratched the surface of investigating the effects of EBW and PWHTs on Ti-5553. It has led to the possibility of continued work to further understand the microstructural evolution and embrittlement in EBW Ti-5553. Ideas for future work are mentioned below.

1. As expected, ω was found to exist in the AW condition. HAADF-STEM imaging proved that there was a collapse of the $\{111\}_\beta$ planes in the $\langle 111\rangle_\beta$ direction, which caused an apparent displacement of atoms within the ω precipitates compared to the β matrix. Quantifying this displacement would be beneficial in determining the extent of

the transformation from β to ω as well as estimating the lattice strain associated with ω precipitates. This information would help explain the brittle characteristics imparted to the bulk material by ω.

2. ω was also found to be ordered, such that a tri-layered scheme developed. Determining which elements occupy the lattice sites in ω is important to understanding the ω-phase in the Ti-5553 system.
3. ω was only investigated in depth in FZ of the AW specimens, therefore expanding the investigation to the HAZ as well as to the FZs and HAZs of the PWHT specimens will help further explain ω's role in Ti-5553.
4. True solution treatments were not evaluated in this work. Solution treatments above the β-transus (856°C) should be carried out. It would be ideal to determine the optimum time and temperature to fully homogenize the FZ, but limit excessive grain growth. This information could better serve industrial applications of autogeneously welded Ti-5553.
5. Based on the gradient of microstructures found from the BM, through the HAZ, into the FZ, thermally simulated HAZ microstructures for the AW and PWHT conditions are needed. From this, more accurate measurements of the mechanical properties of the HAZ can be made, such as strength, impact toughness, fatigue limits, and fracture toughness.

6. References

Aaronson, H.I., Spanos, G., Masamura, R.A., Vardiman, R.G., Moon, D.W., Menon, E.S.K., Hall, M.G., *Sympathetic Nucleation: an Overview,* Mater. Sci. Eng. B, Vol. 32, p. 107-123 (1995).

Alvarez, A.-M., Robertson, I.M., Birnbaum, H.K.., *Hydrogen embrittlement of metastable β-titanium alloy,* Acta Materialia, p. 4161-4175 (2004).

American Society for Metals, "Properties & Selection – Nonferrous Alloys and Pure Metals", 9th Ed., Vol. 3, American Society for Metals, Metals Park, Ohio (1979).

Azimzadeh, S., Rack, H.J., *Phase Transformations in Ti-6.8Mo-4.5Fe-1.5Al,* Met. Mater. Trans A, Vol. 29A, p. 2455-2466 (1998).

Bagariatskii, Y.A., Nosova, , G.I., Tagunova, T.V., Doklady. Akad. Nauk. SSSR, Vol. 105, p. 1225 (1955).

Bagariatskii, Y.A., Nosova, G.I., Tagunova, T.V., *Factors in the Formation of Metastable Phases in Titanium-Base Alloys*, Dokl. Akad. Nauk. SSSR, Vo. 3, p. 1014-1018 (1959).

Bechetti, D.H., "Microstructural Evolution and Creep Rupture Behavior of INCONEL® Alloy 740H® Fusion Welds," Thesis, Lehigh University, (2013).

Bendersky, L.A., Boettinger, W.J., Burton, B.P., Biancaniello, F.S., Shoemaker, C.B., *The Formation of Ordered Omega-related Phases in Alloys of Composition Ti_4Al_3Nb,* Acta Mater. Vol. 38, No. 6, p. 931-943 (1990).

Banerjee, D., Gogia, A.K., Nandy, T.K., Joshi, V.A., *A New Ordered Orthorhombic phase in a Ti_3Al-Nb Alloy,* Acta Mater., Vol. 36, No. 4, p. 871-882 (1988).

Bania, P.J., *Beta titanium alloys and their role in the titanium industry,* J. Mater., Vol. 46, No. 7, p. 16-19 (1994).

Bermingham, M.J., McDonald, S.D., St. John, D.H., Dargusch, M.S., *Segregation and grain refinement in cast titanium alloys,* J. Mater. Res., Vol. 24, No. 4, p. 1529-1535 (2009).

Blackburn, M.J., *The Ordering Transformation in Titanium:Aluminum Alloys Containing up to 25 at. pct Aluminum,* Trans Metall. Soc. AIME, Vol. 239, p. 1200-1208 (1968).

Block-Bolton, A., Eagar, T.W., *Metal vaporization from weld pools,* Metal. Trans. B, Vol. 15, p. 461–469 (1984).

Bowen A.W., *Omega Phase Embrittlement in Aged Ti-15%Mo,* Scripta Mater., Vol.5, No. 8, P.709-716 (1971).

Bowen, A.W., *On the Strengthening of a Metastable β-Titanium alloy by ω- and α- precipitation,* Titanium '80: Science and Technology, p.1317-1326 (1980).

Bylica, A., Sieniawski, J., "Tytan i jego stopy, Panstwowe Wydawnictwo Naukowe", Warszawa, pp. 147 (1985).

Cieslak, M.J., Fuerschbach, P.W., *On the weldability, composition, and hardness of pulsed and continuous Nd:YAG laser welds in aluminum alloys 6061, 5456, and 5086,* Metal. Trans. B, Vol. 19, p. 319 (1988).

Clement, N., Lenain, A., Jacques, P.J., *Mechanical Property Optimization via Microstructural Control of New Metastable Beta Titanium Alloys,* J. Mater., p. 50-53 (2007).

Cotton, J.D., Bingert, J.F., Dunn, P.S., Patterson, R.A., *Microstructure and Mechanical Properties of Ti-40Wt Pct Ta (Ti-15 At. Pct Ta),* Met. Mater. Trans., Vol. 25, p. 461-472 (1994).

Cottrell, C.L.M., *Electron Beam Welding – a Critical Review,* Mater. & Design, Vol. 16, p. 285-291 (1985).

Danielson, P., Wilson, R., Alman, D., *Microstructure of Titanium Welds,* Adv. Mater. & Process, p. 39-42 (2003).

DebRoy, T., David, S.A., *Physical Processes in fusion welding,* Rev. Mod. Phys., Vol. 67, 1, p. 85-112 (1995).

De Fontaine, D., Paton, N.E., Williams, J.C., *The Omega Phase Transformation in Titanium Alloys as an Example of Displacement Controlled Reactions,* Acta Metall., Vol. 19, p. 1153-1162 (1971).

De Fontaine, D., *Mechanical Instabilities in the BCC lattice and the Beta to Omega Phase Transformation,* Phil. Mag., Vol. 27, 4, p. 967-983 (1973).

Devaraj, A., Nag, S., Srinivasan, R., Williams, R.E.A., Banerjee, S., Banerjee, R., Fraser, H.L., *Experimental evidence of concurrent compositional and structural instabilities leading to ω precipitation in titanium-molybdenum alloys,* Acta Mater., Vol. 60, p.596-609 (2012).

Dobromyslov, A.V., Elkin, V.A., *Martensitic transformation and metastable beta phase in binary titanium alloys with d-metals of 4-6 periods,* Scripta Mater., Vol. 44, 6, p. 905-910 (2001).

Donachie, M.J., "Titanium: A Technical Guide", 2nd Ed., ASM International, Metals Park, OH (2000).

Duerig, T.W., Terlinde, G.T., Middleton, R., Williams, J.C., *Stress Assisted Transformation in Ti-10-2-3,* Titanium '80 Science and Technology, p.1503 (1980).

Duerig, T.W., Terlinde, G.T., Williams, J.C., *Phase Transformations and Tensile Properties of Ti-10V-2Fe-3Al,* Metall. Trans. A., Vol. 11A, p.1987-1998 (1980).

Duerig, T.W., Williams, J.C., *Overview: Microstructure and Properties of Beta Titanium Alloys,* Beta Titanium alloys in the 80's: Proceedings of the Symposium, Atlanta, GA, United States, p. 16-67 (1984).

DuPont, J.N., Farren, J.D., *Influence of Heat Treatment Time and Temperature on the Microstructure and Corrosion Resistance of Cast Superaustenitic Stainless Steels,* Corros., Vol. 67, 5, p. 1-8 (2011).

Eisler, G.R., Fuerschbach, P.W., *SOAR: An Extensible Suite of Codes for Weld Analysis and Optimal Weld Schedules,* Seventh International Conference on Computer Technology in Welding, NIST, San Francisco, CA, p 257-268 (1997).

Fanning, J.C., *Properties of TIMETAL 555 (Ti-5Al-5Mo-5V-3Cr-0.6Fe),* J. Mater. Eng. Peform., Vol. 14, p. 788-791 (2005).

Fanning, J.C., *Recent Developments in High-Strength Near-Beta Titanium Alloys,* Presented at "Titanium 2011", San Diego, CA, Oct. 2-5 (2011).

Flower, H.M., Davis, R., West D.R.F., *Martensite Formation and Decomposition in Alloys of Titanium Containing β-Stabilizing Elements,* Titanium and Titanium Alloys, Scientific and Technological Aspects, 1703-1715 (1982).

Folz, J.W., Welk, B., Collins, P.C., Fraser, H.L., Williams, J.C., *Formation of Grain Boundary α in β Ti Alloys: Its Role in Deformation and Fracture Behavior of These Alloys,* Metall. Mater. Trans. A, Vol 42A, p. 645-650 (2011).

Frost, P.D., Parris, W.M., Hirsch, L.L., Doig, J.R., Schwartz, C.M., *Isothermal Transformation of Titanium Chromium Alloys,* Trans. Amer. Soc. Metals, Vol. 46, p. 231-256 (1954).

Furuhara, T., Aaronson, H.I., *Crystallography and Interfacial Structure of Proeutectoid Alpha Grain Boundary Allotriomporphs in a Hypoeutectoid Ti-Cr Alloy,* Acta Metall. Mater, Vol. 39, 11, p. 2887-2899 (1991).

Furuhara, T., Makino, T., Idei, Y., Ishigaki, H., Takada, A., Maki, T., *Morphology and Crystallography of Alpha Precipitates in Beta Ti-Mo Binary Alloys,* Mater. Trans., JIM, Vol., 39, 1, p. 31-39 (1998).

GOM mbH, *ARAMIS, User Information – Hardware,* Braunschweig, Germany, GOM mbH (2007).

GOM mbH, *ARAMIS, User Information – Software,* Braunschweig, Germany, GOM mbH (2007).

Gridnev, V.N., Ivasishin, O.M., Oshkaderov, S.P., *Phsical principle of High-Speed Thermal Hardening of Titanium Alloys,* Russian, Naukova Dumka, Kiev, (1986).

Grytten, F., Daiyan, H., Polanco-Loria, M., Dumoulin, S., *Use of digital image correlation to measure large-strain tensile properties of ductile thermoplastics,* Polymer Testing, Vol. 28, p. 653-660 (2009).

Gysler, A., Lutjering, G., Gerold, V., *Deformation behavior of age-hardened Ti- Mo alloys,* Acta Met, Vol. 22, p.901-909 (1974).

Hansen, M., Anderko, K., "Constitution of Binary Alloys", McGraw-Hill Book Co., Inc., Maple Press Co., York, PA, pp. 1059-1062 (1958).

Harper, M.L., "A Study of the Microstructural and Phase Evolutions in TIMETAL 555", Thesis, The Ohio State University, (2004).

Hickman, B.S., *Omega Phase Precipitation in Alloys of Titanium with Transition Metals*, Trans. TMS-AIME, Vol. 245, p.1329-1335 (1969a).

Hickman, B.S., *The Formation of Omega Phase in Titanium and Zirconium Alloys: A Review*, J. Mater. Sci., Vol. 4, p.554-563 (1969a).

Ho, .F., Ju, C.P., ChernLin, *Structure and properties of cast binary Ti-Mo alloys*, Biomater., Vol. 20, p. 2115-2122 (1999).

Ivasishin, O.M., Markovsky, P.E., Matviychuk, Yu.V., Semiatin, S.L., *Precipitation and Recrystallization Behavior of Beta Titanium Alloys during Continuous Heat Treatment,* Metall. Mater. Trans. A, Vol 34A, p. 147-158 (2003).

Jamieson, J.C., *Crystal Structures of Titanium, Zirconium, and Hafnium at High Pressures*, Sci., Vol. 140, p. 72-73 (1963).

Kar, S.K., Ghosh, A., Fulzele, N., Bhattacharjee, A., *Quantitative microstructural characterization of a near beta Ti alloy, Ti-5553 under different processing conditions,* Mater. Charact., Vol. 31, p. 37-48 (2013).

Kearns, M., *Titanium: Alive, Well, and Booming!*, Adv. Mater. Proc., p.63-64 (2005).

Kestner-Weykamp, H.T., Ward, C.H., Broderick, T.F., Kaufman, M.J., *Microstructures and Phase Relationships in the Ti_3Al+Nb System*, Scripta Metall., Vol. 23, pp. 1697-1702 (1989).

Liu, C.M., Wang, H.M., Tian, X.J., Tang, H.B., *Subtransus triplex heat treatment of laser melting deposited Ti-5Al-5Mo-5V-1Cr-1Fe near β titanium alloy,* Mater. Sci. Eng. A, Vol. 590, p. 30-36 (2014).

Luke, C.A., Taggart, R., Polonis, D.H., *The Metastable Constitution of Quenched Titanium and Zirconium-Base Binary Alloys*, Trans. ASM, 57, p.142- 149 (1964).

Lütjering, G., Williams, J.C., "Titanium, Engineering Materials and Processes", 2nd Ed., Springer-Verlag (2007).

Lütjering, G., Albrecht, J., Sauer, C., Krull, T., *The influence of soft, precipitate-free zones at grain boundaries in Ti and Al alloys on their fatigue and fracture behavior*, Vol. 468-470, p. 201-209 (2007).

Lynch S.P., Hole B., Pasang T., *Failure of Welded Titanium Aircraft Ducts,* Engineering Failure Analysis, Vol. 2, 4, p. 257-273 (1995).

McGann, M., Matthews, S., *Determination of Design Data for Heat Treated Titanium Alloy Sheet*, Vol. 2a, ASD-TDR-62-355, reported in Aerospace Structural Metals Handbook,

Mechanical Properties Data Center, Bettelle Columbus Laboratories, Columbus, Ohio, Code 3707, p. 9 (1962).

Mendez, P., Eager, T.W., *Welding Processes for Aeronautics,* Adv. Mater. Proc., p. 39-43 (2001).

Menon, E.S.K., Aaronson, H.I., *Black Plate Formation in Ti-X Alloys,* Acta Metall., Vol. 34, 10, p. 1963-1973 (1986).

Mitchel, R., Short, R., Pasang, T., Littlefair, G., *Characteristics of EBW Ti alloys,* Advances in Mater. Res., Vol. 275, p. 81-84 (2011).

Moiseev, V.N., Zakharov, Yu.I., Kirillov, Yu.G., Dolzhanskii, Yu.M., Danilina, T.G., *Heat Treatment of Titanium Alloy VT22,* Metallovedenie i Termischeskaya Obrabotka Metallov, Vol. 3 p. 46-49 (1990).

Mots, M., Hooper, R., Frost, P., *Report on the Engineering Properties of Commercial Titanium Alloys*, TML Report 92, Titanium Metallurgical Laboratory, Battelle Institute, Columbus Ohio, June (1958).

Mueller, S., Bratt, C., Mueller, P., Cuddy, J., Shankar, K., *Laser Beam Welding of Titanium—A Comparison of CO2 and Fiber Laser for Potential Aerospace Applications,* Proceedings of ICALEO 2008: 27th International Congress on Applications of Lasers and Electro-Optics (2008).

Mullins, W.W., Sekerka, R.F., *Morphological Stability of a Particle Growing by Diffusion or Heat Flow,* J. Appl. Phys., Vol. 32, 2, p. 323-329 (1963).

Mullins, W.W., Sekerka, R.F., *Stability of a Planar Interface during Solidification of a Dilute Binary Alloy,* J. Appl. Phys., Vol. 35, 2, p. 444-451 (1964).

Munitz, A., Colter, C., Shaham, H., Kohn, G., *Electron Beam Welding of Magnesium AZ91D Plates,* Weld. Res. Supplement, p. 202s-208s (2000).

Muraleedharan, K., Nandy, T.K., Banerjee, D., *Phase stability and ordering behaviour of the O phase in Ti-Al-Nb alloys,* Vol. 3, No. 3, p. 187-199 (1995).

Nag, S., "Influence of Beta Instabilities on the Early Stage of Nucleation and Growth of Alpha in Beta Titanium Alloys", Dissertation, The Ohio State University (2008).

Nag, S., Banerjee, R., Hwang, J.Y., Harper, M., Fraser, H.L., *Elemental partitioning between α and β in the Ti-5Al-5Mo-5V-3Cr-0.5Fe (Ti-5553) alloy,* Phil. Mag., Vol. 89, 6, p. 535-552 (2009a).

Nag, S., Banerjee, R., Srinivasan, R., Hwang, J.Y., Harper, M., Fraser, H.L., *ω-Assisted nucleation and growth of α precipitates in the Ti-5Al-5Mo-5V-3Cr-0.5Fe β titanium alloy,* Acta Mater., Vol. 57, p. 2136-2147 (2009b).

Nag., S., Zheng, Williams, R.E.A., Devaraj, A., Boyne, A., Wang. Y., Collins, P.C., Viswanathan, G.B., Tiley, J.S., Muddle, B.C., Banerjee, R., Fraser, H.L., *Non-classical homogeneous precipitation mediated by compositional fluctuations in titanium alloys,* Acta Mater., Vol. 60, p. 6247-6256 (2012).

Ogi, H., Kai, S., Ledbetter, H., Tarumi, R., Hirao, M., Takashima, K., *Titanium's high temperature elastic constants through the hcp-bcc phase transformation,* Acta Met., Vol. 52, p. 2075-2080 (2004).

Ohmori, Y., Natsui, H., Nakai, K., *Crystallographic Analysis of α Phase Formation in a Metastable β Ti Alloy,* Mater. Trans., JIM, Vol. 39, 1, p. 49-56 (1998).

Okuda, H., Ochiai, S., *The Effects of Solute and Vacancy Depletion on the Formation of Precipitation-Free Zones in a Model Binary Alloy Examined by a Monte Carlo Simulaion,* Mater. Trans., JIM, Vol. 45, 5, p. 1455-1460 (2004).

Orlova, L.M., Lemesh, A.D., Belozub, G.P., Filatova, T.V., *Metallographic study of beta-solid solution decomposition for Titanium alloy VT22,* Metallovedenie i Termicheskaya Obrabotka Metallov, Vol. 1, p. 56-58 (1986).

Polmear, I.J., "Light Alloys", *Metallurgy of the Light Metals,* 3rd Ed., Arnold, London, England, 1995.

Porter, D.A., Easterling, K.E., "Phase Transformations in Metals and Solids", 2nd Ed., CRC Press, Taylor & Francis Group, Boca Raton, FL (2004).

Prima, F., Vermaut, P., Texier, G., Ansel, D., Gloriant, T., *Evidence of α-nanophase heterogeneous nucleation from ω particles in a β-metastable Ti-based alloy by high-resolution electron microscopy,* Scripta Mat., Vol. 54, p. 645-648 (2006).

Qazi, J.I., Marquardt, B., Allard, L.F., Rack, H.J., *Phase transformations in Ti-35Nb-7Zr-5Ta-(0.06-0.68)O alloys,* Mater. Sci. Eng. C., Vol. 25, p. 389-397 (2005).

Rhodes, C.G., Williams, J.C., *The Precipitation of α-Phase in Metastable β-Phase Ti Alloys,* Metall. Trans. A, Vol. 6A, p. 2103-2114 (1975).

Rosenberg, H.W., *The Science, Technology and Application of Titanium,* Pergamon Press, Oxford, UK., p. 851 (1970).

Rosenthal, D., *Mathematical theory of heat distribution during welding and cutting,* Welding J., 20, 5, p. 220-234 (1941).

Russell, J.D., *Developments in heavy section EB welding, Metal Construction*, Vol. 13, 10, p. 601 (1981).

Sabol, J.C., Pasang, T., Misiolek, W.Z., Williams, J.C., *Localized tensile strain distribution and metallurgy of electron beam welded Ti-5Al-5V-5Mo-3Cr titanium alloys,* J. Mater. Proc. Tech., Vol. 212, p. 2380-2385 (2012).

Sanchez-Amaya, J.M., Delgado, T., De Damborenea, J.J., Lopez, V., Botana, F.J., *Laser welding of AA 5083 samples by high power diode laser,* Science and Technology of Welding and Joining, Vol. 14, 1, p. 78–86 (2009).

Sass, S.L., *The Structure and Decomposition of Zr and Ti b.c.c. Solid Solutions,* J. Less-Common Met., Vol. 28, p. 157-173 (1972).

Sauer, C., Lütjering, G., *Influence of α layers at β grain boundaries on mechanical properties of Ti-alloys,* Mater. Sci. Eng. A, Vol. A319-321, p. 393-397 (2001).

Schectman, D., Blackburn, M.J., Lipsitt, H.A., *The Plastic Deformation of TiAl,* Metall. Trans. B, Vol. 5, No. 6, p. 1373-1381 (1974).

Sciaky Inc., *Electron Beam Welding Systems,* WWW Source, http://www.sciaky.com/sample_EB_systems.html, 2014.

Shariff, T., Cao, X., Chromik, R.R., Wanjara, P., Cuddy, J., Birur, A., *Effect of joint gap on the quality of laser beam welded near-β alloy with the addition of Ti-6Al-4V filler wire,* J. Mater. Sci.. Vol. 47, p. 866-875 (2012).

Shevel'kov, V.,V., *Structural conversions in VT22 Titanium Alloy during aging*, Metallovedenie i Termicheskaya Obrabotka Metallov, Vol. 8, p. 33-37 (1992).

Siebert, T., Becker, T., Spiltthof, K., Neumann, I., Krupka, R., *High-speed digital image correlation: error estimation and applications,* Optical Eng., Vol. 46, 5, p. 1-7 (2007).

Silcock, J.M., Davies, M.H., Hardy, H.K., *The Mechanism of Phase Transformations in Solids*, Inst. of Metals, Vol. 93 (1956).

Silcock, J.M.,*An X-Ray Examination of the ω Phase in TiV, TiMo, and TiCr Alloys,* Acta Metall Mater., Vol. 6, p. 481-492 (1958).

Strychor, R., Williams, J.C., *Solid to Solid Phase Transformations,* AIME, Warrendale, USA, p. 249 (1982).

Strychor, R., Williams, J.C., Soffa, W.A., *Phase Transformations and Modulated Microstructures in Ti-Al-Nb Alloys,* Metall. Trans. A, Vol. 19A, p. 225-234 (1988).

Sukedai, E., Hashimoto, H., Tomita, M., *Investigation of omega-phase in Ti-Mo alloys by high resolution electron microscopy, image processing and dark-field methods,* Phil. Mag. A, Vol. 64, 6, pp. 1201-1208 (1991).

Tal-Gutelmacher E., Eliezer D., *The Hydrogen Embrittlement of Titanium-Based Alloys,* J. Mater., Vol. 57, 9 (2005).

Thompson, A.W., Williams, J.C., *Nuclei for Ductile Fracture in Titanium*, IFC4, Waterloo, Canada, June 19-24. p. 343-348 (1977).

Tiwari, V., Sutton, M.A., McNeill, S.R., *Assessment of High Speed Imaging Systems for 2D and 3D Deformation Measurements: Methodology Development and Validation,* Exp. Mech., Vol. 47, p. 561-579 (2007).

Unwin, P.N.T., Lorimer, G.W., Nicholson, R.B., *The Origin of the Grain Boundary Precipitate Free Zone,* Acta Metall., Vol. 17, p. 1363-1377 (1969).

Vassel, A., *Microstructural Instabilities in Beta Titanium Alloys*, Beta Titanium in the 1990's, p.173-185 (1990).

Vishwakarma, K.R., Richards, N.L., Chaturvedi, M.C., *Microstructural analysis of fusion and heat affected zones in electron beam welded ALLVAC® 718PLUS™ superalloy,* Mater. Sci. Eng. A, Vol. 480, p. 517-528 (2008).

Welk, B., "Microstructural and Property Relationships in Beta-Titanium Alloy Ti-5553", Thesis, The Ohio State University, (2010).

Williams, J.C., Blackburn, M.J., *The Influence of Misfit on the Morphology and Stability of the Omega Phase in Titanium-Transition Metal Alloys*, Trans. Met. Soc., AIME, Vol. 245, p.2352-2355 (1969)

Williams, J.C., Hickman, B.S., Marcus, H.L., *The Effect of Omega Phase on the Mechanical Properties of Titanium Alloys*, Met. Trans., Vol. 2, p.1913-1919 (1971).

Wood, R.M., *Martensitic alpha and omega phases as deformation products in a Titanium-15% Molybdenum Alloy,* Acta Metall., Vol. 11, p. 907-914 (1963).

Wu, K.C., *Correlation of Properties and Microstructure in Welded Ti-6Al-6V-2Sn,* Weld. Res. Supplement, p. 219s-226s (1981).

Zhang, B., Wang, J., Wan, X., Chen, W., *A Study on the Beta and Omega Phases in a Ti-Al-Cr Alloy,* Scripta Metall., Vol. 30, p. 399-404 (1994).

Ziegler, W., Mullins, J., Hwa, S., "Specific Heat and Thermal Conductivity of Four Commercial Titanium Alloys", Advances in Cryogenic Engineering, Vol. 8, Plenum Press, New York, p. 268 (1963).

7. Vita

Joseph was born on July, 28 1986 in Chambersburg, PA. He grew up in Mercersburg, PA with his parents, Joe and Susan Sabol, and his two younger sisters, Molly and Claire. Joseph attended high school at Mercersburg Academy, a college preparatory school, for four years. He then enrolled in Lehigh University's P.C. Rossin College of Engineering for the 2005 fall semester. Joseph graduated in May of 2009 with a Bachelor of Science in materials science and engineering as well as with a minor in German. Joseph then began his graduate studies in June of 2009 under the guidance of Dr. Wojciech Misiolek. After three years of working on characterizing the interaction of solid nickel with liquid zinc for use in solar thermal energy storage systems and after a month spent in New Zealand collaborating with Timotius Pasang at the Auckland University of Technology on welding titanium, he obtained his Masters in materials science and engineering in May 2012. Joseph continued his graduate work under Dr. Misiolek as a Ph.D. candidate researching the effects of electron beam welding on titanium. He graduated in 2014 with a doctorate in materials science and engineering. He is now at Exponent, Inc. in Atlanta, GA performing failure analysis as a metallurgical consultant.